Population Balance Modeling Webinar – 1st Edition

November 30th, 2023

Book of Abstracts

Chairs:

Fiora ARTUSIO (Politecnico di Torino)

Graziano FRUNGIERI (Politecnico di Torino)

In memory of **Graziano Frungieri**

Organizing committee:

Fiora ARTUSIO   (Politecnico di Torino)

Grégory BANA   (CEA)

Yash BARHATE   (Purdue University)

Graziano FRUNGIERI   (Politecnico di Torino)

Scientific committee:

Nida Sheibat-Othman	(Université Claude Bernard Lyon 1)
Heiko Briesen	(Technical University of Munich)
Zoltan K. Nagy	(Purdue University)
Jerome Morchain	(INSA, Toulouse)
Joseph Yong Kuen Ho	(Monash University Malaysia)
Antonio Buffo	(Politecnico di Torino)
Marco Vanni	(Politecnico di Torino)
Daniele Marchisio	(Politecnico di Torino)
Doraiswami Ramkrishna	(Purdue University)
Elena Simone	(Politecnico di Torino)
Noureddine Lebaz	(University of Lyon)
Matthäus U. Bäbler	(KTH Royal Institute of Technology)
Antonello Barresi	(Politecnico di Torino)
Rodney O. Fox	(Iowa State University)
Giuseppina Montante	(Università di Bologna)
Ashwin Kumar Rajagopalan	(University of Manchester)
Szilágyi Botond	(Budapest University of Technology and Economics)
Andreas Bück	(Friedrich-Alexander University Erlangen)
Ville Alopaeus	(Aalto University)
Christine Frances	(INP - ENSIACET Toulouse)
Paulo Laranjeira da Cunha Lage	(Universidade Federal do Rio de Janeiro)
Zheng-Hong Luo	(Shanghai Jiao Tong University)
Menwer Attarakih	(University of Jordan)
Gurmeet Kaur	(Technical University of Munich)
Dimitrios Meimaroglou	(University of Lorraine)
Nicodemo Di Pasquale	(Brunel University London)

Welcome!

Dear Colleagues,

This book of abstracts contains the final camera ready of abstracts of all the papers presented at the first edition of Population Balance Modeling Webinar (PBMW) held on November 30th, 2023.

The objective of this webinar is to provide a platform for early career researchers (PhD students, recently graduated PhDs, and Postdocs) to discuss their latest progress and results in the field of population balance modeling. Our ambition is to collect contributions addressing the formulation, numerical strategies, experimental validation and/or coupling of population balance models with smaller or large-scale techniques in the fields of environmental, biological, pharmaceutical, and chemical processing.

We extend our sincere thanks to the members of the international scientific committee for their reviews, advice during the selection process, and the support during the preparation of technical program. Additionally, we express gratitude to all authors for submitting their abstracts.

We hope that this book of abstracts serves as a valuable reference for the contributions made at PBMW 2023.

Sincerely,

The Webinar Chairs

The Organizing Committee

Summary

Assessing bubble dispersion and mass transfer in Ambr®250 using updated population balance models for bioprocess development

Vishal Kumar Singh[1], Ioscani Jimenez Del Val[2], Jarka Glassey[1,3] Fatemeh Kavousi[1]
[1] Process and Chemical Engineering, University College Cork, Food Science Building, 1 College Rd, Cork T12 TP07, Ireland
[2] School of Chemical & Bioprocess Engineering, University College Dublin, Ireland
[3] School of Engineering, Newcastle University, Newcastle upon Tyne, UK
Corresponding author email: 120222313@umail.ucc.ie

ABSTRACT

Ambr®250 vessels are commonly used miniaturised reactor systems for bioprocess development. They have increased the throughput of process development activity and are deemed cost-efficient due to their small operating volume. Ambr®250 bioreactors are suitable for scale-down experiments but require comparable hydrodynamic behaviour to reference large scale to ensure process consistency. Computational fluid dynamics (CFD) aided simulation of flow characteristics is a time-efficient means of screening suitable operating conditions. In this study, the bubble distribution and volumetric mass transfer have been simulated for Ambr®250 using an updated coupled CFD-PBM model to suit cell culture fluid characteristics.

Keywords: Ambr®250, scale-down, computational fluid dynamics (CFD), bubble distribution, volumetric mass transfer

1. INTRODUCTION

Bioprocess development, particularly in the fields of biotechnology and pharmaceuticals, has witnessed significant advancements with the introduction of miniaturised reactor systems like the Ambr®250 vessels. These vessels have become invaluable tools for researchers and engineers, enhancing throughput and cost-effectiveness by enabling operations at lower volumes. However, to fully harness the benefits of these miniaturised bioreactors, it is essential to ensure that their hydrodynamic behaviour closely mimics that of larger reference-scale systems.

Achieving comparable hydrodynamic behaviour to reference-scale reactors is critical for maintaining process fidelity across different scales. Computational Fluid Dynamics (CFD) provides a powerful means to predict and analyse fluid flow characteristics in the Ambr®250, enabling the rapid screening of suitable operating conditions. In this study, we employ CFD simulations, coupled with updated Population Balance Models (PBMs), to investigate the distribution of air bubbles and volumetric mass transfer in the Ambr®250 using Ansys CFX.

2. MATERIALS AND METHODS

2.1. Geometry and meshing

The Ambr®250 geometry was created in Ansys SpaceClaim. The dimension of Ambr®250 was retrieved from literature (Li et al., 2018) with the diameter of the tank, T= 62.5 mm and the height of the tank, H was maintained equivalent to 175 ml volume occupancy (*Figure 1*). The default tetrahedron mesh was used in the Ansys meshing tool with the advanced size function for proximity & curvature capture. To resolve the boundary layer profiles, an inflation of 1.2 growth rate and a maximum layer of 5 was assigned. A mesh refinement study determined the optimal mesh size, starting with 1.2 million cells up to 2.03 million cells. It is noted that the change of liquid velocity was insignificant for refinements beyond the 1.2 million mesh, so this mesh was used for further simulations.

2.2. Numerical setup

The system was modelled using the Eulerian- Eulerian multiphase model, and the impeller rotation has been modelled using Multiple Reference Frame (MRF) method. Since the density difference between the two phases (air and fluid) is high, the dispersed k-ε turbulence model was used. The bubble size distribution has been modelled using the population balance equations module in Ansys CFX.
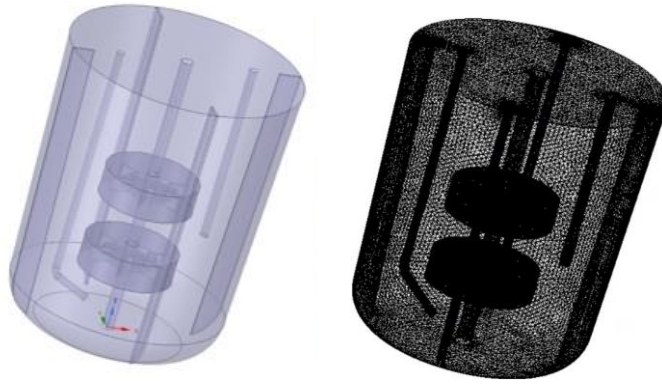
Figure 1. Isometric view of the CAD and meshed geometry of Ambr®250

In this work, the MUSIG(Multiple Size Group) discrete method was employed, in which a large variation of bubble sizes (bins) was specified to describe air as a polydispersed phase. Ten discrete bin sizes ranging from 0.1 mm to 18 mm were applied, with 3.73 mm as the sole initial size (experimentally obtained by Li et al. (2018). Li et al. observed differences in the volumetric mass transfer rate in Ambr250 compared to experimental data, which can be attributed to using air-water mixture properties for simulation. The model parameters for Luo and Svendsen breakup (Luo & Svendsen, 1996) and Prince and Blanch coalescence (Prince & Blanch, 1990) models were updated to mimic cell culture fluid properties. For validation of CFD simulations, volumetric gas-liquid mass transfer rate (k_La) was calculated as the product of the mass transfer coefficient, k_L (m s^{-1}) and the specific surface area, a (m^{-1}) for varied agitation rates- 300 rpm, 600 rpm and 650 rpm. Based on Higbie's penetration theory (Lamont & Scott, 1970), the mass transfer coefficient is given by:

$$k_L = \frac{2\sqrt{D'}}{\sqrt{\pi}} \sqrt[4]{\frac{\varepsilon\rho}{\mu}}$$

1

where D' (m^2 s^{-1}) is the molecular diffusion coefficient, ε (m^2 s^{-3}) is the turbulent dissipation rate, ρ (kg m^{-3}) is the density of the liquid and μ (Pa s) is the dynamic viscosity of the liquid. The interfacial area is calculated from the mean Sauter mean diameter d_{32} (m) as:

$$a = \frac{6\,\alpha'}{d_{32}}$$

2

where α' is the gaseous volume fraction.

3. RESULTS AND DISCUSSION

The velocity magnitude and turbulent eddy dissipation rate (**Figure 2**) are high around the impeller and shaft region. Fluid velocity near the impeller tip is 0.5 m/s, which is in agreement with experimental tip speed

(a) Velocity profile   (b) Turbulence dissipation rate   (c) Bubble size distribution

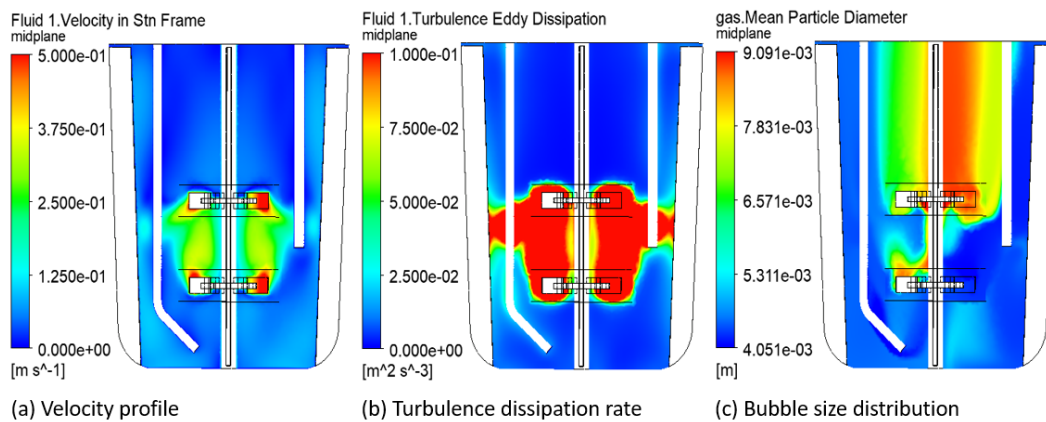*Figure 2. Simulated hydrodynamic profiles of Ambr®250 for 600 rpm agitation rate and 0.02 vvm aeration rate (a)Velocity profile (b) Turbulence dissipation rate (c) Bubble size distribution*

range of 0.27 – 1.02 m/s reported by Bareither et al. for Ambr®250 under agitation speed range of 200 – 800 rpm (Bareither et al., 2013). The mean particle diameter at 600 rpm shows that both the impellers are in

dispersed regime, while larger bubbles appear to accumulate near the top of the shaft (***Figure 2(c)***). k_La at varied agitation rates- 300 rpm, 600 rpm and 650 rpm (***Figure 3***) matches closely to experimental data.
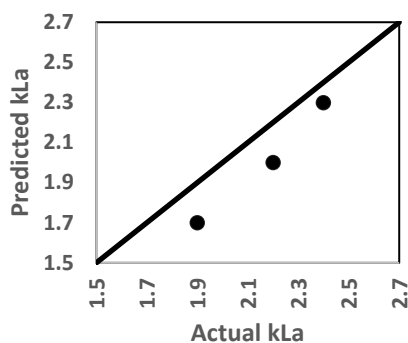

Figure 3 *Parity plot for k_La for Ambr®250 at 300, 600 and 650 rpm agitation rates and 0.02 vvm aeration rates*

The parity plot has a root mean square error of 0.17, which has more accuracy than root mean square error of 0.3 reported by Li et al. in literature. This reduction in error can be attributed to the refinement in bin size, initial bubble size, bubble breakage and coalescence coefficients.

4. CONCLUSIONS

In this study, we used CFD to model bubble distribution and volumetric mass transfer rate (k_La) inside Ambr®250 bioreactors using updated Population Balance Models (PBMs). Our simulations aligned well with experimental data and enhanced our understanding of Ambr®250's performance at varied agitation rates. It is important to note that results are sensitive to model parameters (bin size, initial bubble size, bubble breakage and coalescence coefficients), and hence, the parameters must be based on experimental observations. Nevertheless, CFD simulations assist to help design and optimise bioreactor performance, requiring less time and fewer experiments, leading to faster delivery of biologics to the market.

REFERENCES
Bareither, R., Bargh, N., Oakeshott, R., Watts, K., & Pollard, D. (2013). Automated disposable small scale reactor for high throughput bioprocess development: a proof of concept study. *Biotechnology and Bioengineering*, *110*(12), 3126–3138. 10.1002/BIT.24978

Lamont, J. C., & Scott, D. S. (1970). An eddy cell model of mass transfer into the surface of a turbulent liquid. *AIChE Journal*, *16*(4), 513–519. 10.1002/AIC.690160403

Li, X., Scott, K., Kelly, W. J., & Huang, Z. (2018). Development of a Computational Fluid Dynamics Model for Scaling-up Ambr Bioreactors. *Biotechnology and Bioprocess Engineering*, *23*(6), 710–725. 10.1007/s12257-018-0063-5

Luo, H., & Svendsen, H. F. (1996). Theoretical Model for Drop and Bubble Breakup in Turbulent Dispersions. *AIChE Journal*, *42*(5), 1225–1233. 10.1002/aic.690420505

Prince, M. J., & Blanch, H. W. (1990). Bubble coalescence and break-up in air-sparged bubble columns. *AIChE Journal*, *36*(10), 1485–1499. 10.1002/aic.690361004

Centrifugal creaming study of oil in water emulsions: Experimental and modeling approach

Kristy Touma [1], Noureddine Lebaz [1] and Nida Sheibat-Othman[1]

[1]University of Lyon, Claude Bernard Lyon 1, CNRS, LAGEPP UMR 5007, F-69100, Villeurbanne, France

Corresponding author email: kristy.touma@univ-lyon1.fr

ABSTRACT

In this study, we present an overview of the creaming phenomenon and its importance in concentrated emulsion systems. We discuss the underlying principles and mechanisms involved in creaming, including the influence of the preparation parameters and limitations related to light transmission in the used device. A mathematical model is then identified to describe the creaming behavior under centrifugation forces based on the convection-diffusion equation.

Keywords: creaming, convection-diffusion model, centrifugal forces, concentrated O/W emulsions.

1. INTRODUCTION

Creaming is a common phenomenon observed in oil-in-water (O/W) emulsions, wherein the dispersed oil droplets tend to migrate toward the top of the emulsion due to the density differences. Understanding and predicting the creaming behavior of emulsions is crucial in various industrial applications, including food, pharmaceuticals, and cosmetics. However, this presents several challenges due to the difficulty in quantifying droplet-droplet and droplet-continuous phase interactions, and the lack of noninvasive and quantitative measurement techniques. Indeed, several measurement techniques were employed to evaluate the creaming due to gravity forces, such as NMR methods, turbidimetry, Raman spectroscopy, optical image analyzer or conductivity measurement. However, these studies are usually limited to some formulations of emulsions that would cream slowly under normal conditions (e.g. diluted emulsions, big droplets, low continuous phase viscosity). In emulsions that are more stable against creaming, such as concentrated emulsions, there is a need to accelerate the creaming phenomenon to be able to predict the creaming behavior during storage for longer periods. For this objective, a centrifugally induced transmission measurement technique would represent a powerful tool as it can induce fast creaming or sedimentation (Antonopoulou *et al.*, 2018).

To model creaming, many approaches have been used, involving computational fluid dynamics (CFD) or population balance models (PBM) when phenomena other than creaming occur (e.g. coalescence). Also, the convection-diffusion equation can be used to describe satisfactorily the binary creaming phenomenon (Deb *et al.*, 2022) which is less computationally intensive. This model was however not evaluated for concentrated emulsions, due to the slow creaming behavior and lack of measurements of dense emulsions.

Hence, this study focuses on the modeling and experimental investigation of creaming in highly concentrated O/W emulsions under centrifugal forces. The convection-diffusion equation is employed to monitor the concentration profiles along the height of the sample and over time.

2. MATERIALS AND METHODS

2.1. Emulsions preparation and characterization

O/W emulsions were prepared using an Ultra-Turrax homogenizer. The viscosities of both phases, water for continuous and silicone oil as the dispersed phase, were varied as seen in Table 1. The used hydrophilic emulsifier is Polysorbate20 (Tween™ 20, Sigma-Aldrich) and is present at 0.5 w.t% in the continuous phase to ensure full monolayer coverage of the surface of the droplets and saturation of the continuous phase. Glycerol was used to modify the viscosity of the continuous phase (at 45.7 w.t % for the viscosity of 5 mPa.s, 57.81 w.t % for 10 mPa.s and 66.3 w.t % for 20 mPa.s).

Table 1. *Chemical ingredients properties.*

Material	Viscosity μ (mPa.s)	Density ρ (Kg/m³)	Refractive index n_d
Water Ultra-Pure	0.9914	999	1.3316
Silicone oil	5, 10, 20, 50, 100	913, 930, 949, 960, 970	1.3953, 1.3986, 1.4006, 1.4018, 1.4024
Continuous phase	5	1000.19	1.392
Continuous phase	10	1000.51	1.4087
Continuous phase	20	1000.73	1.4419

Granulometry measurements were carried out using a Mastersizer®, for samples taken before and after the creaming, and they validated that no coalescence of droplets occurred during the creaming time.

The instrument used to monitor the creaming profiles along time and position is the LUMisizer®. In this device, a laser emits a beam of light through the tube containing the emulsion. The transmitted light is then measured over time and the sample height. It utilizes centrifugal forces to enhance the separation of emulsion droplets, allowing us to study highly dispersed emulsions in short periods of time.

2.2. Modeling Approach
The convection-diffusion equation is given by:

$$\frac{\partial \emptyset_i}{\partial t} + \frac{\partial (u_i \emptyset_i)}{\partial z} = \frac{\partial}{\partial z}\left(D \frac{\partial \emptyset_i}{\partial z}\right) \tag{1}$$

This equation describes the transport of oil droplets within the emulsion sample and allows us to calculate the oil fraction ($\emptyset_i$) over time (t) and space (z), for droplets of different diameters (d_i). In addition, the model adds a correction factor (n) to the velocity calculation to account for the dispersed phase hindering effect on the movement of the droplets, as follows:

$$u_i(z,t) = u_{ti}\left(1 - \frac{\emptyset_T}{\emptyset_{max}}\right)^n \tag{2}$$

Different terminal velocity models are to be compared (i.e.: Kumar and Hartland, Stokes law), considering the centrifugal forces applied, besides the drag and buoyancy forces. The PDEPE function of MATLAB® is used to solve this model. Then, through experimental fitting, the two parameters D and n are identified for the different operating conditions varied. This identification is done in two cases: considering monodispersed emulsion (since the polydispersity index, PDI, is relatively small) and then taking the droplet size distribution.

3. RESULTS AND DISCUSSION
An example of the light transmission measured over the sample height with time is shown in Figure 1. The main limitation of this device is that when the oil fraction varies between 0 and 3 %, the light transmission decreases drastically to about 15 % (Figure 1 on the right). Therefore, the device does not allow accurate evaluation of fractions higher than 3%. Moreover, in the diluted region, due to the high variation of the transmission when the concentration increases, there is a big uncertainty on the prediction of very low oil fractions (<0.5 %). However, based on the information provided for the confidence interval (0.5 %-3 %), model fitting can be done. Another difficulty was observed when adding glycerol in the continuous phase, which was found to affect the optical aspect of the emulsion, altering the transmittance profiles and prohibiting the prediction of the dispersed phase concentration. This is due to the nonlinear variation in the transmission as a function of the ratio of the reflective indices of the dispersed and continuous phases ($n_{dispersed}/n_{continuous}$, Table 1).
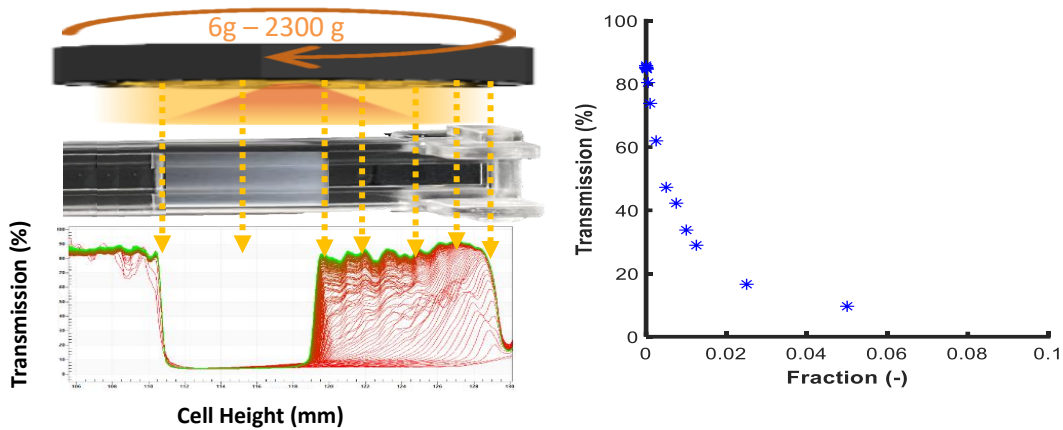
Figure 1. *The transmittance measurement in the Lumisizer (left) and the relation between transmission and oil fraction for a particular emulsion at one instance (right).*

An example of model simulation results compared to the experimental results of the Lumisizer is shown in Figure 2. The figure shows the height variation as a function of time corresponding to an oil fraction of 2.5 %. Improvements and interpretations are still in progress for the parameter estimation and model fitting.
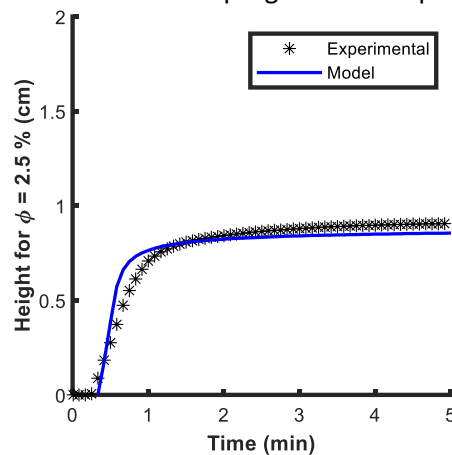
Figure 2. *Height (when the emulsion reaches ϕ=2.5 %) as a function of time, for an emulsion with mean diameter d_{43}=6.92 μm, μ_d=20 mPa.s and μ_c=1 mPa.s, ϕ_0=40 % for identified D=2.5×10^{-8} m/s^2 and n=2.5 under centrifugation of 1000×g m.s^{-2}.*

4. CONCLUSION

This study discusses the experimental evaluation of the creaming phenomenon and the governing equation and assumptions of the convection-diffusion model. The instrument used has limitations specifically in the detection range besides the influence of some additives on the optical properties of the medium and hence light transmission. However, it permits a proper investigation of the influence of the preparation parameters on the creaming process and hence the stability of concentrated emulsions.

REFERENCES

Antonopoulou, E. *et al.* (2018) 'Numerical and experimental analysis of the sedimentation of spherical colloidal suspensions under centrifugal force', *Physics of Fluids*, 30(3), p. 030702. 10.1063/1.5010735.

Deb, T.K. *et al.* (2022) 'Monitoring and Modeling of Creaming in Oil-in-Water Emulsions', *Industrial & Engineering Chemistry Research*, 61(13), pp. 4638–4647. 10.1021/acs.iecr.1c04722.

Assessing the performances of the fixed pivot technique vs. the finite volume scheme in modeling multi-dimensional breakage

Suet Lin Leong[1], Yong Kuen Ho[1,2]
[1]Department of Chemical Engineering, School of Engineering, Monash University Malaysia, Jalan Lagoon Selatan, Bandar Sunway, 47500 Selangor, Malaysia.
[2]Monash-Industry Plant Oils Research Laboratory (MIPO), Monash University Malaysia, Jalan Lagoon Selatan, Bandar Sunway, 47500 Selangor, Malaysia
Corresponding author email: suet.leong@monash.edu

ABSTRACT

When modeling particle breakage, the use of a single dimension to characterize the particulate system is inadequate to account for both the variations in particle shapes and sizes. In this regard, effectively modeling multi-dimensional breakage using the population balance equation (PBE) requires the utilization of accurate and efficient numerical techniques. Amongst many potential numerical techniques, the Fixed Pivot Technique (FPT) and Finite Volume Schemes (FVS) are popular choices to resolve multi-dimensional breakage PBEs. However, whether there exists a general multi-purpose technique between the two remains unclear. Across all test cases with identical size domain and mesh, while both techniques exhibit comparable accuracy in resolving the moments, and exhibit similar computational efficiency (time taken by FPT relative to FVS is of $\sim \mathrm{O}(10^0)$), the choice of numerical technique is contingent upon the properties where accurate prediction is critical. To this end, FVS is the preferred choice when precise estimation of up to two properties is required owing to its simplicity, albeit requiring distinct schemes for different properties. Conversely, when more than two properties are crucial, the FPT is more suited as it preserves up to four properties in 2D. Overall, this work offers rational guidance for efficient and accurate modeling of multi-dimensional breakages.

Keywords: multi-dimensional; population balances; breakage; fixed pivot technique; finite volume scheme

1. INTRODUCTION

Breakage is a phenomenon that results in the production of two or more smaller-sized daughter particles from a larger parent particle. While the use of a single internal coordinate (e.g., volume-equivalent diameter) to characterize a particulate system is common and convenient, crucial characteristics of particulate system are often multi-dimensional in reality. Therefore, in cases where tracking the behavior of a particle population with two internal coordinates is crucial, a traditional one-dimensional PBE is no longer adequate, demanding the use of a two-dimensional (2D) or Bivariate Population Balance Model (2D-PBM).

Solving multi-dimensional PBEs is a non-trivial task fraught with complexities due to their partial integro-differential nature. While the method of moments and its variants are simple, computationally inexpensive, and capable of predicting the moments of distributions with high accuracy, they are not designed to capture the dynamics of the entire particle size distribution and renders additional processing to reconstruct the number distribution. To this end, the FPT and FVS have emerged as appealing techniques for solving multi-dimensional breakage PBEs, owing to their ability to accurately predict the transients of the complete number density and moments with reasonable computational efficiency. However, an objective comparison of their performances is lacking. In the literature, 2D FPT was only investigated for pure aggregation and simultaneous aggregation and breakage problems, but pure breakage problems were not adequately studied (Vale and McKenna, 2005, Chakraborty and Kumar, 2007, Nandanwar and Kumar, 2008). In contrast, the simple implementation of FVS schemes by Saha et al. (2019), which conserves up to two moments, have proven promising. However, it remains to be seen how the formulation of FVS affects its performance, as opposed to the 2D FPT which preserves up to four properties, as far as solving multi-dimensional breakage PBEs is concerned. Insofar, a clear and objective assessment between the FPT and FVS is imperative for a more informed knowledge of their performances for solving multi-dimensional PBEs.

In this work, the performances the FPT (Kumar and Ramkrishna, 1996) and FVS (Scheme 2b of Saha et al. (2019)) are compared and examined with the aim of providing valuable insights into their numerical

capabilities and limitations for solving multi-dimensional breakage PBEs. The techniques are assessed using relative error indicators and are benchmarked against analytical solutions.

2. COMPUTATIONAL SETTINGS

2.1. Model Configuration

In this work, we employ a finite domain of internal coordinates v and w of range $[v_{\min}, v_{\max}] \times [w_{\min}, w_{\max}] = [10^{-9}, 2] \times [10^{-9}, 2]$. For all case studies, we employ a geometric mesh with 25×25 grid points (geometric ratio ≈ 3) across the computational domain. Additionally, we adopt a monodisperse initial distribution $n(v, w, 0) = \delta(v - v_{\max}) \delta(w - w_{\max})$. The solutions were computed on a workstation equipped with an Intel® Core™ i5-1135G7 CPU with a clock speed of 2.40 GHz and 16 GB installed memory.

2.2. Case Studies and Performance Indicators

We evaluate the performance of the FPT and FVS by testing them against known solutions. Here, 2D breakages that conserve the first-order moments are studied, as tabulated in Table 1. Due to the absence of analytical solutions for number density, we benchmarked the numerical solutions for moments.

Table 1. *Cases employed in this study.* $\beta(v, w, v', w')$ *is the stoichiometric kernel for particle of size* (v, w) *due to the breakage of parent particle of size* (v', w'), $\Gamma(v, w)$ *is the breakage rate kernel,* $M_{\lambda\mu}^{ana}(t)$ *is the analytical moments of order* λ *and* μ *with respect to* v *and* w, *respectively, and* $v_{\max}$ *and* $w_{\max}$ *are the maximum sizes in the computational domain. Analytical moments are obtained from Saha et al., 2019.*

Case	$\beta(v, w, v', w')$	$\Gamma(v, w)$	Analytical Moments, $M_{\lambda\mu}^{ana}(t)$
1	$\dfrac{2}{v'w'}$	1	$M_{\lambda\mu}^{ana}(t) = v_{\max}^{\lambda} w_{\max}^{\mu} \exp\left[\left(\dfrac{2}{(\lambda+1)(\mu+1)} - 1\right)t\right]$
2	$\dfrac{2}{v'w'}$	$v + w$	$M_{00}^{ana}(t) = 1 + (v_{\max} + w_{\max})t$ $M_{10}^{ana}(t) = v_{\max}$, $M_{01}^{ana}(t) = w_{\max}$

Note that the internal coordinates need not be size related, where they can represent other properties of the particle, such as size and composition, or mass and energy. These entities are expected to be conserved upon binary breakage (Cases 1-2). The results are assessed using the following time-averaged relative error:

$$\sigma_{\lambda\mu} = \frac{1}{F} \sum_{j=1}^{F} \left| \frac{M_{\lambda\mu}^{ana}(t_j) - M_{\lambda\mu}^{num}(t_j)}{M_{\lambda\mu}^{ana}(t_j)} \right| \tag{1}$$

where F is the total number of time points. The superscript '*ana*' denotes analytical and '*num*' denotes either FPT and FVS.

3. RESULTS AND DISCUSSION

Figure 1a shows that both the FPT and FVS predict the zeroth moment satisfactorily for size-independent breakage (Case 1), demonstrating similar performance with $\sigma_{00} \sim \mathrm{O}(10^{-3})$ across different meshes. Interestingly, the FVS outperforms the FPT in predicting the first-order moments, with $\sigma_{10} + \sigma_{01} \sim \mathrm{O}(10^{-13})$ compared to the FPT, with $\sim \mathrm{O}(10^{-5})$. This can be attributed to the intrinsic characteristic of the FVS (Scheme 2b of Saha et al. (2019)) as it was devised to conserve the first-order moments. However, the FVS shows poor accuracy in predicting the hypervolume M_{11}, with $\sigma_{11} \sim \mathrm{O}(10^{-1})$, whereas the FPT achieves an error of $\sigma_{11} \sim \mathrm{O}(10^{-10})$, indicating better performance. Therefore, while the FVS is simple to implement with reasonable accuracy, it suffers issues in resolving higher-order moments, which are important properties (e.g., the total area of particles) for certain applications. In this regard, the FPT would be a more suitable choice if more than two moments are crucial. For size-dependent breakage (Case 2), on the other hand, both the FPT and FVS show good agreement with the analytical zeroth moment with an error of $\sigma_{00} \sim \mathrm{O}(10^{-4})$ and $\sim \mathrm{O}(10^{-2})$, respectively, as seen in Figure 1b. Further, quantitative results indicate that the FVS outperforms

the FPT in predicting the first-order moments, achieving a remarkable average relative error of $\sigma_{10} + \sigma_{01} \sim O(10^{-15})$ compared to $\sim O(10^{-4})$ by the FPT. As for the computation times, results indicate that, for both cases, the two methods are comparable, taking $\sim 2\,\mathrm{s}$ to resolve the simulation up to $t = 10$.
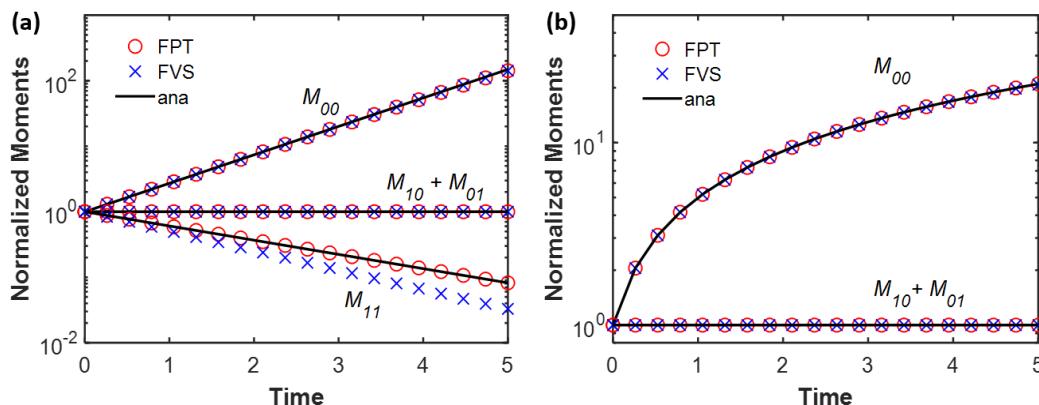

Figure 1. (a) Case 1 and (b) Case 2: A comparison between the FPT and FVS against analytical solution, in predicting the moments of distribution $M_{\lambda\mu}$ of order λ and μ with respect to v and w, respectively. The moments are normalized against the initial analytical moments of identical order.

4. CONCLUSIONS

In this study, we evaluate the performance of two state-of-the-art techniques, i.e., FPT and FVS, for solving pure breakage 2D-PBEs. Our results reveal that, while both the FPT and FVS exhibit relatively comparable accuracy in predicting the moments of distributions and in their computation times, the selection of numerical technique hinges on the properties/moments that necessitate precise estimation. When up to two important moments are critical for observation, the FVS is the preferred option attributing to its simpler formulation, although necessitating distinct schemes for conserving different properties. In contrast, the more complex FPT offers versatility by effectively balancing accuracy and the ability to preserve up to four properties in 2D, rendering it adequate for general usage. Further, for the conservation of other properties, the FPT formulation is flexible in adapting to the properties of choice, whereas the FVS requires redesign. Equipped with an understanding of the capabilities of numerical techniques in solving multi-dimensional breakage PBM, we can anticipate an increased utilization of the population balance model for precise control over the dynamics of multi-dimensional particles across a diverse range of applications.

REFERENCES

Chakraborty, J. & Kumar, S. 2007. A new framework for solution of multidimensional population balance equations. *Chemical Engineering Science,* 62**,** 4112-4125. doi: https://doi.org/10.1016/j.ces.2007.04.049

Kumar, S. & Ramkrishna, D. 1996. On the solution of population balance equations by discretization—I. A fixed pivot technique. *Chemical Engineering Science,* 51**,** 1311-1332. 10.1016/0009-2509(96)88489-2

Nandanwar, M. N. & Kumar, S. 2008. A new discretization of space for the solution of multi-dimensional population balance equations: Simultaneous breakup and aggregation of particles. *Chemical Engineering Science,* 63**,** 3988-3997. 10.1016/j.ces.2008.04.054

Saha, J., Das, N., Kumar, J. & Bück, A. 2019. Numerical solutions for multidimensional fragmentation problems using finite volume methods. *Kinetic and Related Models,* 12**,** 79-103. 10.3934/krm.2019004

Vale, H. M. & Mckenna, T. F. 2005. Solution of the Population Balance Equation for Two-Component Aggregation by an Extended Fixed Pivot Technique. *Industrial & Engineering Chemistry Research,* 44**,** 7885-7891. 10.1021/ie050179s

Modeling mass- and number- expending fragmentation using the modified moving grid technique

Simon Ing Xun Tiong[1] and Yong Kuen Ho[1,2]

[1]Department of Chemical Engineering, School of Engineering, Monash University Malaysia, Jalan Lagoon Selatan, 47500 Bandar Sunway, Selangor, Malaysia

[2]Monash-Industry Plant Oils Research Laboratory, Monash University Malaysia, Jalan Lagoon Selatan, Bandar Sunway, 47500 Selangor, Malaysia

Corresponding author email: simon.tiong@monash.edu

ABSTRACT

Under external forces, particles may experience fragmentation while at the same time lose their mass through shrinkage, and ultimately dissolve into the continuous phase. However, the mass- and number-expending processes cause the tracking of the particle size distribution to be highly non-trivial. In this work, a comprehensive sectional scheme that combines the Fixed Pivot (FP) discretization and moving grid system, called the modified moving-grid technique (m-MGT), is introduced to resolve the PBEs that involve fragmentation, shrinkage and dissolution.

Keywords: population balances, moving grid, grid elimination, mass-expending, number-expending

1. INTRODUCTION

Mass- and number- expending fragmentation is a pivotal particulate phenomenon observed in various processes such as the processing of pharmaceutical substances. In this process, particles lose mass through shrinkage while simultaneously undergoing fragmentation. As time progresses, particles will eventually undergo dissolution and vanish, resulting in a decrease in total particle count. To model this process, Population Balance Equations (PBE) that characterizes the temporal evolution of the number density of the dispersed phase entities, is the fundamental approach. However, due to the intricacy exhibited by the mass- and number- decreasing fragmentation PBE, i.e., Eq. (1), in the form of hyperbolic partial-integro differential equation, generalized analytical solutions are not commonly available.

While there is a substantial number of numerical methods available for solving the pure fragmentation PBEs and size expanding classes of PBEs, the literature is sparse when it comes to finding the numerical solution to the PBEs that involve fragmentation, shrinkage and dissolution. There are only some recent works which addressed the simultaneous fragmentation and shrinkage PBEs (Bertin et al., 2016; Wu et al., 2017; Yuan et al., 2012). A successful numerical approximation of PBEs also hinges on the preservation of the fundamental moment-based properties. In this regard, the state-of-the-art sectional technique, i.e., the Moving Grid (MG) technique developed by Kumar and Ramkrishna (1997) is a compelling strategy as it preserves moments and is free from numerical diffusion. In this study, we present a modified Moving Grid technique (m-MGT), which incorporates a left moving grid to reflect shrinkage while eliminating grid points to realistically mimic dissolution and uses the principle of FP to ensure the preservation of important moments (Tiong et al., 2023).

$$\frac{\partial n(v,t)}{\partial t} + \frac{\partial}{\partial v}[c(v)n(v,t)] = \int_v^\infty \beta(v,w)\Gamma(w)n(w,t)dw - \Gamma(v)n(v,t) \qquad (1)$$

2. THEORETICAL FRAMEWORK

2.1. Discrete Equations for Simultaneous Shrinkage, Dissolution and Fragmentation

The fundamental framework of the MG technique is built upon the synergy between the method of characteristics and the FP discretization. In particular, the shrinkage term is handled by the method of characteristics whereas the breakage terms are dealt with by the FP technique (Kumar and Ramkrishna, 1996), on the condition that the grid points, which represent the particle sizes, are now a function of time. For simplicity, we write the grid specific variables: $x_i(t)$ and $v_i(t)$ as x_i and v_i, and also present the final

implementable formulation in this section. Discretizing the simultaneous shrinkage, dissolution and fragmentation PBEs gives the following

$$\frac{dN_i(t)}{dt} = \sum_{k=i}^{M} \eta_{ik} \Gamma_k N_k(t) - \Gamma_i N_i(t) \tag{2}$$

Here, N_i is the number of particles in the i-th bin, M is the numbering of the final bin. The mean value theorem is employed to compute the average number density, i.e., $n_i = N_i/(v_{i+1} - v_i)$. Moreover, η_{ik} is the fractional allocation of particles due to fragmentation. For the exact preservation of the zeroth and the first moments (total mass and number, respectively), η_{ik} is given by

$$\eta_{ik} = \int_{x_i}^{x_{i+1}} \left[\frac{x_{i+1}-v}{x_{i+1}-x_i}\right] \beta(v, x_k)dv + \int_{x_{i-1}}^{x_i} \left[\frac{v-x_{i-1}}{x_i-x_{i-1}}\right] \beta(v, x_k)dv \tag{3}$$

where x_i is the i-th grid points or the representative sizes for the i-th bin, $\beta(v, x_k)$ is the daughter distribution function. In addition, the shrinkage term is considered through the following equations:

$$\frac{dv_i}{dt} = c(v_i) \tag{4}$$

$$\frac{dx_i}{dt} = c(x_i) \tag{5}$$

Here, $c(\cdot)$ is the shrinkage rate and v_i are the bin boundaries. Equations (4) and (5) suggest that both v_i and x_i travel at the velocity equivalent to the shrinkage rate, which is always negative. However, the left-moving grid here presents a new challenge unprecedented in the earlier work. It causes the grid points to intersect at zero and move into the negative domain due to dissolution. Thus, special considerations are needed here.

2.2. Strategy for Resolving the Dissolution of Particles
As alluded to in the preceding section, the left moving grid requires a proper refinement such that it can accurately capture the decline in particle count due to dissolution of particles when their sizes approach asymptote zero. We address the issue by discarding the existing bin one by one at predesignated temporal intervals. To provide a clear and concise picture of the approach, we herein consider that all particles in the system are arbitrarily larger than asymptote zero, which we approximate using the point of dissolution of 1e-8. Dissolution occurs when v_1 coincides at the point due to continuous shrinkage. The time frame before dissolution occurs, t_s can be determined as follows:

$$\int_0^{t_s} dt = \int_{v_1}^0 c(v_1)dv \tag{6}$$

Evidently, both x_i and v_i will start crossing over into the negative domain without any particular treatment. To resolve this, we first restrict the movement of v_1 by assigning a velocity of zero, i.e., $dv_1/dt = 0$. On the other hand, the velocity of x_1 is also modified so that it stays in the middle of the first bin

$$\frac{dx_i}{dt} = \frac{1}{2}\left(\frac{dv_1}{dt} + \frac{dv_2}{dt}\right) \tag{7}$$

Following this, Eqs. (2)-(5) together with Eqs. (6) and (7) are computed over a specific time interval, Δt until v_2 intersects at zero. This time interval can again be evaluated using the concept presented in Eq. (6), i.e., $\int_{t_s}^{t_s+\Delta t} dt = \int_{v_2}^0 c(v_2)dv$. At this point, the first bin is eliminated because v_1, x_1 and v_2 coincides at zero concurrently, which implies that the particles here are completely dissolved. The remaining bins are now renumbered, and the process persists until either the designated simulation duration is reached or all the bins are eliminated.

3. RESULTS AND DISCUSSION
To exemplify the capability of the m-MGT, we assess the numerical results against the established analytical solutions for simultaneous shrinkage, dissolution and fragmentation PBEs with an exponential initial condition. For easier interpretation, the time scale is standardized against the time at which 99% of the initial mass is depleted and the moments are normalized against their respective initial moments. Fig. 1(a)-(c) show the results for fragmentation dominant scenario whereas Fig. 1(d)-(e) display the results for shrinkage prominent scenario. Figure 1a) and d) show that the m-MGT provides accurate predictions for the transients of the number density until the very late phase where 99% of the mass is exhausted. The number density distribution in a) is shifted towards the left due to the substantial size reduction as a result of fragmentation

predominance. The accurate approximations of the zeroth moment in Figure 1b) and e) suggest that the bin elimination routine captures the dynamics of the particle number satisfactorily. Notably, for the fragmentation dominant case, the total number count shows an initial increase, indicating the dominance of fragmentation in the early phase. The decline at the middle stage is due the inherent nature of the system, which shrinkage prevails over fragmentation as the particles become smaller. On the other hand, for the shrinkage dominant case, the particle count continues to decline throughout the process. Furthermore, it is worth noting that the continuous left moving grid allows the decline in the first moment or the total mass of the particle population to be precisely estimated. The simulation results here suggest that the m-MGT robustly handles the simultaneous shrinkage, dissolution, and fragmentation process even in the asymptotic scenarios where either shrinkage or fragmentation is dominant.
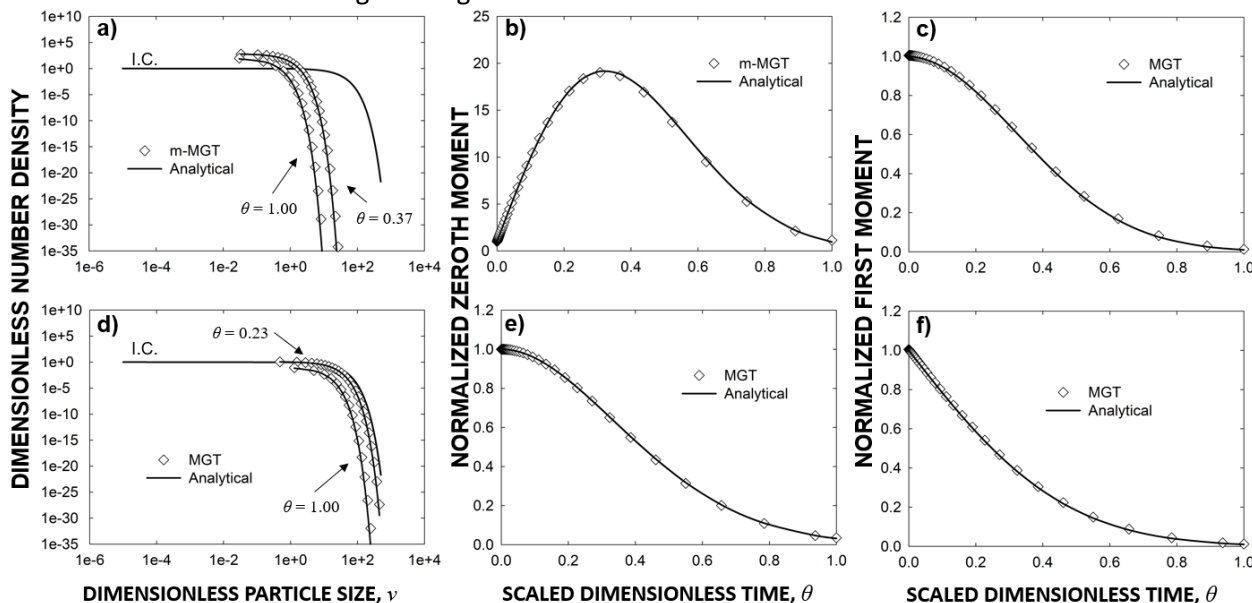

Figure 1. *Comparison of fragmentation-dominant scenario (a-c) and shrinkage-prominent (d-f) scenarios against the analytical solution with coefficients of c(v) = - 0.1 and -100 respectively, fragmentation rate of Γ(v) = v and stoichiometric kernel of β(v,w) = 2/w*

4. CONCLUSIONS

The m-MGT proposed in this work resolved the unique challenges posed in accurately simulating the dynamics of particles experiencing shrinkage, dissolution, and fragmentation concomitantly. All the features, i.e., the continuous moving grid, stepwise bin elimination at the lower end of the particle size spectrum and FP discretization, are crucial to ensure the accurate predictions of the number density profiles and important moments of interest. As the current work only includes the size-diminishing process, there is a potential requirement for further modifications and advancement to incorporate size-expanding processes such as growth and aggregation.

REFERENCES

Bertin, D., Cotabarren, I., Piña, J. and Bucalá, V., 2016. Population balance discretization for growth, attrition, aggregation, breakage and nucleation. *Computers & Chemical Engineering*, *84*, pp.132-150. doi: https://doi.org/10.1016/j.compchemeng.2015.08.011

Kumar, S. and Ramkrishna, D., 1996. On the solution of population balance equations by discretization—I. A fixed pivot technique. *Chemical Engineering Science*, *51*(8), pp.1311-1332. doi: https://doi.org/10.1016/0009-2509(96)88489-2

Kumar, S. and Ramkrishna, D., 1997. On the solution of population balance equations by discretization—III. Nucleation, growth and aggregation of particles. *Chemical Engineering Science*, *52*(24), pp.4659-4679. doi: https://doi.org/10.1016/S0009-2509(97)00307-2

Tiong, S.I.X., Ahamed, F., Sitaraman, H., Leong, S.L. and Ho, Y.K., 2023. Modeling simultaneous particle shrinkage, dissolution and breakage using the modified moving grid technique. *Powder Technology*, *421*, p.118439. doi: https://doi.org/10.1016/j.powtec.2023.118439

Wu, S., Yapp, E.K., Akroyd, J., Mosbach, S., Xu, R., Yang, W. and Kraft, M., 2017. A moment projection method for population balance dynamics with a shrinkage term. *Journal of Computational Physics*, *330*, pp.960-980. doi: https://doi.org/10.1016/j.jcp.2016.10.030

Yuan, C., Laurent, F. and Fox, R.O., 2012. An extended quadrature method of moments for population balance equations. *Journal of Aerosol Science*, *51*, pp.1-23. doi: https://doi.org/10.1016/j.jaerosci.2012.04.003

A data and physics driven approach to understand dispersion making devices

Anjali Kumari[1], Adam Kowalski[2], Sanjeev Kumar[1]
[1]Department of Chemical Engineering, Indian Institute of Science, Bengaluru, India
[2]R&D Port Sunlight Laboratory, Unilever, Bebington, UK
Corresponding author email: anjalikumari@iisc.ac.in

ABSTRACT

Dispersion-making devices are known to produce bimodal and other more complex shaped size distributions, starting with initial monomodal distributions. Unfortunately, even empirical breakup frequencies and daughter size distribution functions for real-time control are unavailable. This study presents a new method: identification of distinct drop breakup modes and assigning them unknown weights and parameters through Genetic Algorithms driven fit to evolving size distribution data. The approach can potentially identify active breakup modes and map them to physical zones in a device based on the required flow field for a breakup mode to exist. We focus on the primary-secondary mode observed in shear fields. The developed daughter size distribution function captures the transition from monomodal to bimodal sizes with the help of a specific error estimator for the Genetic Algorithms optimizer.

Keywords: population balance model; high shear mixers; bimodal DSDs; fixed pivot technique

1. INTRODUCTION

The size distribution of fine drops in an emulsion influences its stability, texture, and appearance. Despite a minimal increase in energy during emulsion formation (0.02% to 0.06% of total input), sustaining a complex flow field is energy intensive. The lower limit on necessary energy is unknown. Minimizing it for a target drop size distribution is a key goal. Evolving size distributions in industrial units rarely follow a self-similar pattern, making traditional approaches ineffective. Fitting data to empirical breakage functions for mixer control does not address energy efficiency improvements through modified internals.

We propose a framework based on literature findings, highlighting characteristic features in various drop breakup modes. For instance, within a shear field, a drop can break into two primary and several secondary drops (Cristini et al., 2003). The evolving size distribution captures cumulative features from all active breakup modes in a device. The weighted contribution of these modes—active, dormant, or simultaneous—changes over time with the evolving size distribution. Using the population balances framework, we predict the size distribution for multiple breakup modes, employing a set of functions tailored to operating modes. Our focus is on high-shear devices, identifying a minimal set of governing drop breakup modes. Genetic Algorithm is used to fine tune the description of operating breakup modes for a given set of evolving size distributions and determine wights of operating breakup modes. The mapping of the operating modes to device is the next step for design modification.

In summary, this research focuses on the nuanced exploration of active breakup modes within a dispersion device using the evolving size distributions. By deciphering the operating fundamental modes and optimizing their parameters through design modification, the proposed framework seeks to enhance our understanding of emulsion formation and development of energy efficient devices in industrial applications.

2. METHODS

We combine functions for the expected modes of drop breakup with weights assigned to each one to fit experimentally measured evolving size distributions. The population balance equation for a well-mixed system is discretized using the fixed pivot technique of Kumar and Ramakrishna (1996). For multiple modes of drop breakup operating concurrently and independently (assumed), the discretized equation takes the following form:

$$\frac{dN_i(t)}{dt} = -\left(\sum_{all\ j} w_j \Gamma_i{}^j\right)N_i(t) + \sum_{k=i}^{M} \beta_{i,k}\left(\sum_{all\ j} w_j \Gamma_k{}^j\right)N_k(t)\ ,\ \ i = 1\ to\ M \tag{1}$$

$$\beta(v, v') = \sum_{all\ j} w_j \beta_j(v, v')$$

Here, N_i is the population of drops at i[th] pivot per unit volume, Γ_i their breakup frequency, and $\boldsymbol{\beta_{i,k}}$ the number of drops formed at i[th] pivot size when drops at k[th] pivot break. The $\boldsymbol{w_j}$ denotes the weight assigned to j[th] mechanism.

We consider four distinct drop breakup modes: 1) unequal binary breakup, 2) primary-secondary breakup, 3) erosion, and 4) shattering, depicted in Figure 1(a). Each mode is represented by a unique non-overlapping family, mathematically expressed through a parameterized function allowing precise adjustments within a broad class. Unlike employing a polynomial basis set for the daughter size distribution function (Sathyagal et al., 1995), the selected modes represent the varied physics of drop breakup in dispersion devices reported in the literature. The primary-secondary breakup mode, $\boldsymbol{\beta^2(v, v')}$, elucidates the disintegration observed in shear fields (Cristini *et al.,* 2003). Here, a parent drop undergoes division into two primary drops, and multiple secondary drops. The daughter-size distribution function, shown in Figure 1(b), is the first attempt in this direction. This function contains parameters for the number of secondary drops formed, the volume of secondary drops, and a shape parameter for the distribution of secondary drops. The widely used model in the literature for binary unequal breakup developed by Diemer and Olson (2002) characterizes the first mode of breakup shown in Fig. 1(a). The parameters in the functions are determined using GA. The latter however required the development of a novel objective function from data-driven learning (using experimental data) to facilitate the successful convergence of GA optimizers. The error estimator addresses the challenge faced by near zero discretized populations as the GA driven iterations continue to march towards convergence.
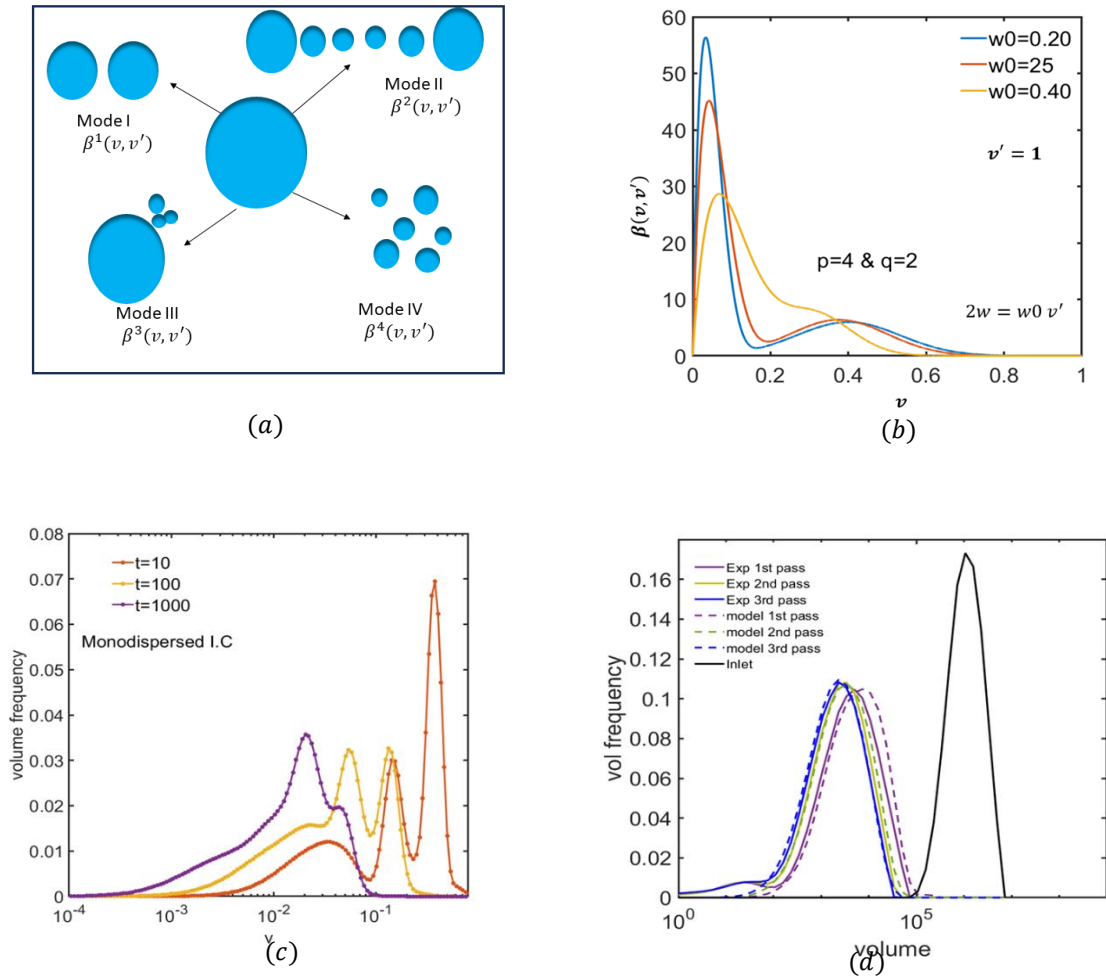

(a)

(b)

(c)

(d)

Figure 1. *(a) The four basic modes of drop breakup. (b) Primary secondary drop breakup daughter size distribution for various values of parameters. (c) Generation of bimodal size distributions using primary secondary daughter size distribution function from monodispersed I.C and power law breakup frequency. (d) Data from Hert and Rodgers (2017) predicted using modes.*

3. RESULTS AND DISCUSSION

The outcome of particular significance pertains to the primary-secondary mode of drop breakup. The daughter size distribution function characteristic of this mode exhibits a diverse range of potential shapes, as visually illustrated in the accompanying figures. Commencing with an initial monodisperse size distribution and applying the simplest power law breakage frequency, the mode facilitates the generation of bimodal and multimodal size distributions, shown in Figure 1(c). The continued refinement of the kernel model has been prompted by the necessity to accommodate additional physics. This includes scenarios where varying numbers of secondary drops are formed from parent drops of differing sizes while maintaining a consistent mean size for secondary drops. This model refinement validates experimental findings reported in the literature (Hert & Rodgers, 2017), thus affirming the active participation of specific breakup modes within mixing processes. Figure 1(d) shows the prediction of the drop size distribution for experimental data (Hert & Rodgers, 2017) using the basic modes formulation. The contribution from the primary-secondary mode is 20%, and 80% from the unequal binary breakup when only the first and second modes were active. The small peak on the smaller drop side was not captured even by allowing two modes to be active.

4. CONCLUSIONS

We solve the inverse problem of population balance by introducing "basic modes" of drop breakup. Distinguishing our work from existing studies, these modes offer a more comprehensive understanding of the intricate droplet fragmentation mechanisms at play in a device. Robust mathematical models are developed to represent these basic modes, with parameter estimation facilitated through the application of genetic algorithms. The intriguing phenomenon observed in high shear mixing scenarios is the transformation of an initially monomodal droplet size distribution into a bimodal distribution, a behavior challenging to predict using conventional breakage functions. Nevertheless, our approach exhibits promise in comprehending such intricate evolutions. The results demonstrate the potential of the proposed approach to unravel the complexities of drop size distribution evolution in emulsification processes within mixers. A further emphasis is drawn on the importance of appropriate objective functions for this problem, which alone can lead to convergence and estimation of parameters while solving inverse problems using an optimizer.

REFERENCES

Cristini, V., Guido, S., Alfani, A., Bławzdziewicz, J., & Loewenberg, M. (2003). Drop breakup and fragment size distribution in shear flow. Journal of Rheology, 47(5), 1283-1298. https://doi.org/10.1122/1.1603240

De Hert, S. C., & Rodgers, T. L. (2017). On the effect of dispersed phase viscosity and mean residence time on the droplet size distribution for high-shear mixers. Chemical Engineering Science, 172, 423-433. https://doi.org/10.1016/j.ces.2017.07.002

Diemer, R. B., & Olson, J. H. (2002). A moment methodology for coagulation and breakage problems: Part 3—generalized daughter distribution functions. Chemical Engineering Science, 57(19), 4187-4198. https://doi.org/10.1016/S0009-2509(02)00366-4

Kumar, S., Ganvir, V., Satyanand, C., Kumar, R., & Gandhi, K. S. (1998). Alternative mechanisms of drop breakup in stirred vessels. Chemical Engineering Science, 53(18), 3269-3280.Doi: https://doi.org/10.1016/S0009-2509(98)00139-0

Kumar, S., & Ramkrishna, D. (1996). On the solution of population balance equations by discretization—I. A fixed pivot technique. Chemical Engineering Science, 51(8), 1311-1332. https://doi.org/10.1016/0009-2509(96)88489-2

Sathyagal, A. N., Ramkrishna, D., & Narsimhan, G. (1995). Solution of inverse problems in population balances-II. Particle break-up. Computers & chemical engineering, 19(4), 437-451. https://doi.org/10.1016/0098-1354(94)00062-S

Population balance modeling of propylene polymerization process in a multi-zone circulating reactor

Ya-Nan Yang [1], Hui Liu [2] and Li-Tao Zhu[1], Jie Jin[1], Xi-Bao Zhang [1]*, Zheng-Hong Luo [1]*

[1] Department of Chemical Engineering, School of Chemistry and Chemical Engineering, State Key Laboratory of Metal Matrix Composites, Shanghai Jiao Tong University, Shanghai 200240, P. R. China

[2] Shandong Chambroad Petrochemicals Co., Ltd, Binzhou 256599, P. R. China

Corresponding author email: 13127935995@sjtu.edu.cn

Corresponding author email: luozh@sjtu.edu.cn

ABSTRACT

The multi-zone circulating reactor (MZCR) technology is an emerging and advanced olefin polymerization process, which allows the production of intimate mixtures of polyolefins with widely varying properties. In this study, a multi-model coupling method is proposed to understand the characteristics of gas-phase propylene polymerization in a multizone circulating reactor. The developed model which couples the kinetic-based moment method, the chain length distribution model and the steady-state population balance model can be used to simultaneously account for the molecular and particle properties of polypropylene within the whole MZCR. Three key operating variables linked to product properties involving gas barrier conditions, catalyst conditions, and gas velocities are examined. The simulation results demonstrate that a wide range of polymer properties can be obtained by varying the reactor operating conditions. The MZCR technology offers tremendous advantages in flexibly tuning the molecular and particle properties of products as compared to the conventional fluidized beds, loop reactors and stirred bed reactors. The current study can offer some guidance for tailoring polymers with specific particle size and molar mass distributions.

Keywords: multi-zone circulating reactor; gas-phase propylene polymerization; method of moments; population balance model; chain length distribution

1. INTRODUCTION

The preparation of propylene within the multi-zone circulating reactor (MZCR) is an advanced technology, which greatly improves the property of polymers (Govoni and Mei, 2001). Applying versatile modeling methods to investigate particle-size-related properties have received extensive attention with the rapid development of computer technology. In this work, a coupled model integrating the kinetic-based moment method, the chain length distribution model, and the steady-state PBM is developed. The impacts of gas barrier, catalyst conditions and riser gas velocities on the molecular and particle properties of the resulting polymers within the whole MZCR are investigated.

2. MATERIALS AND METHODS

2.1. Propylene polymerization kinetics and MZC Reactor model

Herein, a kinetic model is developed for propylene polymerization catalyzed by the Ziegler-Natta catalyst (Zacca and Ray, 1993). The polymerization mechanism involves the formation of active sites, initiation of active sites, chain propagation, chain transfer and chain deactivation. The mathematical equations for the monomer can be derived as follows (Fernandes and Lona, 2004):

$$\frac{dM}{dz} = -\frac{R_p(1-\varepsilon^r)}{u_0\varepsilon^r} = -\frac{R_p(1-\varepsilon^r)}{u_g} \tag{1}$$

where M denotes monomer, z represents the length along the reactor tube, ε^r is bed porosity in the riser, and u_g represents gas velocity.

2.2 Steady-state population balance model

Following Levenspiel et al. (Levenspiel et al, 1968) the particle-size distribution in the MZCR can be described by the following closure equation (Luo et al., 2009; Santos et al., 2006):

$$\int_{D_0}^{D_{max}} P_b(D)dD = 1 \tag{2}$$

The steady-state mass balance equation for the particle size between *D, D+ΔD* can be described by equation (3). The model mainly takes into account the effect of particle growth and attritions on particle size.

$$\begin{Bmatrix} \text{Particles entering} \\ \text{with catalyst feed} \end{Bmatrix} - \begin{Bmatrix} \text{Particles leaving in} \\ \text{the outflow stream} \end{Bmatrix} + \begin{Bmatrix} \text{Particles entering the} \\ \text{interval from a smaller} \\ \text{size due to polymerization} \end{Bmatrix} -$$

$$\begin{Bmatrix} \text{Particles leaving the} \\ \text{interval to a larger size} \\ \text{due to polymerization} \end{Bmatrix} + \begin{Bmatrix} \text{Particles entering the} \\ \text{interval from larger} \\ \text{size due to attrition} \end{Bmatrix} - \begin{Bmatrix} \text{Particles leaving the} \\ \text{interval to a smaller} \\ \text{size due to attrition} \end{Bmatrix} +$$

$$\begin{Bmatrix} \text{Generation of particle mass} \\ \text{within the interval } D, D + \Delta D \\ \text{due to polymerization} \end{Bmatrix} - \begin{Bmatrix} \text{Loss of particle mass} \\ \text{within the interval } D, D + \Delta D \\ \text{due to attrition} \end{Bmatrix} = 0 \tag{3a}$$

$$F_c P_c(D_i)\Delta D - F_1 P_b(D_i)\Delta D + W_b P_b(D_{i-1})R_p(D_{i-1}) - W_b P_b(D_i)R_p(D_i) + W_b P_b(D_{i+1})R_a(D_{i+1}) - W_b P_b(D_i)R_a(D_i) +$$

$$W_b \frac{3R_p(D_i)}{D_i}P_b(D_i)\Delta D - W_b \frac{3R_a(D_i)}{D_i}P_b(D_i)\Delta D = 0 \tag{3b}$$

Then, the equation (3b) is solved to yield:

$$P_b(D) = \begin{cases} 0 & D \leq D_0 \\ \frac{F_c}{W_b R_r(D)}\left(\frac{D}{D_0}\right)^3 I(D, D_0^+) & D_0^+ \leq D \leq D_{max} \\ 0 & D > D_{max} \end{cases} \tag{4}$$

$$R_r(D) = R_p(D) - R_a(D) \tag{5}$$

$$I(D, D') = exp\left(-\int_{D'}^{D} \frac{F_1}{W_b R_r(D'')} dD''\right) \tag{6}$$

The above equation (4) is the analytical solution form of the particle density function ($P_b(D)$) for the case of uniform-size catalyst feed. *F* represents the mass flow rate, with the subscript 1 denoting product discharging and *c* indicating the catalyst. W_b is the bed weight, *D* is the particle size with the subscript 0 denoting the initial size and max indicating the maximum size, R_a is the attrition rate and R_p is particle growth rate.

3. RESULTS AND DISCUSSION

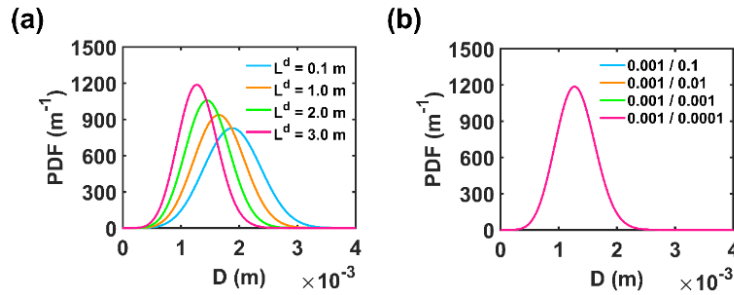### 3.1 Propylene polymerization in the MZC reactor with gas barriers

Figure 1. Instantaneous particle size distribution of polymers for: (a) different parts of the reactor and (b) different settings of gas barrier.

Herein, the effect of gas barrier on the molar mass of resulting polymers is investigated while the other operating conditions remain unchanged. The particle size distribution of polymers at various parts in the downer is illustrated in **Figure 1** (a).

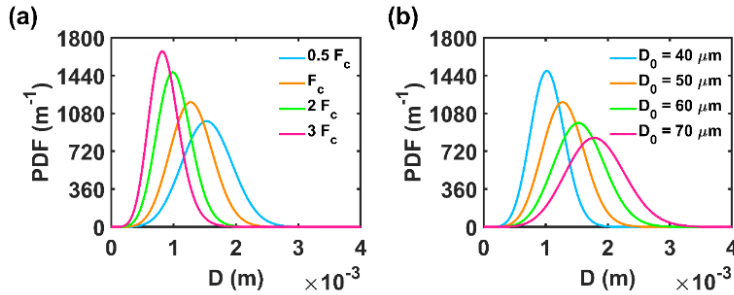### 3.2 Propylene polymerization under various catalyst conditions

Figure 2. Instantaneous particle size distribution of polymers for: (a) different catalyst flow rates, and (b) different initial size of catalyst.

The catalyst flow rate determines the concentration of active sites, which further affects the polymerization rates as well as the molar mass of polymers. Furthermore, the particle size of resulting polymers is strongly

dependent on the initial size of the catalyst particles. **Figure 2** demonstrates the effect of the catalyst flow rates and initial catalyst size on the instantaneous particle size distribution at the outlet of the downer.

3.3 Propylene polymerization under various gas velocities

Herein, several simulation cases with gas velocities in the range of 3 m/s to 15 m/s are implemented to investigate the influence of riser gas velocities on the instantaneous particle size distribution of product, as seen in **Figure 3**.
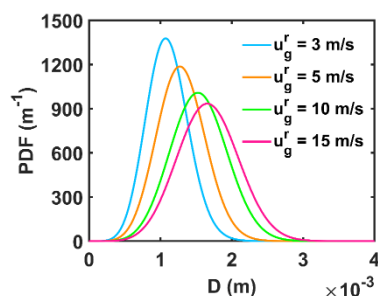

Figure 3. Instantaneous particle size distribution of polymers at different riser gas velocities.

4. CONCLUSIONS

A comprehensive model coupling the kinetic-based moment method, the distributed characteristics model and the steady-state population balance model is developed to account for the propylene polymerization process. The simulation results indicate that the molecular and particle properties of the resulting polymers can be tuned by operating parameters. Major conclusions involve: a) Increasing the hydrogen concentration in the gas barrier can reduce the molar mass of polymers, but has a negligible impact on the particle size distribution of polymers. b) Polymer particles with larger sizes and wider PSD can be produced from catalyst particles with larger initial size. c) Increasing the riser gas velocities within the range of 3 to 10 m/s can significantly increase the particle size of the resulting polymers. However, its effect becomes weak when the gas velocities exceed 10 m/s. The study presented here shows that the multi-zone circulating reactors has a great advantage in regulating the properties of products.

REFERENCES

Choi K.Y., Zhao X., Tang S., 1994. Population balance modeling for a continuous gas phase olefin polymerization reactor. *Journal of Applied Polymer Science*, 53, 1589-1597. https://doi.org/10.1002/app.1994.070531205

Covezzi M., Mei G., 2001. The multizone circulating reactor technology. *Chemical Engineering Science,* 56,13: 4059-4067. https://doi.org/10.1016/S0009-2509(01)00077-X

Fernandes F.A., Lona L.M., 2004, Multizone circulating reactor modeling for gas-phase polymerization. I. Reactor modeling. *Journal of Applied Polymer Science,* 93, 1042-1052. doi: https://doi.org/10.1002/app.20573

Levenspiel O., Kunii D., Fitzgerald T., 1968. The processing of solids of changing size in bubbling fluidized beds. *Powder technology,* 2, 87-9. https://doi.org/10.1016/0032-5910(68)80043-9

Luo Z.H., Su P.L., You, X.Z., Shi D.P., Wu J.C., 2009. Steady-state particle size distribution modeling of polypropylene produced in tubular loop reactors. *Chemical Engineering Journal,* 146, 466-476. https://doi.org/10.1016/j.cej.2008.10.023

Santos J.L., Asua J.M., de la Cal J.C., 2006. Modeling of olefin gas-phase polymerization in a multizone circulating reactor. *Industrial & engineering chemistry research*, 45, 3081-3094. https://doi.org/10.1021/ie0500523

Zacca J. J., Ray W. H., 1993. Modelling of the liquid phase polymerization of olefins in loop reactors. *Chemical Engineering Science*, 48(22): 3743-3765. https://doi.org/10.1016/0009-2509(93)80218-F

CFD-PBM simulation and scale-up of the pilot-scale bioreactor

Hao Chen[1], Xiu-Guang Yi[2], Xi-Bao Zhang[1], Zheng-Hong Luo[1]

[1]Department of Chemical Engineering, School of Chemistry and Chemical Engineering, State Key Laboratory of Metal Matrix Composites, Shanghai Jiao Tong University, Shanghai 200240, P. R. China.
[2]School of chemistry and chemical engineering, Jinggangshan University, Ji'an, Jiangxi 343009, P. R. China
Corresponding author email: luozh@sjtu.edu.cn

ABSTRACT

In this work, a coupled computational fluid dynamics-population balance model (CFD-PBM) method is applied to study the influence of combination mode of impellers, hole diameter and number of gas distributors, and combination structure on the performance of a pilot-scale bioreactor. The study used fermentation broth as a continuous phase and bubbles as dispersed phases to investigate the effect of bubble size distribution on mass transfer. The method of equal mass transfer coefficients was applied to the scale-up design of the reactor.

Keywords: Stirred bioreactor; Numerical simulation; Impeller combination; Distributor structure; Scale up

1. INTRODUCTION

The stirring tanks are widely used in chemical, metallurgy, food and biochemical fields (Demain and Adrio, 2008). The stirred bioreactors have many advantages such as simplicity in operation and adaptability in diversified production. Although a variety of new bioreactors have been introduced, stirred bioreactors still dominate the fermentation industry (Kawase and Moo-Young, 1990). Therefore, the structural design and amplification effect of stirred bioreactors have always been the focus of fermentation engineering. In addition, the mass transfer process of the stirred bioreactors is influenced by geometrical parameters, including gas distributor structure, impeller number, blade structure, distance between the impeller and impeller, etc. The mass transfer coefficient has a crucial relationship with the scale-up of the bioreactor.

In this work, a coupled computational fluid dynamics-population balance model (CFD-PBM) method is applied to study the influence of combination mode of impellers, hole diameter and number of gas distributors, and combination structure on the performance of a pilot-scale bioreactor. The study used fermentation broth as a continuous phase and bubbles as dispersed phases to investigate the effect of bubble size distribution on mass transfer. The results indicate that the gas distribution is greatly affected by the structure of gas distributor and the diameter of impellers. Through comparative analysis of five impeller and gas distributor combinations, the results show that the combination of Rushton turbine (Impeller four in a multi-impeller) and the four-hole ring distributor can improve the dispersion effect of gas hold-up and mixing performance of bioreactors, and reduce the energy consumption of the bioreactors to 7.53 W/L. Finally, a series of stirred bioreactors with volumes of 15 m^3, 45 m^3 and 75 m^3 were designed based on the numerical simulation results of impeller combination and distributor optimization.

2. MATERIALS AND METHODS
2.1. Figures and Tables

Table 1. Comparison of bioreactor scale-up parameters

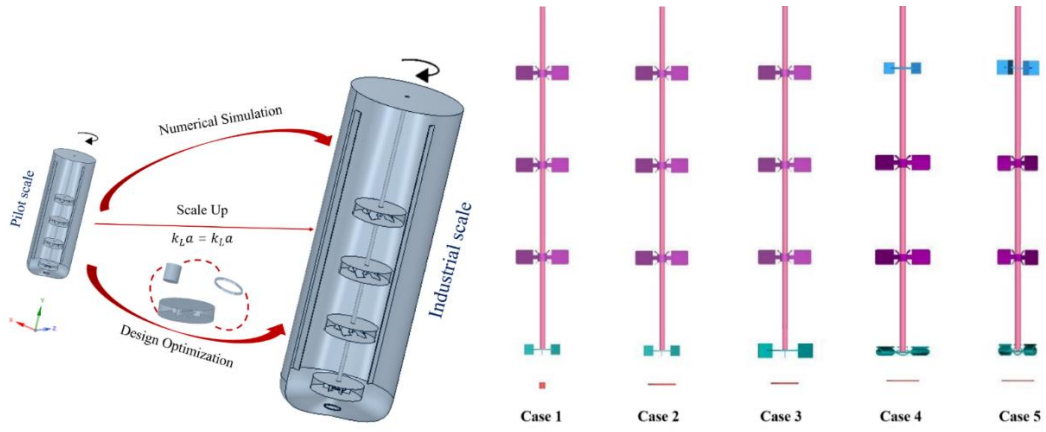| Bioreactor	225 L	15 m^3	45 m^3	75 m^3
Design volume :V	225 L	15 m^3	45 m^3	75 m^3
Working volume V_L	180 L	12 m^3	36 m^3	60 m^3
Magnification factor	1	67	200	334
H/T	2.92	2.92	2.92	2.92
D/D_1	0.31	0.31	0.31	0.31
Ventilation intensity /VVm	0.74	0.42	0.40	0.38
P/V(kW/m^3)	7.53	3.98	2.63	1.58
$k_L a/s^{-1}$	0.00416	0.00416	0.00416	0.00416

Figure 1. *Scaling up methods and Five combinations of agitators in the reactor*

2.2. Equations

2.2.1 Population balance model

The coalescence rate $c(v_i, v_j)$:

$$c(v_i, v_j) = w_{ij} P_c(d_i, d_j) \tag{1}$$

Prince and Blanche coalescence efficiency model formula (Prince and Blanch, 1990):

$$P_c(d_i, d_j) = \exp\left(-\frac{r_{ij}^{5/6}\rho_l^{1/2}\varepsilon^{1/3}}{4\sigma^{0.5}}\ln\frac{h_0}{h_f}\right), r_{ij} = \frac{d_i d_j}{d_i + d_j} \tag{2}$$

Luo and Svendsen's breakup model formula (Luo and Svendsen, 1996):

$$b(V_0, f_v V_0) = \int_{\lambda_{min}}^{\lambda_{max}} P(d_0, f_v^{1/3} d_0, \lambda)\omega(\lambda, d_0)d\lambda \tag{3}$$

2.2.2 Mass transfer coefficient

Commonly used correlation to describe the mass transfer coefficient in stirred bioreactor is the $k_L a$ relationship described:

$$k_L a = k\left(\frac{P}{V}\right)^\alpha v_S^\beta \left(\frac{\eta}{\eta_w}\right)^\gamma \tag{4}$$

3. RESULTS AND DISCUSSION

Stirring impeller and gas distributor are the main factors affecting the inhomogeneity characteristics of the flow field in the bioreactor. **Figure 2** shows that the local gas hold-up and interfacial area of case 2 are higher than that of other cases, and the local Sauter average diameter of case 5 is the highest. Furthermore, the gas hold-up, Sauter average diameter and interfacial area of cases 1-4 in the middle and low regions of bioreactors show two peaks. One reason is that the reactor forms a cycle in this area, increasing the gas residence time. In addition, the impellers diameter of case 1-4 is relatively large, and the gas holding capacity is strong, which is also the reason for the high gas hold-up. In conclusion, the gas hold-up of combination 2 is obviously uniform than other combinations, indicating that optimizing the gas distributor and impeller can improve the gas dispersion performance of the bioreactor.
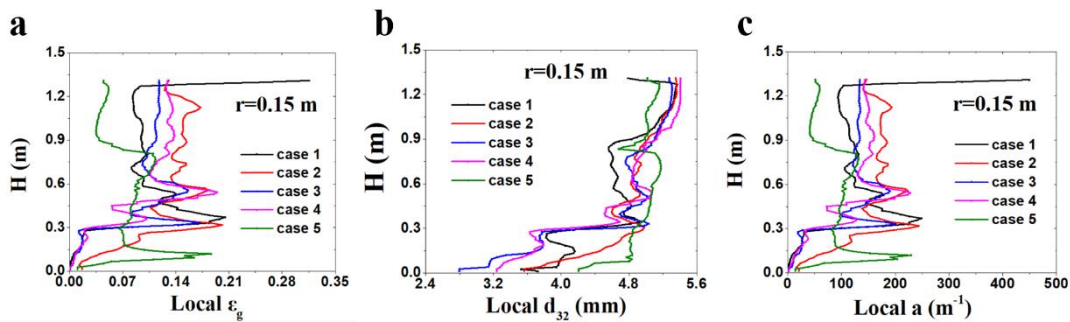

Figure 2. *Effect of different combinations on the axial local (a) gas hold-up (b)*

4. CONCLUSIONS

The results show that the combination of Rushton turbine (Impeller four in a multi-impeller) and the four-hole ring distributor can improve the dispersion effect of gas hold-up and mixing performance of bioreactors, and reduce the energy consumption of the bioreactors to 7.53 W/L. Finally, a series of stirred bioreactors with volumes of 15 m3, 45 m3 and 75 m3 were designed based on the numerical simulation results of impeller combination and distributor optimization.

ACKNOWLEDGEMENTS

REFERENCES

Demain A. L., Adrio J. L., 2008. Contributions of microorganisms to industrial biology. *Mol. Biotechnol.* 38, 41-45.

Kawase Y., Moo-Young M., 1990. Mathematical models for design of bioreactors: Applications of: Kolmogoroff's theory of isotropic turbulence. *Chem. Eng. J.* 43, B19-B41.

Wang T.F., Wang J.F., Jin Y., 2005. Population balance model for gas-liquid flows: Influence of bubble coalescence and breakup models. *Ind. Eng. Chem. Res.* 44, 7540–7549.

Prince M.J., Blanch H.W., 1990. Bubble coalescence and breakup in air-sparged bubble columns. *AIChE J.* 36, 1485-1499.

Luo H., Svendsen H.F., 1996. Theoretical model for drop and bubble breakup in turbulent dispersions. *AIChE J.* 42, 1225-1233.

Stability analysis of continuous crystallizer: Analysis of stationary and oscillatory states

Satish R. Inamdar[1] Sanika Joshi[1], and S.J. Parulekar[2]
[1]*Chemical Engineering Department, Vishwakarma Institute of Technology, Pune 411037, India*
[2]*Chemical and Biological Engineering Department, Illinois Institute of Technology, 127 Perlstein Hall, 10 West 35th Street, Chicago, IL 60616, USA*
Corresponding author email: satishinamdar2810@gmail.com

ABSTRACT

The crystallization process is modeled using population balance models and further transformed into moment equations. The corresponding steady-state model is analyzed based on the sign of eigenvalues to find if motion is stable. Thus, if a steady state is chosen as an operating point, the motion caused should be stable to operate the process unit in the absence of a controller to keep control costs to a minimum. Then the dynamical system can be searched through parameter space for stable solutions using the characteristic polynomial. In this paper, we present two new results on the stability of a continuous crystallizer which is modeled using a population balance model. The first result is the application of the multi-equation bifurcation theory to find branching patterns of stationary states in free parameter space. The second result is about parameter uncertainty in the free parameter space of the moments model that is present as an interval. In the first case, Turning I and Single II branching patterns were obtained from numerical computations, which were not shown in previous work. Further an interval is considered as parameter uncertainty in inlet feed concentration. It was observed that for the secondary nucleation case, where oscillatory states are abundant in free parameter space, the crystallizer remains steady state stable despite the presence of uncertainty. A new result was used that starting with the Kharitonov stability criterion instead of vertex polynomials being Hurwitz stable, a new stability criterion has been applied. The numerical computations illustrate the findings.

Keywords: Population balance model; branching behavior; Kharitonov stability criterion; continuous crystallizer; parameter uncertainty.

1. INTRODUCTION

Crystallization is an important unit operation in chemical engineering and population balance models are used to model the dynamical behavior of a continuous crystallizer. These models have been used to design crystallization processes and their control systems in industrial practice too. The crystal size distribution in the population balance model is used to derive zeroth-order to third-order moments and result in a moment equations model as a system of the ordinary differential equation system. This system now can be analyzed to devise stability measures, which is essential to select a nominal operating point for design and control. The issues that come up are the occurrence of the multiplicity of steady states and the stability of oscillatory states. Lakatos et. al. (2007) have presented results on the multiplicity of steady states and the application of the Mikhailov criterion to study the stability of oscillatory states. In this work, we present two new results, 1. Application of multi-equation bifurcation theory to explore if branching patterns of stationary states form in free parameter space, and 2. Application of Bartlett et. al. (1988) to apply Kharitonov stability criterion without finding Hurwitz stability of all vertex polynomials.

2. CONTINUOUS CRYSTALLIZER MODEL

In this Section, we present the moment equations derived from the population balance model of a continuous crystallizer. We reproduce the moment equations from Lakatos et.al. (2007) for the sake of brevity. The dimensionless moment equations are

$$\frac{dx_0}{d\xi} = -x_0 + \theta_v, v = p, b \tag{1a}$$

where subscripts *p.b* denote primary and secondary nucleation respectively, and

$$\theta_p = x_0 + \mathcal{D}a * y * x_3{}^j \tag{1b}$$

$$\theta_b = -x_0 + \mathcal{D}a * (1 - x_3) * \text{Exp}[-\frac{\sigma}{\text{Log}[\frac{y+\vartheta}{\vartheta}]^2}] \tag{1c}$$

$$\frac{dx_m}{d\xi} = -x_m + y^g(x_{m-1} + \beta x_m); \quad m = 1,2,3 \tag{2}$$

$$\frac{dy}{d\xi} = \frac{y_{in} - y}{1 - x_3} - \frac{(\alpha - y)y^g(x_2 + 3\beta x_3)}{1 - x_3} \tag{3}$$

$$\frac{dy_{sv}}{d\xi} = \frac{y_{sv,in} - y_{sv}}{1 - x_3} + \frac{y_{sv}y^g(x_2 + 3\beta x_3)}{1 - x_3} \tag{4}$$

The initial conditions for these moment equations are given as

$$x_m(0) = x_{m,0}; \quad m = 0,1,2,3; \ y(0) = y_0; \ y_{sv}(0) = y_{sv,0} \tag{5}$$

In the above equations, Eqs. 1-5, x_m is dimensionless m^{th} moment, $m = 0,1,2,3$. The details of this model are given in Lakatos et.al. (2007).

3. RESULTS AND DISCUSSION

Branching behavior of stationary steady states (Karimi and Inamdar, 2002).
Consider a parameter set to find out if a singular parameter point exists for secondary nucleation to occur. We select $\mathcal{D}a = 90.0; y_{in} = 1.2; y_{sv,in} = 8.6; \alpha = 5.; \beta = 0.8; \vartheta = 1.4$. The constants are set as $g = 1; b = 20.0; j = 1.25; n = 2$. The parameter conditions solved for the occurrence of a Turning I branching pattern yield a solution, $y_s = 1.3726, \sigma = 3.7655$. Further, the constants required to compute the perturbed branching solutions are obtained as, $a_{01} = -0.5249$, and $a_{20} = 3.9351$. Now we can compute the perturbed solution as, $w_1 = \pm(0.3652\sqrt{\Delta\mu * \chi})$. The perturbed branch eigenvalue comes out as, $\lambda = \pm(0.2874)$, $\Delta\mu = 0.01$. The sign of the perturbed branch eigenvalue clearly shows that the upper branch of the Turning I pattern is stable, and the lower branch is unstable.
Another branching point that exists in free parameter space, showing the presence of stationary steady states, is Single II branching pattern for the case of secondary nucleation. The constants in the model are set as, $g = 1.5; b = 2.0; j = 1.7; n = 2$. The rest of the parameters are chosen as, $= 190.; y_{in} = 1.4; y_{sv,in} = 7.2; \alpha = 20.5; \vartheta = 1.4$. The Single II point occurs at, $y_s = 2.3961, \sigma = 2.5695, \beta = 1.0663$. We find that $w = -1.1977\Delta\mu^{1/3}\chi$. The perturbed eigenvalue is, $\lambda = -2.5076$, $\Delta\mu > 0$. Therefore, as is required both the branches across singular point are steady state stable.

Stability of oscillatory states in presence of parameter uncertainty (Bartlett et. al., 1988).
Consider a parameter set for secondary nucleation, $\mathcal{D}a = 500.; y_{sv,in} = 8.8; \alpha = 25.; \beta = 0.1; \vartheta = 1.; k_e = 0.8$. Let $y_{in} = 1.2$ initially and shifts to a value $y_{in} = 1.5$. The lower and upper limits of coefficients of characteristic polynomial are obtained from steady state equations. The six convex combinations (Bartlett et. al., 1988) give rise to polynomials whose real and imaginary solutions are mapped with $\lambda \in [0,1]$ and plotted as real versus imaginary parts in a complex plane. Figure 1 shows a complex plane mapping when exponent *b* takes values 2.0, 10.0, 16.0 and initial value of input parameter $y_{in} = 1.2$ is kept constant. The results of computations are plotted in Figure 1, and we see that some of the roots lie in right half plane implying those real parts of eigenvalues are positive. This confirms that the isothermal continuous crystallizer is steady state unstable in presence of parameter uncertainty.
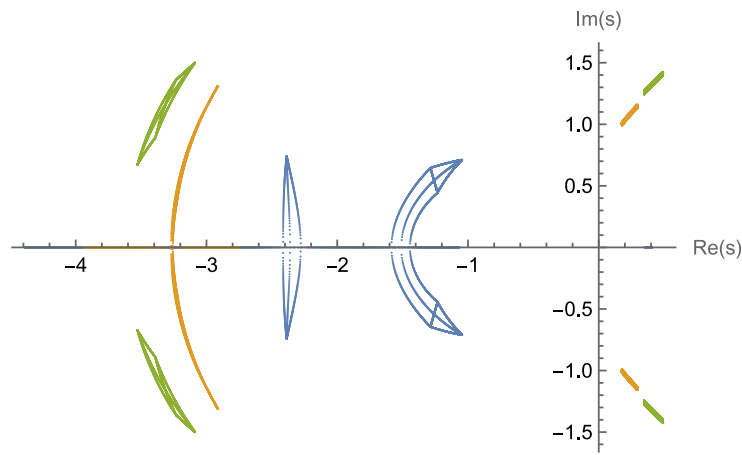
Figure 1. *A comparison between various b values is presented. (b=2 Blue, b=10, Orange, b=16, Green). The three solutions are unstable.*

4. CONCLUSIONS

In this work, we have presented two new results on stability of crystallizer for the first time. The first result is about application of multi-equation bifurcation theory (Karimi and Inamdar, 2002) to study the branching behavior of steady states. The local stability of branches bifurcating from singularity was studied too. The second result is based on a result by Bartlett et.al. (1988), where for Kharitonov stability criterion a new method is applied instead of Hurwitz stability of vertex polynomials. This deals with parameter uncertainty appearing as an interval coefficient. Both the results are presented after numerical computations and illustrate the theory well.

Notation

b	Exponent of secondary nucleation rate
Da	Dimensionless parameter for nucleation
g	Exponent of crystal growth rate
j	Exponent of secondary nucleation rate
k_e	Parameter of primary nucleation rate
n	Population density function, m^{-4}
y	Dimensionless concentration of solute
Greek	
α	Dimensionless parameter
β	Dimensionless parameter
ϑ	Dimensionless equilibrium saturation concentration
Subscripts	
in	Inlet value
sv	Steady state

REFERENCES

Karimi, I.A. and Inamdar, S.R., 2002. Branching and stability of stationary solutions in multi-equation systems. *Chemical engineering science*, **57**(8), 1251-1267. https://doi.org/10.1016/S0009-2509(02)00062-3.

Bartlett, A.C., Hollot, C.V. and Lin H., 1988. Root locations of an entire polytope of polynomials: It suffices to check the edges, *Math. Control Signals Systems*, **1**, 61-71. https://doi.org/10.1007/BF02551236.

Lakatos, B.G., Sapundzhiev, T.J., Garside, J. 2007. Stability and dynamics of isothermal CMSMPR crystallizers, *Chemical engineering science*, **62**, 4348-4364. https://doi.org/10.1016/j.ces.2007.04.028

Population balance equation for collisional breakage: A new numerical solution scheme and its convergence[#]

Prakrati Kushwah[1], Arijit Das[1] , Jitraj Saha[1] and Andreas Bück[2]
[1]Department of Mathematics, National Institute of technology Tiruchirappalli, Tamil Nadu – 620 015, India
[2]Institute of Particle Technology, Friedrich-Alexander Universität Erlangen-Nürnberg, Erlangen - 91058, Germany
Corresponding author email: jitraj@nitt.edu

ABSTRACT

A new numerical method for the solution of population balance equation modeling nonlinear collisional breakage is presented. The new scheme is obtained by modifying the birth term of discretized equation. Allocation of new born particles to their neighboring cells plays a vital role towards the efficiency of proposed model. A detailed investigation on mathematical properties of the scheme, e.g., consistency and stability, is presented for different mesh types. It shown that the new scheme is moment-consistent and has first order convergence rate. A new finite volume scheme for collisional breakage is also presented to validate the efficiency of new scheme over several physics embedded test problems.

Keywords: collisional breakage; sectional methods; consistency; Lipschitz stability; error analysis.

1. INTRODUCTION

Two types of breakage can be discriminated: "Linear" breakage in which a mother object with some property value v splits into a collection of fragments with property values u, *always smaller* than v. The reason for the onset of breakage is not further specified or modeled. This type of breakage well describes the situation where stress is provided by an external entity or field, e.g., thermal stress. The other type is *collisional* breakage: Here, two mother objects with properties v and w collide. The probability of breakage of either object as well as the property distribution of the fragments depend on the properties of the specific collision partners. Both objects may break with different fragment distributions (as in the "linear" case); however, even property transfer may occur, i.e., one of the mother objects may even increase in volume by transfer and attachment of one of the fragments to a mother object. It is therefore a more general situation than the "linear" case with various applications in science and technology. The formal mathematical model reads as [ref. to Kushwah et al. (2023). Commun. Nonlinear Sci. Numer. Simul. 121:107244.]

$$\frac{\partial n(v,t)}{\partial t} = \int_0^\infty \int_v^\infty b(v|\zeta,\eta)\mathcal{K}(\zeta,\eta)n(\zeta,t)n(\eta,t)d\zeta d\eta - \int_0^\infty \mathcal{K}(v,\zeta)n(v,t)n(\zeta,t)dv\zeta,$$

with initial condition $n(x,0) = n_0(x) \geq 0$. The breakage kernel $b(v|\zeta,\eta)$ denotes formation rate of fragments with volume v from particles with volume ζ due to its impact with a particle of volume η. Other components are defined in the usual manner.

In this contribution, an alternative method for the solution of population balance equation of collisional breakage is presented. A detailed analysis of its mathematical properties is also provided. The numerical efficiency of the proposed model is validated over several physics-embedded test problems both qualitatively and quantitatively. Note that we need a reference scheme to validate the numerical efficiency of the new model. Therefore, a finite volume model is also introduced, and efficiency of both the schemes are discussed over the considered test problems.

2. MATERIALS AND METHODS

During collisional breakage, if a new daughter particle (fragment) is formed, there arise two possibilities for particle allocation in a cell according to its volume. Without taking into account the possibilities and handling them separately, inconsistencies in total volume will accumulate over time. The two events are:

1. <u>(Less likely event)</u> If the volume of daughter particle is equal to the volume of cell representative, then all properties associated to it are trivially preserved.
2. <u>(Most likely event)</u> If the particle volume is not equal to the cell representative v_i we assign that particle to the two neighboring cell representatives such that two pre-chosen dynamic properties are preserved exactly. The *birth modification* rule is as follows: If a particle of volume v is formed in volume range $[v_i, v_{i+1}]$, then formation of this particle is represented by assigning a fraction $\mu_i^+(v)$ at v_i and fraction $\mu_{i+1}^-(v)$ at v_{i+1} to particle populations. Similarly, particle formation in volume range $[v_{i-1}, v_i]$, is reallocated in the pivots v_{i-1} and v_i with the help of suitably defined volume fractions $\mu_{i-1}^+(v)$ and $\mu_i^-(v)$. Thus, representative in the $i-$th cell gets two contributions from its two neighboring pivots, namely v_{i-1} and v_{i+1}.

Figure 1 represents particle allocation in the intervals $[v_i, v_{i+1}]$, and $[v_{i-1}, v_i]$ respectively.
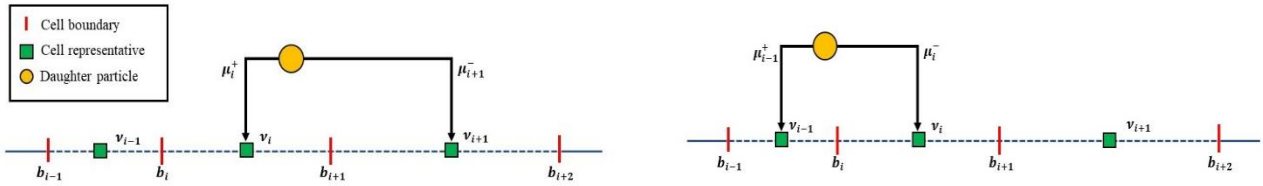

Figure 1. *Pivot allocation when particle volume is not same as cell representative.*

2.2. Equations
The new discrete equation reads like

$$\frac{d\widehat{N}_i}{dt} = \sum_{j=1}^{I}\sum_{k=i}^{I} \omega_{ik}^{j}\mathcal{K}(v_k, v_j)\widehat{N}_k\widehat{N}_j - \sum_{j=1}^{I} \mathcal{K}(v_i, v_j)\widehat{N}_i\widehat{N}_j,$$

where

$$\omega_{ik}^{j} := \int_{v_i}^{v_{i+1}} \mu_i^+(v)b(v|v_k, v_j)dv + \int_{v_{i-1}}^{v_i} \mu_i^-(v)b(v|v_k, v_j)dv .$$

The first and second integrals in the above equations are zero for $i = I$ and $i = 1$, respectively.

3. RESULTS AND DISCUSSION
We have discussed 3 sample problems and validate the efficiency of the new model, along with error analysis in the paper. Here, we will showcase results for one problem which deals with multiple breakage and constant Collision kernel along with mono-disperse initial condition. Fig. 1 shows numerical number density simulated form the new scheme and Fig. 2 compares the particle density and moments with exact quantities and finite volume scheme (reference) results. An excellent agreement of all the vital properties can be observed which proves the robustness of the presented method.
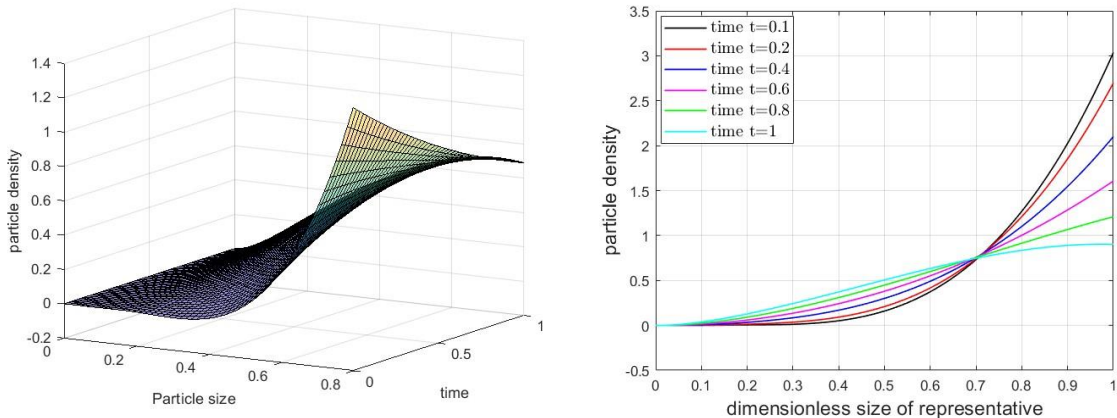
(a) 3D representation of number density   (b) Number density at different times

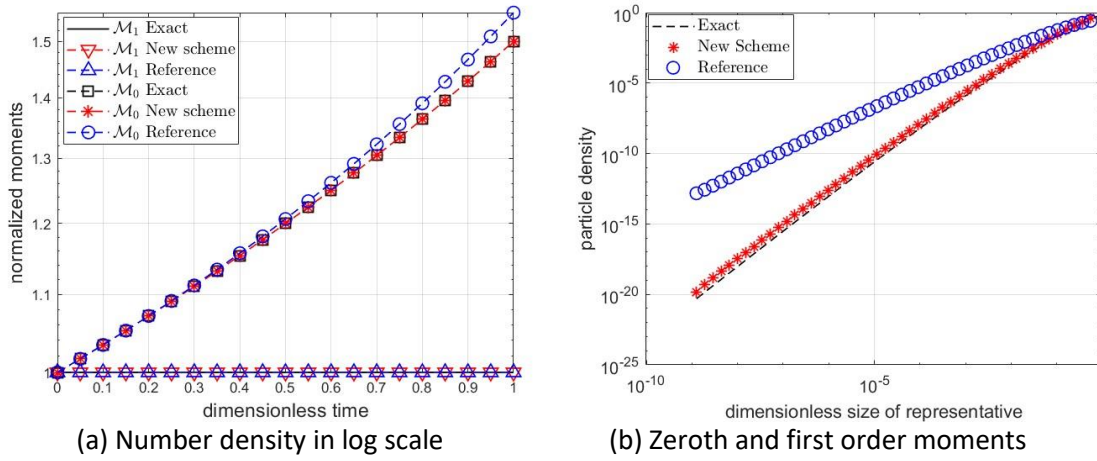**Figure 2.** *Number density with respect to particle size at different times*

33

(a) Number density in log scale   (b) Zeroth and first order moments

Figure 3. *Comparison of number density and different order moments.*

4. CONCLUSIONS

We introduce a new sectional method to approximate the solution of the nonlinear collisional population balance breakage equation. The underlying idea here is to modify the birth term by reallocating the particles in their neighboring pivots such that the total number and volume of the particles are captured with high accuracy. A detailed stability and convergence analysis of the scheme is carried out using Lipschitz condition. Discretization error is calculated for four different meshes to investigate the order of consistency. The first order convergence is obtained from analysis for uniform, nonuniform and locally uniform meshes. However, scheme is inconsistent on random meshes. Several test problems are solved to validate the accuracy of the proposed scheme. For all the considered examples, the qualitative comparison of number density as well as zeroth and first order moments is performed. The relative error for both moments, relative sectional error and relative L^1 −error are calculated for new scheme. Calculation for EOC shows first order of convergence. Overall, new scheme gives highly accurate results both qualitatively and quantitatively.

REFERENCES

Cheng Z., Redner S., 1988. Scaling theory of fragmentation. *Physical Review Letters*. 60:2450. 10.1103/PhysRevLett.60.2450.

Cheng Z., and Redner S., 1990. Kinetics of fragmentation. Journal of Physics A: Mathematical and General. 23:1233. 10.1088/0305-4470/23/7/028.

Ramkrishna D. *Population balances: Theory and applications to particulate systems in engineering*. Academic Press, 2000. 10.1016/B978-0-12-576970-9.X5000-0.

Kumar J., Warnecke G., 2008. Convergence analysis of sectional methods for solving breakage population balance equations-I: The fixed pivot technique. *Numerische Mathematik*. 111:81–108. 10.1007/s00211-008-0174-6.

Kumar J., Saha J., Tsotsas E., 2015. Development and convergence analysis of a finite volume scheme for solving breakage equation. *SIAM Journal on Numerical Analysis*. 53(4):1672–1689. 10.1137/140980247.

Das A., Saha J., 2022. Existence and uniqueness of mass conserving solutions to the coagulation and collision-induced breakage equation. *The Journal of Analysis*. 30(3):1323-1340. 10.1007/s41478-022-00407-z.

Adomian(-Padé) series solutions for the nonlinear hyperbolic aggregation population balance equation: Derivation, analysis, and performance

Prakrati Kushwah[1], Kamalika Roy[2] , Jitraj Saha[1] and Andreas Bück[3]

[1]Department of Mathematics, National Institute of technology Tiruchirappalli, Tamil Nadu – 620 015, India

[2]Department of Mathematics, Sastra Deemed University, Thanjavur, Tamil Nadu - 613 401, India

[3]Institute of Particle Technology, Friedrich-Alexander Universität Erlangen-Nürnberg, Erlangen - 91058, Germany

Corresponding author email: jitraj@nitt.edu

ABSTRACT

We analyze the hyperbolic aggregation population balance model that guarantees mass conservation. New solutions for this model is obtained by employing Adomian decomposition method. A recursive scheme is derived to generate the solution as an infinite series. Mathematical convergence analysis of the new scheme is performed in detail. Further the accuracy and efficiency of the time dependent solutions are accelerated and stabilized for longer times by coupling the analytical method with Padé approximation technique. Reliability of the coupled approach is validated by considering several empirical test problems. For one test problem, we successfully present the new series-solution in closed form. Qualitative and quantitative comparison of significant physical entities like particle size distribution, total mass, number etc. are carried out against their exact values. Furthermore, we present a detailed error analysis of the original solution both with the Adomian and Padé approximant solutions at different times and parameters.

Keywords: aggregation; Adomian decomposition method; Padé approximant; asymptotic stability; convergence.

1. INTRODUCTION

The aggregation PBEs are in general nonlinear equations whose mathematical treatment is very challenging. Solutions are mostly unavailable except for a few class of simple kinetic rates. Therefore, advanced computational techniques are much needed to solve the aggregation PBEs either analytically or numerically. The first aggregation model was proposed by M Smoluchowski in 1916. For a continuous system, the mass-conserving, hyperbolic aggregation equation is an integro-partial differential equation [ref. to Bourgade & Filbet (2008)] as given below

$$\frac{x\partial n(x,t)}{\partial t} = -\frac{\partial}{\partial x}\left[\int_{0}^{x}\int_{x-\omega}^{\infty} v\zeta(v,\omega)n(v,t)n(\omega,t)dvd\omega\right],$$

With initial data

$$n(x,0) = n_0(x) \geq 0, \ for \ all \ x \geq 0.$$

Here, $n(x,t)$ is the particle density of x -size (≥ 0) particles at time $t \geq 0$, and $\frac{\partial}{\partial t}$ denotes the partial derivative with respect to time. The function $\zeta(x,y)$ appearing on the right hand side is known as aggregation kernel. It gives the rate at which x -size and y -size particles merge to form a larger $(x + y)$ -size particle. In general, it is assumed that aggregation kernel is nonnegative and symmetric in nature. Besides the particle number density $n(x,t)$, their moment functions also play a significant role in the population balance modeling. Few of them defines important particle properties. In this note the n −th order general moments are defined as

$$m_i(t) = \int_{0}^{\infty} x^i n(x,t)dx.$$

The zeroth moment $m_0(t)$ defines the total number of particles in the system, and the first moment $m_1(t)$ defines the total particle mass of the system. In case of mass-conservation we must have $\frac{dm_1(t)}{dt} = 0$.

2. MATERIALS AND METHODS

With the onset of high-speed computational techniques several semi-analytical methods are used considerably to solve nonlinear mathematical models when analytical solutions are either unavailable, or too complicated which are unlikely to be found. These techniques are especially helpful in disciplines like engineering and industry where complicated systems or events are described using mathematical models. The *Adomian decomposition method* (ADM) is one of the most efficient semi-analytical techniques for a wide range of nonlinear differential equations. It was first proposed by George Adomian in the 1990s as an alternative to traditional numerical and analytical methodologies. This approach is based on decomposition of a complex nonlinear problem into smaller linear sub-problems, which can be solved analytically. These solutions are then added together using a recursive scheme to approximate the solution of original nonlinear equation. By changing the number of terms in the series, it is possible to influence the precision of solution to a further extent. The fact that ADM does not require the use of meshes or grids, which are generally employed in other numerical methods based on sectional discretization is one of the great advantages of the method. As a result, problems involving complicated geometries or irregular boundaries benefit greatly from the ADM. The aforementioned factors have led to widespread application of this technique in numerous technical and scientific community. Note that for time dependent solutions, asymptotic stability of the solution is utmost important. To this end, the Padé approximant is rational function that gives the best approximation of a given function, whose values are available at specific points. These approximants are constructed by taking a ratio of two power series, one for the function being approximated and another for the function's reciprocal. Coefficients of the power series are chosen in such a way that the error is minimum between the function and Padé approximant. This approximation method is particularly useful in dealing with functions that have singularities, poles or branch cuts and stabilize the solutions for longer times. The analytical properties of such functions are preserved while being correctly approximated. Each analytical method has its strength and limitations. It is found that by coupling the Padé approximant with other analytical methods often results in more accurate solution. In this case, the approximated solution obtained by ADM is be redefined by coupling it with Padé approximant and thus advantages of both the methods can be enjoyed. The major success is observed on the stability of time dependent solutions at larger times. The coupled ADM-Padé solution shows stabilized asymptotic behavior as compared to the regular ADM solution.

To further understand the requirement of coupling these methods for analyzing solutions at larger times, a sample study is presented. In the Figure 1, exact particle density for sum aggregation kernel $\zeta(\nu, \omega) = \nu + \omega$ is compared against the $5-$th order ADM solution and $[2,2]-$order ADM-Padé approximant over an physics-embedded initial conditions. For Figure 1, an exponential initial distribution $n_0(x) = \exp(-x)$. From Figure 1 it is noticed that both ADM and ADM- Padé approximant predict the density function with high accuracy at $t = 1$. However, when time increased to $t = 3$ and $t = 5$, it is noticed that ADM over-predicts the solution and generates huge margin for error. However, ADM- Padé approximat gives more accurate and stabilized solutions results at longer times also.
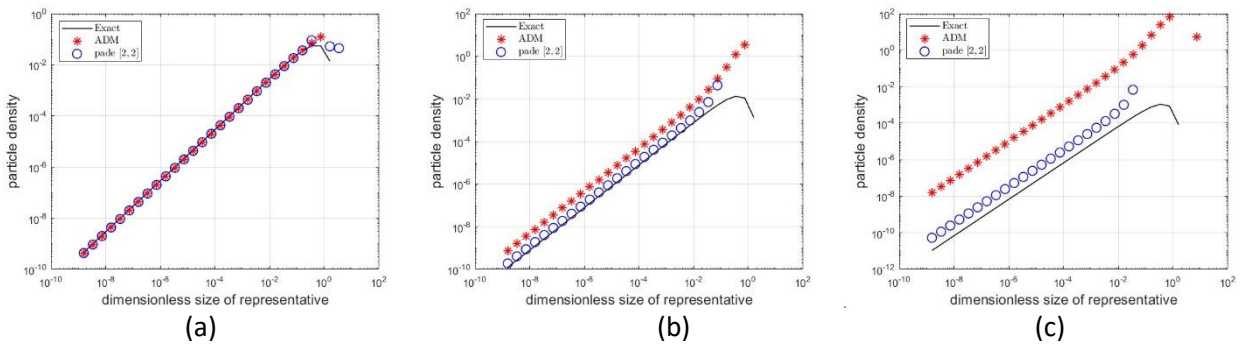

| (a) | (b) | (c) |

Figure 1. *Comparison of the particle density at different times; (a) t = 1, (b) t = 3, and (c) t = 5 for sum aggregation kernel with exponential initial distributions.*

3. RESULTS AND DISCUSSION

We validate the efficiency of the introduced ADM and ADM-Padé methods for solving the hyperbolic aggregation PBE. This is carried out by considering four test cases. These problems are classified into two

categories with respect to initial particle density distributions as: (i) exponential $n_0(x) = \exp(-x)$, and (ii) Gaussian distribution

$$n_0(x) = \frac{(\rho + 1)^{\rho+1} x^\rho \exp(-(\rho + 1)x)}{\Gamma(\rho + 1)},$$

where $\rho = 1$ are considered. For each type of initial data two different aggregation kernels are chosen in increasing difficulty level. The results obtained from ADM-based scheme are compared with exact ones to showcase a great prediction of all the concerned physical quantities. Note that, fifth-order ADM-based solutions are considered throughout the manuscript. The series solutions can be further refined and improved by including higher number terms, however it will increase the computational complexity and thus affect the computational cost and efficiency. Series solutions are further improved by coupling with the Padé approximant of the ADM solutions, which gives a stable and efficient solution for a longer period of time. The quantitative analysis for particle density is carried out for both the methods and it is observed that coupled method gives improved results. In the subsequent presentation, the methodology for calculating the errors will be presented. Here, we present results for the case where exponential initial condition along with constant aggregation kernel is considered.
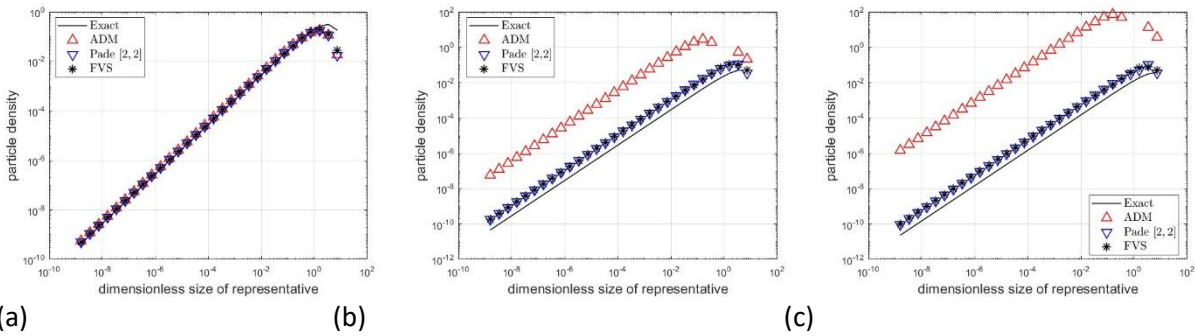

(a)   (b)   (c)

Figure 2. *Comparison of the particle density at different times; (a) $t = 1$, (b) $t = 3$, and (c) $t = 5$*

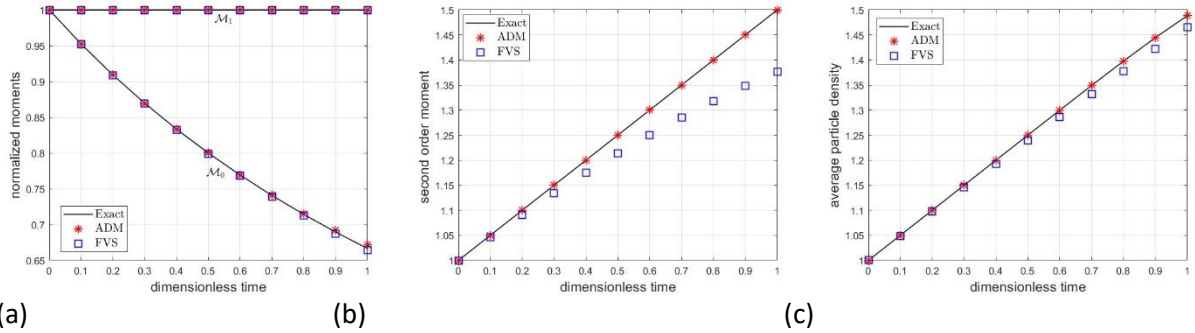(a)   (b)   (c)

Figure 3. *Comparison of (a) zeroth and first order moments (b) Second order moment (c) Average particle size*

From the figures, it can be observed that ADM with Padé gives promising results for number density and is in excellent agreement with exact as well as finite volume scheme (FVS) (Bourgade JP, 2008). All order moments and average particle size is very well captured by ADM as compared to FVS.

4. CONCLUSIONS

The Adomian decomposition approach is implemented for the first time to approximately solve the hyperbolic aggregation population balance equation. A recurrence relation is developed to approximate the solution using the ADM approach. Convergence analysis is carried out based on contraction mapping principle. Several empirical test problems are taken into consideration with various kernel selections in order to validate the series solution. Both a qualitative and quantitative comparison of the exact and approximated quantities is performed. It is proved that the ADM accurately predicts all of the key characteristics with just a few terms in the series solution. From the description above, it can be inferred that ADM can serve as one of the most effective semi-analytical methods for the solution of hyperbolic aggregation model. Moreover, to improve the accuracy and to stabilize the asymptotic behavior of the solution, ADM is coupled with Padé approximation method. This technique produced highly accurate results with accelerated rate of convergence for longer times.

REFERENCES

Adomian G., 1990. A review of the decomposition method and some recent results for nonlinear equations. *Mathematical and Computer Modelling*, 13(7):17–43. 10.1016/0895-7177(90)90125-7.

Bourgade JP., Filbet F., 2008. Convergence of a finite volume scheme for coagulation-fragmentation equations. Mathematics of Computation, 77:851–882. https://www.ams.org/journals/mcom/2008-77-262/S0025-5718-07-02054-6/

Singh R., Saha J., and Kumar J., 2015. Adomian decomposition method for solving fragmentation and aggregation population balance equations. *Journal of Applied Mathematics and Computing*, 48:265–292. 10.1007/s12190-014-0802-5

Das A., and Saha J., 2023. On the mass conserving solutions to the singular kernel coagulation with multi-fragmentation. *Japan Journal of Industrial and Applied Mathematics*, 40(1):563–588. Doi: 10.1007/s13160-022-00544-9.

Ramkrishna D. *Population balances: Theory and applications to particulate systems in engineering*. Academic Press, 2000. 10.1016/B978-0-12-576970-9.X5000-0.

A bubble coalescence model for the population balance equation in gas–solid fluidized bed

Wen Zhao-Quan [1,2], Zhang Xi-Bao[1] and Luo Zheng-Hong[1]

[1] Department of Chemical Engineering, School of Chemistry and Chemical Engineering, State Key Laboratory of Metal Matrix Composites, Shanghai Jiao Tong University, Shanghai 200240, P. R. China.
[2] Department of Chemical Engineering, School of Environmental and Chemical Engineering, Jiangsu Ocean University, Jiangsu, Lianyungang 222005, P. R. China.
Corresponding author email: majorwen@alumni.sjtu.edu.cn, wenzq@jou.edu.cn

ABSTRACT
A new bubble coalescence model was developed to simulate the bubble size distribution in gas-solid bubbling fluidized bed. The model takes into account the collisions that occur due to the differences in the rising velocities of the bubbles and the entrainment of the bubbles by the wake. The efficiency of coalescence for colliding bubbles is developed analogously to the liquid film drainage process in a gas-liquid system. Additionally, the model considers the physical phenomena and closes the coalescence model by performing sensitivity analysis on the unspecified parameters. The model is coupled with the population balance equations (PBEs) to predict the distribution of bubble sizes in the fluidized bed. The results of the model predict the trends of bubble size distribution reasonably well and show good agreement with the experimental data.

Keywords: gas-solid bubbling fluidized bed; population balance model; bubble coalescence; size distribution; coalescence efficiency

1. INTRODUCTION
Recent years have seen numerous experimental measurements of bubble size distribution in bubbling fluidized beds using advanced techniques. Karimipour et al. provided correlations between bubble diameters and rise velocities. However, models predicting bubble size distribution in gas-solid fluidized beds, considering bubble coalescence and breakage, remain scarce. This paper aims to develop a bubble coalescence model based on physical motion phenomena. Informed by the well-established theoretical basis for bubble coalescence in gas-liquid systems, we adapt these principles to model bubble coalescence in gas-solid bubbling fluidized beds, providing key contributions to the understanding of bubble coalescence in such systems.

2. METHODS
2.1. Collision frequency
Hu and Liu believed that the coalescence is caused by two mechanisms: difference of bubble rising velocities and bubble wake effect. The rising velocities of bubbles with diameter of d_i are calculated by the correlation of Davidson and Harrison:

$$u_i = 0.711\sqrt{gd_i} + U_g - U_{mf} \tag{1}$$

Eq.(1) suggests that the rising velocities of bubbles become larger with the increase of bubble size. It can conclude that bubble collision will not occur when the size of leading bubbles is larger than that of following bubbles. The situation on a case-by-case basis is investigated in this work. The diameters of leading bubbles (i) and following bubbles (j and k) satisfy the relationship of $d_j < d_i < d_k$, and the collision between leading bubbles and following bubbles are illustrated in Fig.1.

First, the diameter of the collision tube is the sum of diameters of two colliding bubbles as the diameter of leading bubbles is smaller than that of the following bubbles ($d_i < d_k$). The dark-colored solid line cylindrical area in Fig.1 is the collision tube due to the difference of bubble rising velocity. the collision frequency due to different rising velocities can be given by computed by:

$$\omega_r(d_i, d_k) = \frac{\pi}{4}(d_i + d_k)^2(u_k - u_i) = \frac{\pi}{4}(d_i + d_k)^2\left(0.711\sqrt{gd_k} - 0.711\sqrt{gd_i}\right) \tag{2}$$

Second, for the case of that the diameter of leading bubbles is larger than that of the following bubbles ($d_j < d_i$), many researchers believed that the coalescence of bubbles would occur due to the local low-pressure area formed by the wake of leading bubbles, which caused an attractive effect on the following bubbles. As the speed of leading bubbles is larger than that of the following bubbles, the bubble collision can only result from the low-pressure area formed by the trailing wake. Therefore, some researchers pointed out that bubble coalescence could only take part in the condition where the following bubbles were in the wake region of leading bubbles. The light-colored dashed line cylindrical area in Fig.1 is the collision tube formed by the bubble wake effect. According to the Clift's model, the wake angle θ_w can be expressed as

$$\theta_w = 50 + 190\exp\left(-0.62Re_i^{0.4}\right) \tag{3}$$

In discussing the above two collision mechanisms, three subscripts appear, and to further simplify the model, the collision frequency model for bubbles in a gas-solid fluidized bed can be written as

$$\omega(d_i, d_j) = \begin{cases} \frac{\pi}{4}(d_i + d_j)^2 \left(0.711\sqrt{gd_j} - 0.711\sqrt{gd_i}\right) & d_i < d_j \\ \frac{\pi}{4}(d_i + d_j)^2 \sin^2\theta_w \left[(u_{ri}^2 + u_{\theta i}^2)^{\frac{1}{2}} - 0.711\sqrt{gd_j}\right] & d_i \geq d_j \end{cases} \tag{4}$$
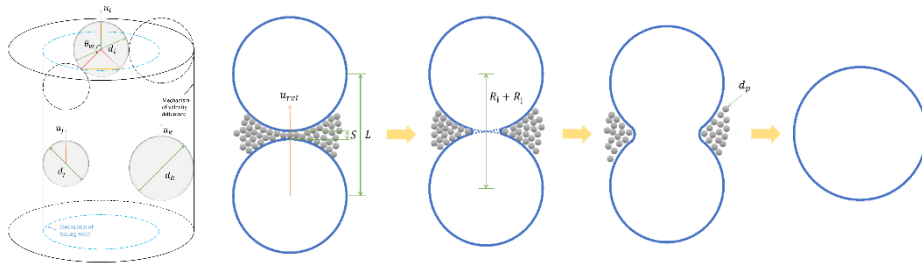

Figure 1. *Collision tube schematic: two different collision mechanisms (left); Schematic diagram of bubble coalescence process in fluidized bed (right)*

2.2. Coalescence efficiency

The most common model for coalescence efficiency in gas-liquid systems is based on the film drainage model. We believe that bubbles in gas-solid systems also have similar behavior to that in gas-liquid systems. As shown in Fig.1, the process of bubble coalescence in a gas-solid fluidized bed is demonstrated. Thus, the bubble coalescence mechanism is a three-step process:

(1) Two bubbles collide, trapping a very thin layer of solid particles between them;(2) Bubbles keep in contact till the solid particle layer becomes thinner. The time that two bubbles keep in contact can be expressed using t_e;(3) Rupture of the solid particle layer when the thickness is smaller than the size of solid particles, and then two bubbles coalesce. The coalescence time required from the collision to the occurrence of coalescence is denoted as t_c.

From the process described above, it can be seen that when t_e is greater than t_c, the bubbles can coalesce. Thus, the probability density function of the normal distribution can be applied to calculate the coalescence efficiency using Coulaloglou's research results. And the contact time t_e is a random variable having negative exponential distribution with mean $\bar{t}_e$, then the coalescence efficiency in a gas-solid fluidized bed can be expressed as]

$$P(d_i, d_j) = P(t_e \geq t_c) = \exp\left(-\frac{t_c}{\bar{t}_e}\right) \tag{5}$$

The two characteristic times in Eq. (5) need to be determined. In Fig.1, when two bubbles collide, the thickness of the layer of solid particles trapped between the bubbles is s. Glicksman and Lord et al. believe that the coalescence time for two equal-size bubbles at a spacing s can be given as

$$\frac{1}{u_{rel}t_c} = \frac{4}{\frac{d_B}{2}\left[\left(\frac{2s}{d_B} - 1\right)^4 - 1\right]} \tag{6}$$

On the basis of this model, we use the equivalent diameters of the two bubbles to modify the Eq. (6). Therefore, the coalescence time for bubble sizes d_i and d_j can be expressed as

$$t_c = \frac{\frac{d_e}{2}\left[\left(\frac{2s}{d_e} - 1\right)^4 - 1\right]}{4u_{rel}} \tag{7}$$

where $d_e = 2d_i d_j/(d_i + d_j)$, $u_{rel} = \begin{cases} u_j - u_i & d_i < d_j \\ u_j - u_{wi} & d_i \geq d_j \end{cases}$ .Here we also discussed the contact time for two bubbles in two cases.

Case 1: Mechanism of bubble rising velocity difference. The contact time $\bar{t}_e$ due to the bubble rising velocity difference can be given as

$$\bar{t}_e = s/u_{rel}, u_{rel} = u_j - u_i \tag{8}$$

Case 2: Mechanism of trailing wake. Based on the geometric relationship, the modified distance s^* can be expressed as

$$s^* = s + \frac{d_i}{2}\left[1 - \cos(180 - \frac{\theta_w}{2})\right] = s + \frac{d_i}{2}\left[1 + \cos(\frac{\theta_w}{2})\right] \tag{9}$$

So, the contact time $\bar{t}_e$ due to the trailing wake can be given as

$$\bar{t}_e = s^*/u_{rel}, u_{rel} = u_j - u_{wi} \tag{10}$$

3. RESULTS AND DISCUSSION

To verify the bubble coalescence model developed in this paper, the population balance equation is solved based on the experimental data of Busciglio et al., In their experiments, the dimensions of the gas–solid fluidized bed equal to 800 (height) × 180 (width) × 15 (depth) mm.The results in Fig.2 show the bubble size distributions at the height of $0.5H_0$, $0.75H_0$ and $1.0H_0$ in the fluidized bed for a gas velocity of $3.4U_{mf}$. Meanwhile, the results in Fig.3 show the bubble size distributions at the height of $0.5H_0$, $0.75H_0$ and $1.0H_0$ in the fluidized bed for a gas velocity of $5.0U_{mf}$. In summary, the model predictions are in fairly good agreement with the experimental results. The peaks of the bubble size distribution functions and their locations are reasonably well matched.
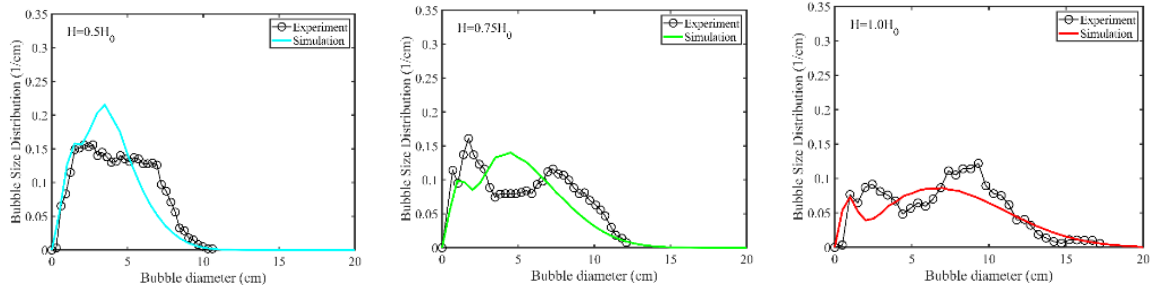

Figure 2. Comparison of experimental and simulated bubble size distribution ($U_g = 3.4U_{mf}$)
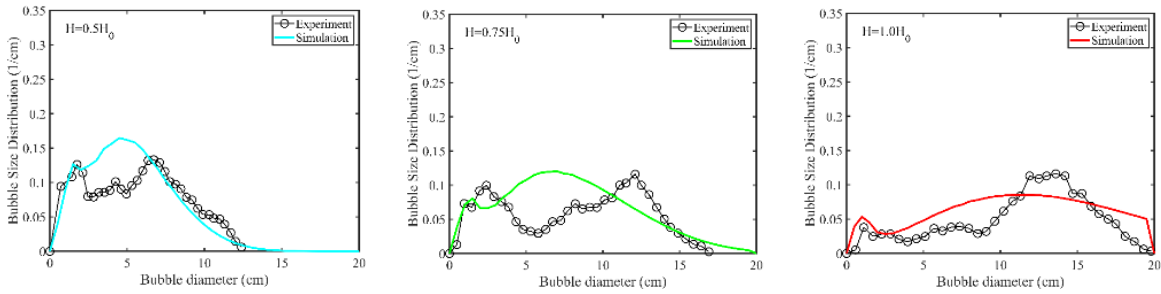

Figure 3. Comparison of experimental and simulated bubble size distribution ($U_g = 5.0U_{mf}$)

4. CONCLUSIONS

The main theme of this work is to accurately predict the bubble coalescence in gas-solid bubbling fluidized beds, and a new coalescence model based on the characteristics of the physical processes of bubble coalescence is developed. The approach of this work has two advantages. Firstly, two collision mechanisms are considered: (1) the bubble coalescence caused by the difference of bubble rising velocities, and (2) the coalescence due to the trailing wake. Secondly, the film drainage phenomenon of bubble coalescence in gas-liquid systems adopted for developing the coalescence efficiency model in gas-solid fluidized beds. The evolution of bubble size distribution obtained by the model calculation is in general agreement with the experiment. This model provides a theoretical basis for solving the problem of understanding the evolution of bubble size in gas-solid fluidized beds.

ACKNOWLEDGEMENTS

REFERENCES

Karimipour S., Pugsley T.,2011. A critical evaluation of literature correlations for predicting bubble size and velocity in gas–solid fluidized beds, Powder Technology. 10.1016/j.powtec.2010.09.016.

A. Busciglio, G. Vella, G. Micale, L. Rizzuti. Analysis of the bubbling behaviour of 2D gas solid fluidized beds: Part I&Part II, Chemical Engineering Journal. 10.1016/j.cej.2007.11.015; https://doi.org/10.1016/j.cej.2008.11.010

Hu S., Liu X.,2020. CFD-PBM simulation of gas–solid bubbling flow with structure-dependent drag coefficients, Chemical Engineering Journal. 10.1016/j.cej.2020.127503.

L.R. Glicksman, W.K. Lord, M. Sakagami.,1987 Bubble properties in large-particle fluidized beds, Chemical Engineering Science. 10.1016/0009-2509(87)80010-6.

Wen ZQ.,Zhang XB.,Luo ZH.,2022.Development of a coalescence model in gas–solid fluidized bed for the population balance equation, Chemical Engineering Journal.10.1016/j.cej.2022.135904

Dynamic modeling and optimal design space determination of pharmaceutical crystallization processes: releasing the synergy between laboratory and industrial scale data

Álmos Orosz[1], Emőke Szilágyi [2], András Spaits[2], Ákos Borsos[2], Ferenc Farkas[2], Imre Markovits[2], László Százdi[2], Balázs Volk[2], Katalin Kátainé Fadgyas[2], Botond Szilágyi[1]

[1]Department of Chemical and Environmental Process Engineering, Budapest University of Technology and Economics, Műegyetem rkp. 3., H-1111 Budapest, Hungary
[2]Egis Pharmaceuticals Plc, P.O. Box 100, H-1475 Budapest 10, Hungary
Corresponding author email: szilagyi.botond@vbk.bme.hu

ABSTRACT

Well-designed crystallization processes can enhance the products' quality; however, this remains a challenging engineering task. Model-based design (e.g., population balance models (PBMs) or computational fluid dynamics (CFD)) can foster the chemical industry's general goal of improving production efficiency. Although these modeling approaches heavily rely on programming skills, a sufficient number of informative experiments are also required. In the past decades, crystallization has been applied generally, which results in large amounts of valuable data deriving from process development and production in lab and plant scale-equally. In this work, we aim to demonstrate that historical-data-based modeling can be feasible, and with its help, production can be improved through offline model-based optimization. The model was used to determine an optimal design space for a temperature cycling operation. The optimal operation halved the current batch time at the plant scale. The optimized temperature profile was validated on a laboratory scale for two particle size specifications.

Keywords: pharmaceutical crystallization; scale-up; population balance modeling; design space; robust optimization

1. INTRODUCTION

Crystallization is a widespread separation and purification technique in the chemical industries, which offers the advantage that the product particle properties can be tuned within a specific domain. This is exploited heavily in pharmaceutical crystallization, where the particle properties are often considered critical quality attributes (CQAs). Population balance models (PBMs) have been deployed in numerous fields of chemical engineering. An adequate model can mimic crystallization dynamics and be utilized for diverse engineering applications. A limitation of model-based technology transfer is that the local conditions (supersaturation, temperature, mixing, etc.) may strongly impact the microscopic and macroscopic behaviour. An elegant and precise solution for simulating processes on different scales is offered by combining PBMs with CFD. However, the computational burden of such full-scale simulations may be prohibitive despite the recent advances in information technology. If the system may be considered well-mixed and is only moderately sensitive to the local stirring conditions, utilizing semi-mechanistic mixing-dependent rate equations may lead to a reasonable solution (Evans et al., 1974).

This work first presents the development of a crystallization model suitable to describe the laboratory and manufacturing scale operation simultaneously involving a limited number of laboratory experiments and historical data of manufacturing batches. Secondly, the design space (DS) (Elder & Teasdale, 2017) is determined using robust multiobjective optimization for laboratory and plant scale operation that satisfies the product particle size constraints with minimal batch time and heating/cooling energy demand.

2. MATERIALS AND METHODS

Compound A is crystallized in an unseeded, cooling crystallization process with temperature cycling (T-cycling). The plant-scale data (16 manufacturing batches) came from the production site, and the initial

conditions (solute and solvent weight), the temperature profile, and the corresponding product particle size quantiles (PSQs) of each batch's CSD were provided. Two dedicated and four historically available laboratory experiments, a seeded and five unseeded. Unlike the plant-scale experiments, the laboratory-scale experiments were monitored with FBRM (see Figure 1 for a high-level summary). The data from the two significantly different manufacturing scales were utilized simultaneously for the kinetic parameter identification. One may wonder whether developing separate models for the two scales would be better for the specific accuracies. The answer is that the available data may not permit us to do so, as complementary information comes from the two measurement groups, i.e., the CQA is the manufacturing-scale PSD. In contrast, the lab experiments were significantly more information-rich, given the existence of FBRM monitoring and intermediate PSD samples.
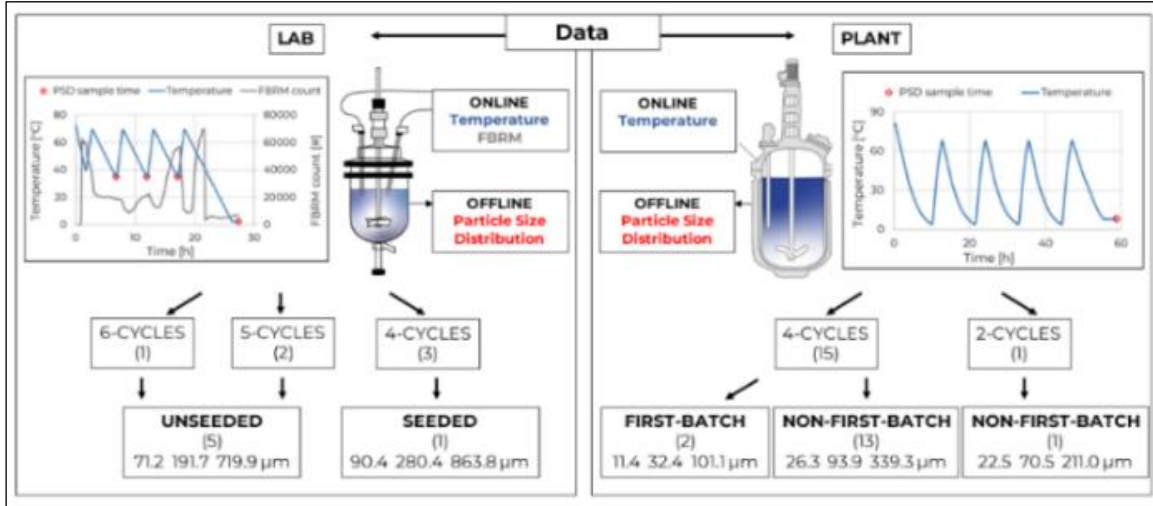

Figure 1. *Representation of the input experiments. The lab and plant-scale experiments and the different cases with the corresponding PSQs of the resulting crystals are illustrated.*

A monovariate number density function $n(L, t)$ is introduced to characterize the particle population. Perfect mixing, constant working volume, negligible breakage, and agglomeration are assumed. The population balance equations (PBEs) for supersaturated and undersaturated conditions take the form of Eq. (1) and Eq. (2). The corresponding initial and boundary conditions and units of the employed variables are listed in the supplementary information (SI: Eq. (1)-(2)).

$$\frac{\partial n(L,t)}{\partial t} + \frac{\partial [Gn(L,t)]}{\partial L} = (B_p + B_s)\, \delta(L - L_n), \qquad \text{if } \sigma > 0 \tag{1}$$

$$\frac{\partial n(L,t)}{\partial t} - \frac{\partial [Dn(L,t)]}{\partial L} = 0, \qquad \text{if } \sigma < 0 \tag{2}$$

The material balance equations (SI: Eq. (3)-(5)) kinetic equations of size-dependent growth, size-dependent dissolution, and primary nucleation (SI: Eq. (7)-(10)) are in the supplementary information for the sake of conciseness. The secondary nucleation equation (Evans et al., 1974) is presented in Eq. (3) since this made it possible to handle the two scales simultaneously by incorporating the agitator properties.

$$B_s = k_s\, \sigma^s \left(\frac{N_P N^3 d^5}{V}\right) \mu_3 \tag{3}$$

A semi-discrete High-Resolution Finite Volume Method implementation reduced the PBEs to ODEs. Then, the ODE was solved numerically with a high-order Runge-Kutta method in Matlab R2022b. The parameter identification is solved by minimizing a bi-objective goal function that, on the one hand, considers the deviations between the measured and simulated particle size quantiles and, on the other hand, the deviations between the measured and simulated nucleation observation times (SI: Eq. (11)-(16)). The optimization problem was solved in Matlab R2022a employing the (Covariance Matrix Adaptation Evolution Strategy) (Hansen, 2016) algorithm.
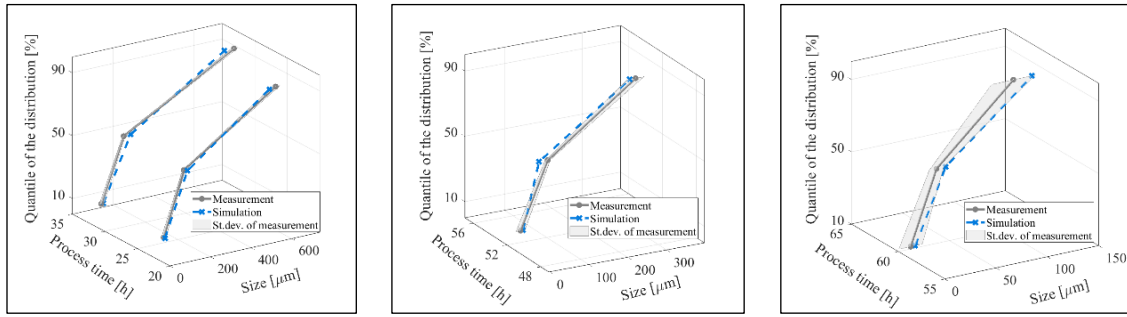
Figure 2. *Validation performance (left to right): lab-scale, plant-scale non-first batch, plant-scale first batch.*

3. RESULTS AND DISCUSSION

A visual representation of the model's predictive power can be seen in Figure 2., where the fitted PSQ values of the validation experiments (and their standard deviation) are portrayed along the corresponding measurement values. The optimized kinetic parameters and the corresponding confidence intervals are summarized in Table 2. of the SI. The figures show that the simulated results agree with the validation data.

With the fine-tuned model, robust multiobjective optimization of the temperature profile was executed by determining design space. The primary objective was reducing the batch time, whereas the secondary objective was reducing the thermal energy demand by minimizing the T-cycles' depth. The temperature turning points were considered normally distributed random variables, and Monte Carlo sampling selected random values, which generated many random temperature profiles around a nominal profile. The design space was determined for cases with different numbers of T-cycles. All the random profiles must satisfy the product size constraints in the final solution. Figure 3. summarizes the results of the cases with four T-cycles. More details are provided in the supplementary information (SI: Eq. (17)-(20); Figure 1., Table 1.).
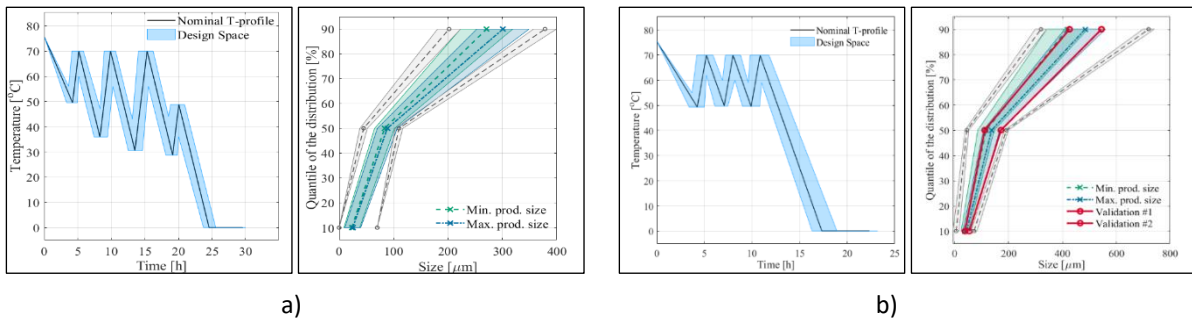

a)   b)

Figure 3. *Temperature profile DS and corresponding PSQs for plant-scale (a) and lab-scale (b) are shown. Blue bands represent the resulting DS; gray bands indicate minimal and maximal PSQ requirements with measurement uncertainties; green and blue bands display simulated PSQs with their variance, and red lines depict lab-scale validation experiments' PSQs.*

As shown in Figure 2, the validation experiments (Fig. 3.b) back up the predictions made with the optimization algorithm, and these results suggest that the model-based optimization provides reliable information. The optimized temperature profile for the plant scale (Fig. 3.a) turned out to be two times faster than the currently applied in the production.

4. CONCLUSIONS

This article presented the PBM-based optimal design space determination for an industrial crystallization process. The input measurements for model development were primarily historical data from previous manufacturing batches and process development works. Due to the features of the available data, namely, the CQA is the plant's product size distribution. Still, as significant kinetic information comes from the lab experiments, the two equipment scales had to be handled by one kinetic model. Evans' secondary nucleation equation was used to reach this goal, which accounts for the different mixing conditions. The kinetic parameter estimation resulted in a good-fitting model with narrow kinetic parameter confidence intervals. The validated model was used subsequently to determine an optimal design space for the temperature

profile that minimized the batch time and energy demand while respecting the technical and quality-related constraints. Lab-scale calculations were experimentally validated for two different particle size specifications. Plant-scale optimal design space suggests that the current operation could be halved in time.

ACKNOWLEDGEMENTS

REFERENCES

Elder, D., & Teasdale, A. (2017). ICH Q9 Quality Risk Management. In *ICH Quality Guidelines* (pp. 579–610). John Wiley & Sons, Ltd.

Evans, T. W., Margolis, G., & Sarofim, A. F. (1974). Mechanisms of Secondary Nucleation in Agitated Crystallizers. In *AlChE Journal* (Vol. 20, Issue 5).

Hansen, N. (2016). *The CMA Evolution Strategy: A Tutorial*. http://arxiv.org/abs/1604.00772

Two-dimensional population balance model for substrate-dependent fungal pellet growth and abrasion

Charlotte Deffur[1], Fangxing Zhang[1] and Heiko Briesen[1]
[1]Chair of Process Systems Engineering, Technical University of Munich, Munich, Germany
Corresponding author email: heiko.briesen@tum.de

ABSTRACT

This study investigates the growth dynamics of *Aspergillus niger* pellets in submerged cultivation. We apply a two-dimensional population balance model to simulate pellet growth, dispersed mycelia formation, glucose consumption, and the influence of shear stress during cultivation. Our results show that increased shear stress and a larger dispersed volume lead to faster glucose consumption, which is consistent with experimental observations. This work improves the understanding of the cultivation processes of *A. niger* and their possible improvement.

Keywords: bi-variate population balance model; *Aspergillus niger*; morphology development; pellet growth; shear stress

1. INTRODUCTION

The filamentous fungus *Aspergillus niger* is widely used as a multipurpose cell factory for the production and secretion of proteins, organic acids, and secondary metabolites. Cellular morphology and hyphal growth affect the choice of process conditions and final product titers. In submerged cultivation, mycelia can grow as dispersed mycelia or in compact pellets. Coagulative pellet formation that occurs in *A. niger* cultivations begins with spore agglomeration, followed by spore germination and pellet growth. In large dense pellets, substrate limitations occur in the pellet core due to hindered diffusion and substrate consumption by the outer hyphae. Variation in nutrient and oxygen supply and pellet fragmentation due to shear stress causes pellet heterogeneity at the bioreactor level [1].

Various modeling approaches have been proposed to understand different aspects of fungal cultivations. Some focus on the initial stages of cultivation and the process of spore agglomeration. Others describe the growth of individual pellets using a stochastic structure model or continuum transport equations. Models for predicting biomass concentration, substrate uptake, and product formation of the entire fungal cultivation often idealize pellets as spherical, porous particles with constant radial density. Reaction kinetics are typically averaged over the entire pellet population [1].

A novel experimental method using synchrotron radiation-based microcomputed tomography has been developed to investigate the 3D structures of a large number of fungal pellets and thus the distribution of hyphal density in the pellet populations [2]. These findings can be further coupled with work investigating the oxygen concentration in various pellets using the microelectrode technique. Thereby, the distribution of hyphal density can be related to the oxygen supply and the metabolism of fungal cells.

In the present study, we aim to simulate the growth of a fungal pellet population with a two-dimensional population balance model. Our model includes pellet growth, dispersed mycelium formation, glucose consumption, and the effect of shear stress potentially causing abrasion.
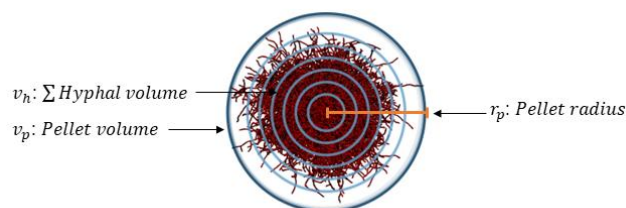
2. MATERIALS AND METHODS

Figure 4: Fungal pellet description in the PBM

2.1. Pellet description and growth processes

Pellets are characterized by the volume of a minimal sphere, which encloses all hyphal elements, v_p in µm³, and additionally with the total volume of all hyphal elements in the pellet, v_h in µm³ (Figure 1). The change of the pellet radius $r_P(v_p)$ due to biological growth processes, $\frac{dr_G}{dt}$, is described by Michaelis-Menten kinetics, where c_g in g·L⁻¹ is the glucose concentration in the cultivation medium and $K_{X,g}$ is the Michaelis constant. For the increase of the total hyphal volume, the outer shell sufficiently supplied with oxygen is determined, described with the limit $r_{o_2 lim}$ and an exponential growth is assumed for the local hyphal volume in the shell. A sigmoid function is used to describe the local hyphal volume $c_h(v_h, v_p, r)$ in a single pellet, based on observations from the 3D structure measurements. The reduction in pellet radius due to shear stress, $\frac{dr_A}{dt}$, occurs for pellets larger than λ with the constant shear impact factor η_{SIF} and the constant shear impact rate $\dot{\gamma}_{SIR}$. In low shear cultivation, it is assumed that no abrasion occurs and equation 2e is zero. Abraded hyphal volume increases the volume of dispersed mycelia, v_d in µm³, which describes the entire dispersed mycelia volume in cultivation. Growth and glucose consumption take place for pellets and dispersed mycelia with the same growth rate μ, yield coefficient Y_{xg}, and hyphal density ϱ. The liquid volume of the cultivation medium is V_{liq}. As liquid volume is considered to be constant all values all states describe absolute instead of volume density values (i.e. number of pellets instead of volumetric number density of pellets). The evolution of the number density distribution, $n_p(v_h, v_p)$ is shown in 2a.

$$\frac{\partial n_p(v_h,v_p,t)}{\partial t} + \frac{\partial [G_h(v_h,v_p)n_p(v_h,v_p,t)]}{\partial v_h} + \frac{\partial [G_p(v_p)n_p(v_h,v_p,t)]}{\partial v_p} - \frac{\partial [A_h(v_h,v_p)n_p(v_h,v_p,t)]}{\partial v_h} - \frac{\partial [A_p(v_h,v_p)n_p(v_h,v_p,t)]}{\partial v_p} = 0 \quad (2a)$$

$$\frac{dr_G}{dt} = k \cdot \frac{c_g}{K_{X,g}+c_g} \quad (2b)$$

$$G_p = \sqrt[3]{4\pi \left(3v_p\right)^2} \cdot \frac{dr_G}{dt} \quad (2c)$$

$$G_h = \int_{r_{o_2 lim}}^{r_P(v_t)} \mu \cdot \frac{c_g}{K_{X,g}+c_g} \cdot c_h\left(v_h, v_p, r\right) \cdot \frac{4}{\pi} r^2 dr \quad (2d)$$

$$\frac{dr_A}{dt} = \eta_{SIF} \cdot \dot{\gamma}_{SIR} \cdot (r_p(v_p) - \lambda)^n \text{ for } r_p \geq \lambda \quad (2e)$$

$$A_p = \sqrt[3]{4\pi \left(3v_p\right)^2} \cdot \frac{dr_A}{dt} \quad (2f)$$

$$A_h = \int_{r_{A(t)}}^{r_P(p)} c_h\left(v_h, v_p, r\right) dr \quad (2g)$$

$$\frac{\partial v_d}{\partial t} = \int_0^\infty \int_0^\infty v_h \cdot \frac{\partial [A_h(v_h,v_p)n_p(v_h,v_p,t)]}{\partial v_h} dv_h dv_p + \mu \cdot \frac{c_g}{K_{X,g}+c_g} \cdot \varrho \cdot v_d \quad (2h)$$

$$\frac{\partial c_g}{\partial t} = \int_0^\infty \int_0^\infty -Y_{xg}^{-1} \cdot \varrho \cdot v_h \cdot \frac{\partial [G_h(v_h,v_p) \cdot n_p(v_h,v_p,t)]}{\partial v_h} dv_h dv_p \cdot V_{liq}^{-1} - Y_{xg}^{-1} \cdot \mu \cdot \frac{c_g}{K_{X,g}+c_g} \cdot \varrho \cdot v_d \cdot V_{liq}^{-1} \quad (2i)$$

2.2. Initial Conditions and Numerical Method

A 2D normal distribution was chosen as the initial condition and the volume of the dispersed mycelia was zero at the beginning. For a numerical solution of Eq. (2a), a 1st order scheme with flux limiter is used [3].

3. RESULTS AND DISCUSSION

Using the PBM described above, we simulated the cultivation of *A. niger* pellets in the absence and in the presence of abrasion. As shown in Figure 2B, the pellet volume increases without abrasion for up to 15 hours as the glucose is depleted. The hyphal volume also stops growing after 15 hours. In the presence of abrasion, the pellet volume increases, but due to abrasion, a left-skewed distribution is obtained in the first hours of cultivation (Figure 2C). Towards the end of cultivation, all pellets have a very similar pellet volume as a result of growth and abrasion (Figure 2C). Because most of the hyphae are in the center of the pellet and only a

small part of the hyphae is in the area affected by abrasion, the hyphal volume increases with time. Small dense pellets are formed. The size distribution of the pellets is significantly narrower than in cultivation with lower shear stress, in which the pellets are not abraded. This trend and the simulated glucose concentration development consumed faster in cultivation with abrasion could also be observed in yet unpublished experiments conducted by cooperation partners.
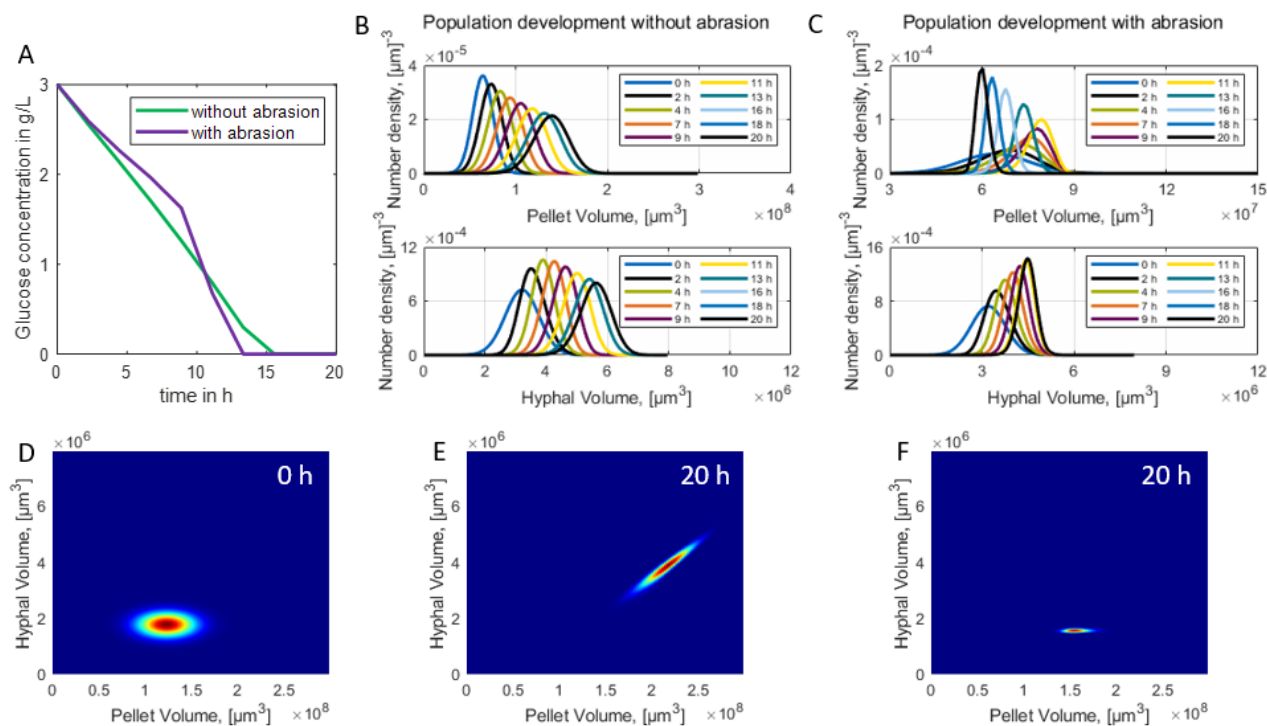

Figure 5: Simulation results of A. niger pellets in submerged cultivation with and without abrasion. A: The glucose consumption profile. B & C: The distribution of pellet volume and hyphal volume throughout the cultivation process. D: The 2D distribution of A. niger in the initial state. E & F: The 2D distribution of A. niger after 20 hours of cultivation.

4. CONCLUSIONS

In the current study, we employ a two-dimensional population balance model to describe the evolution of *A. niger* pellets in the submerged cultivation. The model incorporates growth and abrasion effects, reflecting the observed glucose consumption pattern. We plan to expand this model by incorporating additional factors such as breakage and aggregation, thus enabling a more holistic investigation into the influence of different cultivation conditions.

ACKNOWLEDGEMENTS

REFERENCES

[1] Böl M., Schrinner K., Tesche S., Krull R., 2021. Challenges of influencing cellular morphology by morphology engineering techniques and mechanical induced stress on filamentous pellet systems - A critical review. 10.1002/elsc.202000060

[2] Müller H., Deffur C., Schmideder S., Barthel L., Friedrich T., Mirlach L. et al., 2023. Synchrotron radiation based microcomputed tomography for three-dimensional growth analysis of *Aspergillus niger* pellets 10.1002/bit.28506.

[3] Qamar S., Ashfaq A., Warnecke G., Angelov I., Elsner M.P., Seidel-Morgenstern A., 2007. Adaptive high-resolution schemes for multidimensional population balances in crystallization processes. 10.1016/j.compchemeng.2006.10.014

Modelling of silica synthesis in laminar and turbulent flames with an extended PBE model and CFD

Malamas Tsagkaridis[1], Stelios Rigopoulos[1] and George Papadakis[2]
[1]Department of Mechanical Engineering, Imperial College London, London, UK
[2]Department of Aeronautics, Imperial College London, London, UK
Corresponding author email: m.tsagkaridis18@imperial.ac.uk

ABSTRACT

In the present study, we propose a novel extended population balance equation (PBE) model for aggregation and sintering and couple it with computational fluid dynamics (CFD) to investigate synthesis of silica nanoparticles in a laminar and a turbulent diffusion flame. The extended PBE includes finite-rate sintering of primary particles by solving the PBE together with a transport equation for the number concentration of primary particles. The model is validated with the detailed experimental *in-situ* SAXS data of Camenzind et al. (2008) and is also compared with a monodisperse and a two-PBE approach. For the turbulent-flame case, the extended PBE model is incorporated into a large eddy simulation - probability density function (LES-PDF) modelling framework, accounting for the interactions between turbulence, chemistry and particle dynamics. By retaining the same kinetics in both cases without any adjustments in parameters, we focus on the modelling issues arising in silica flame synthesis. The coupled CFD-PBE simulation with the extended one-PBE model reduces substantially the computational time as compared with a two-PBE model which allows the investigation of 3D turbulent flows. Excellent agreement was found between numerical predictions and experimental data for temperature along the centreline for both flames. Reasonably good agreement was found between numerical predictions and SAXS data for primary particle diameters in the laminar-flame case. However, in the turbulent-flame case, the LES model underestimated the SAXS data for the primary particle diameter by a factor of two. This was attributed to uncertainties in the nucleation model and the precursor decomposition kinetics.

Keywords: population balance, CFD, sectional method, flame synthesis, turbulent flame

1. INTRODUCTION

Aerosol flame synthesis is one of the main methods for the industrial production of nanomaterials. The nanoparticles produced find a wide range of applications in gas sensors, energy storage materials, catalysts, among others. Several processes take place during the formation of nanoparticles in flames, including fuel combustion, precursor decomposition and oxidation, nucleation, condensation, aggregation and sintering. Product characteristics are highly affected by flow configuration, flame temperature, etc. Prediction of particle morphology in different flow regimes, such as laminar or turbulent, remains a challenge.

The main objective of the present study is to investigate numerically the synthesis of silica nanoparticles in a turbulent flame via a comprehensive CFD-PBE methodology that also accounts for the turbulence-chemistry and turbulence-particle dynamics interaction. The extended PBE comprises a sectional method where the PBE is solved together with a transport equation for the number concentration of primary particles. Results are compared with the detailed experimental *in-situ* small-angle X-ray scattering (SAXS) measurements of Camenzind et al. (2008) for the "S-2" and "S-10" flames.

2. METHODOLOGY

2.1. A novel extended one-PBE model for aggregation and sintering

The evolution of the particle size distribution of aggregates is described by the PBE which assumes the following form:

$$\frac{\partial n}{\partial t} + u_j \frac{\partial n}{\partial x_j} = \frac{\partial}{\partial x_j}\left(D_p \frac{\partial n}{\partial x_j}\right) + B\delta(v - v_{nuc}) + C(Y, v)$$

$$+ \frac{1}{2}\int_0^v \beta(w, v - w)n(w)n(v - w)dw - \int_0^\infty \beta(v, w)n(v)n(w)dw \tag{1}$$

where v and w express volume of aggregates, while $n = n(\boldsymbol{x}, t, v)$ is the particle number density concentration (denoting number of particles per unit of particle volume and mixture volume). $\beta(v, w)$ is the **aggregation** kernel, B and C denote the **nucleation** and **condensation** rates, respectively. The transport equation for the number concentration of primary particles, N_p, takes the following form:

$$\frac{\partial N_p}{\partial t} + \frac{\partial(u_j N_p)}{\partial x_j} - \frac{\partial}{\partial x_j}\left(D_p \frac{\partial N_p}{\partial x_j}\right) = J - \frac{3}{\tau_s}\left(\frac{V}{v_p} - \frac{M_{23}}{v_p^{2/3}}\right) \tag{2}$$

Where J is the nucleation rate, v_p is the average primary particle volume V the particle volume fraction, M_{23} is the 2/3 fractional moment of the PSD, and τ_s is a **sintering** characteristic time. The major advantage of this model over the conventional one-PBE model is that it brings a finite-rate sintering model into the PBE. The main assumption adopted here is that the size distribution of primary particles is monodisperse, while the size distribution of aggregates is described by Eq. (1).

2.2. Numerical method - Coupling of PBE with CFD

A conservative finite-volume sectional method developed by Liu & Rigopoulos (2019) was employed for the numerical solution of the PBE. The advantage of the method is that it provides an accurate prediction of the particle size distribution and conserves the first moment (with respect to volume) during the aggregation process, an important feature for mass balance.

The PBE models have been implemented in our in-house CFD code BOFFIN, which is based on the variable-density low Mach number formulation of the Navier-Stokes equations. The Navier-Stokes equations are discretised by applying the finite volume method. The pressure-velocity coupling is dealt with an iterative SIMPLE-type scheme. The transport equations for the reactive scalars and discretised PBE are solved with a fractional step method, where separate fractional steps were employed for convection-diffusion, chemical reaction and PBE integration. The PDF-stochastic field method was employed to describe the influence of the unresolved scales for the turbulent-flame LES simulations.
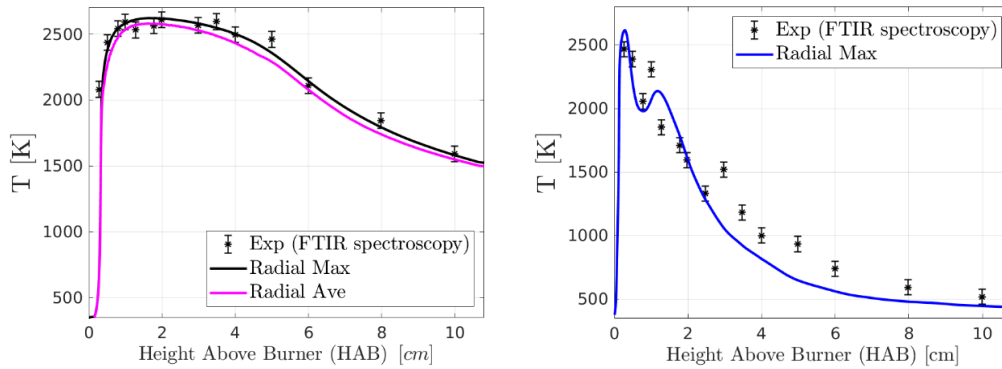
3. RESULTS AND DISCUSSION

Figure 1. Comparison of numerical predictions with experimental FTIR data for flame temperature along the centreline for the laminar flame (left) and the turbulent flame (right).

A comparison of numerical results for temperature with the experimental FTIR data of Camenzind et al. (2008) for both the laminar and the turbulent case is shown in Fig. 1. In the present study, numerical results for flame temperature are in good agreement with the experimental data, largely due to the direct coupling of detailed chemistry with flow and the inclusion of the model for the thermal radiation from particles.

Numerical predictions for the primary particle diameters, $d_{p,av}$, along the pathline of maximum silica volume fraction for both the laminar and the turbulent case are shown in Fig. 2. Results are compared with the *in-situ* experimental SAXS data of Camenzind et al. (2008). Reasonably good agreement is found between numerical predictions and SAXS data in the laminar-flame case (left). However, in the turbulent-flame case (right), the LES model underestimates the SAXS data for the primary particle diameter by a factor of two.
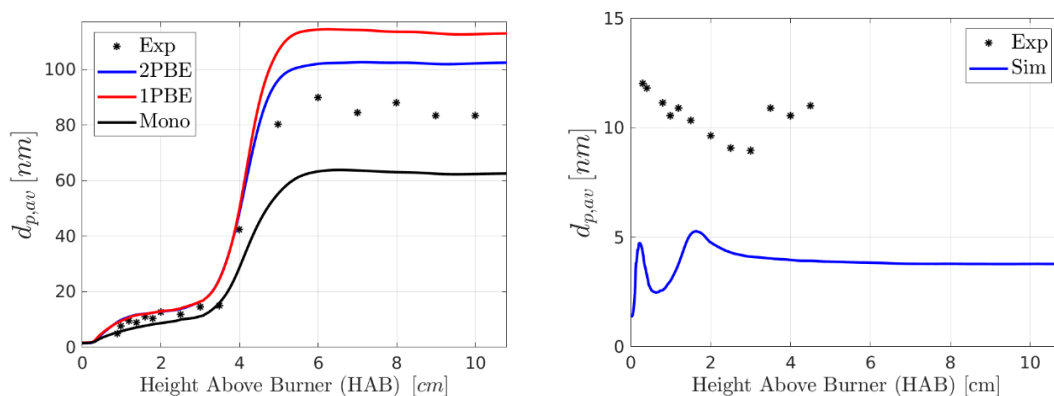
Figure 2. Comparison of experimental SAXS data with numerical predictions for primary particle diameters obtained with the extended one-PBE model for the laminar flame (left) and the turbulent flame (right). Results with a two-PBE and a monodisperse model are also presented in the left figure.

Table 1. Computational performance of the CFD-PBE models for describing aerosol dynamics.

Laminar Flow	Mono	Two-PBE	Extended one-PBE
CPU time (s) / timestep	0.187	1.145	0.32
No. of equations	3	114	61

The total CPU time per timestep for simulating all processes (including flow field and PBE solution) for the laminar-flame case for each of the three models examined is presented in Table 1. The simulation with the one-PBE model requires about a third of the CPU time spent on the two-PBE model, while it requires less than twice time needed by the monodisperse model.

4. CONCLUSIONS

The synthesis of silica nanoparticles in a laminar and a turbulent diffusion flame was studied via population balance modelling coupled with CFD. A novel extended one-PBE model that can predict the evolution of particle morphology while reducing substantially the computational cost as compared to other approaches has been proposed. Numerical predictions were compared with experimental data from the literature. Overall, the results showed that the coupling of CFD and detailed PBE can describe the evolution of particle properties during silica flame synthesis. Some discrepancies with the experimental data were present for the turbulent-flame case. By considering the extent to which the elements of the methodology have been validated in previous works, the discrepancy was attributed to uncertainties associated with the nucleation model and precursor decomposition kinetics. The results of this work have been published in the literature (Tsagkaridis et al. 2023, Tsagkaridis et al. 2023b).

REFERENCES

Camenzind, A., Schulz, H., Teleki, A., Beaucage, G., Narayanan, T., & Pratsinis, S. E. (2008). Nanostructure evolution: from aggregated to spherical SiO2 particles made in diffusion flames.

Liu, A., & Rigopoulos, S. (2019). A conservative method for numerical solution of the population balance equation, and application to soot formation. *Combustion and Flame*, *205*, 506-521.

Tsagkaridis, M., Rigopoulos, S., & Papadakis, G. (2023). Modeling of silica synthesis in a laminar flame by coupling an extended population balance model with computational fluid dynamics. *Aerosol Science & Technology*, *57*(4), 296-317.

Tsagkaridis, M., Papadakis, G., Jones, W.P. *et al.* Large Eddy Simulation of Turbulent Flame Synthesis of Silica Nanoparticles with an Extended Population Balance Model. *Flow Turbulence Combust* **111**, 1029–1057 (2023).

A multi-dimensional and bi-directional PBM-DEM model to describe bi-component granulation processes with liquid addition

Ashley Dan[1], Tarun De[2], Ashok Das[3], Urjit Patil[4] and Rohit Ramachandran[1]
[1]Department of Chemical and Biochemical Engineering, Rutgers University, Piscataway, NJ, USA
[2] Department of Mathematics and Statistics, IIT Kanpur, Kanpur, UP, India
[3] Department of Mathematics and Statistics, University of Limerick, Limerick, Republic of Ireland
[4]Department of Statistics, Rutgers University, Piscataway, NJ, USA
Corresponding author email: rohit.r@rutgers.edu

ABSTRACT

Granulation is an important process operation in industries such as chemicals, pharmaceuticals, and agricultural sectors. Computational tools are now recognized as an essential component of process and product design, analysis, and optimization. In this study, we present an integrated PBM-DEM model of a granulation process that incorporates aggregation, breakage, and liquid addition mechanisms. The population balance model (PBM) is three-dimensional and accounts for distributions with respect to solid 1, solid 2 and liquid, to represent a bi-component formulation consisting of an active pharmaceutical ingredient (API), excipient and liquid binder. Discrete element model (DEM) model is bi-directionally coupled with the PBM to utilize collision frequency-based kernels. These collision frequencies between particles are a function of dynamic particle size distributions and particle properties that contribute to preferential aggregation, breakage, liquid adsorption, or gas consolidation. The PBM-DEM model can simulate distributions and time evolutions of important granule attributes such as granule size, liquid content, and composition. Simulated trends are consistent with experimental trends observed in literature and in our previous work. DEM coupling increases the mechanistic nature of the PBM, as the use of collision frequency reduces the number of fitted constants required for model calibration. The combined model is also optimized for improved computational efficiency and can be simulated efficiently for its ultimate use in process design and analysis.

Keywords: granulation; population balance model; discrete element method; aggregation; collision frequency

1. INTRODUCTION

Wet granulation is a common and complex industrial unit operation in various sectors such as specialty chemicals, pharmaceuticals, consumer goods and agriculture. It is now recognized by industry, regulatory authorities and academia that process models can be used in all stages of a product lifecycle for effective design, analysis, control, and optimization. Wet granulation often requires the development of multi-scale, multi-form and multi-dimensional process models and a popular technique is a coupled population balance model (PBM) and discrete element method (DEM) model. Several studies (Das et al 2022, Barrasso and Ramachandran 2014, Barrasso et al 2014, Nakamura et al 2022, Tamrakar et al 2018) have made substantial advances in the development and use of PBM-DEM models to describe key dynamics of wet granulation but there exist gaps that remains unaddressed, with regards to the incorporation of key rate processes, granule properties and computational efficiency of the model. Additionally, the models implemented in these studies are typically 1-dimensional or 2-dimensional, which contains certain limitations as it only accounts for a single component formulation. Therefore, the objective of this study is to develop a bi-directionally coupled 3-dimensional PBM-DEM model that incorporates aggregation, breakage, liquid addition, and consolidation. The model will account for multiple granule attributes such as granule size, liquid content, fractional composition of solid 1 and porosity. The model will also be computationally efficient to ensure its effective use for process design and analysis.

2. MATERIALS AND METHODS

2.1 Model Development (PBM-DEM Coupling)

A 3-dimensional Population Balance Model (PBM) was used to track the particle size distribution, liquid content, and API composition over time during granulation. The general form of the PBE is shown in Equation 1, where the internal coordinates consist of two solid (s_1, s_s) and a liquid (l) volume. Solid volumes, s_1 and s_2, signify two solid components in the granule, API and excipient volume, respectively. To track porosity of each discretized bin, gas volume was lumped into the present distributions.

$$\frac{\partial}{\partial t}F(s_1, s_2, l, t) + \frac{\delta}{\delta l}\left[F(s_1, s_2, l, t)\frac{dl}{dt}\right] = R_{agg}(s_1, s_2, l, t) + R_{break}(s_1, s_2, l, t) \tag{1}$$

The rate processes included in this PBM are aggregation (R_{agg}), breakage (R_{break}), liquid addition, and consolidation. The specific kernels used to describe these rate functions are as described in Barrasso et al., 2014. While the aggregation and breakage rates are calculated from kernels that are functions of collision and impact frequencies, respectively, which are obtained from DEM, the liquid addition process is modelled entirely in DEM. DEM was incorporated in this work to capture particle scale interactions as a function of the subjected force fields (i.e. impeller rotations, gravity) and modelled using Newton's second law of motion. The Hertz-Mindlin model was used to estimate the normal and tangential contact forces acting on each particle (Di Renzo and Di Maio 2005). The collision detection scheme employed (Das et al, 2022) distinguishes new and repeated collisions to ensure repeated collisions are not recounted.

The coupled model is first initialized through the DEM simulation which incorporates geometric, material and process parameters of the system which consists of solids 1 and 2 and liquid particles. Then, DEM is run for several seconds to ensure a statistically accurate representation of collision frequencies and particle velocities. Next, liquid particles are introduced and its interactions include incorporation into the solid particles or merging with other liquid particles upon collision. At a defined coupling interval, the DEM provides an updated collision and impact frequency to the PBM, which simulates the net changes in size, composition, liquid content, and porosity. The updated distributions are then used to re-initialize the DEM simulation. This iterative simulation procedure repeats until the end of the process.

2.2 Parameters and Initial conditions

DEM simulations were modelled at a timestep of 1e-6 seconds, in a 0.06m diameter granulation, at a speed of 60 rpm. Solid particles were inserted and allowed to settle in the granulator before liquid particles were introduced to simulate the liquid addition process. The solid and liquid particles differ in properties as shown in Table 1.

Table 1. Parameters and initial conditions used in DEM simulations.

Parameters	Solid Particles	Liquid Particles
Particle density [$kg\ m^{-3}$]	1668	1000
Coefficient of restitution [-]	0.3	0.05
Poisson ratio [-]	0.055	0.1
Young's modulus [Pa]	5E6	5E6
Sliding friction coefficient [-]	0.3	0.1
Rolling friction coefficient [-]	0.1	0.01

3. RESULTS AND DISCUSSION

In this study, we demonstrate the need to couple a DEM with PBM under different conditions. PBMs have generally assumed that all particles have an equal probability of colliding with one another. This usually leads to either an over or under prediction of granule dynamics. For this work, we consider two cases which are a dilute phase system (e.g., fluid-bed granulation) and a dense phase system (e.g., high-shear granulation). Within each case, we vary initial configurations to account for different drug loadings (API: excipient ratio), liquid to solids ratio, and initial primary particle size differences between API and excipient. Results show key differences in collision frequencies and granule growth dynamics between the dilute and dense phase which a PBM on its own will be unable to discern. For a dilute phase system, we see that the collision frequencies are randomly distributed with propensity for particles of similar sizes to collide with each other more frequently. For a dense phase system, particles collide with other neighboring particles as influenced by their

material properties, their tendency to segregate and relative motion. These differences in collision frequencies are illustrated in Figure 1. In both phases, we see that the variation in collision frequencies in different systems result in key differences in particle size distribution, liquid content, and API composition as a function of initial configurations, which a PBM will not be able to capture accurately. The overall model is also able to be simulated efficiently, where 1 second of DEM simulation requires approximately 81 minutes.
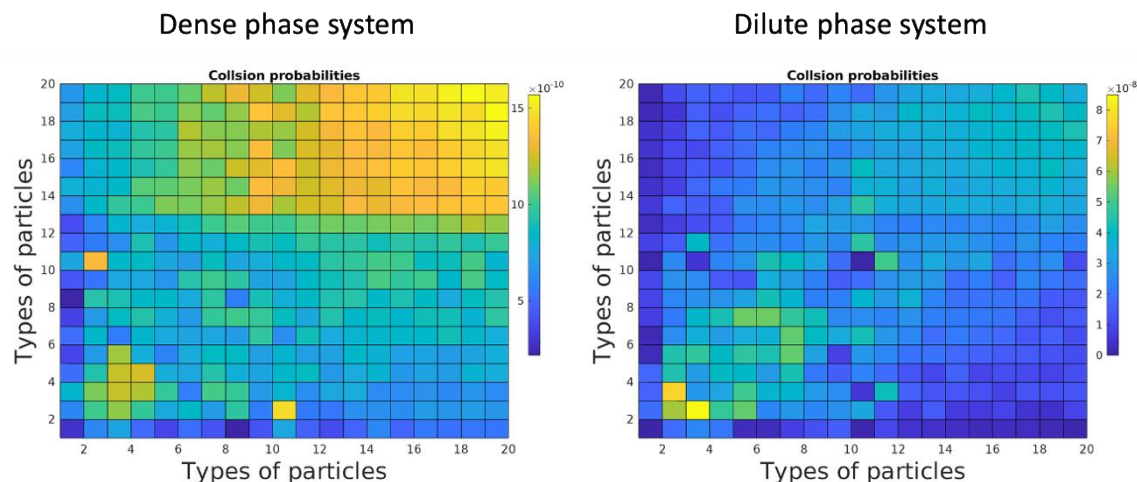

Figure 1. *Collision probabilities between particles of different sizes in a dense phase system and dilute phase system*

4. CONCLUSIONS

A computationally efficient multi-scale model for various wet granulation cases and conditions is developed via a bi-directionally coupled PBM-DEM model. The multi-scale model was successful in simulating dynamics of key granule attributes and when compared with experimental trends, show superior sensitivity and accuracy compared to a more common PBM only model and/or existing PBM-DEM models. The multi-scale model framework accurately accounts for the effects of process parameters, material properties and design attributes that usually are important to account for during process and product design.

REFERENCES

Das A., De T., Kaur G., Dosta M., Heinrich S., Kumar J., 2022. An efficient multiscale bi-directional PBM-DEM coupling framework to simulate one-dimensional aggregation mechanisms. *Proceedings of the Royal Society A Mathematical, Physical, and Engineering Sciences* 22, 1471-2946. 10.1098/rspa.2022.0076

Barrasso D., Ramachandran R., 2014. Multi-scale modeling of granulation processes: Bi-directional coupling of PBM with DEM via collision frequencies. *Chemical Engineering Research and Design Volume 93* 14, 0263-8762. 10.1016/j.cherd.2014.04.016

Barrasso D., Eppinger T., Pereira F. E., Aglave R., Debus K., Bermingham S. K., Ramachandran R., 2014. A multi-scale, mechanistic model of a wet granulation process using a novel bi-directional PBM–DEM coupling algorithm. *Chemical Engineering Science Volume 123* 14, 0009-2509. 10.1016/j.ces.2014.11.011

Nakamura H., Baba T., Ohsaki S., Watano S., Takehara K., Higuchi T., 2022. Numerical simulation of wet granulation using the DEM-PBM coupling method with a deterministically calculated agglomeration kernel. *Chemical Engineering Journal Volume 450* 22, 1385-8947. 10.1016/j.cej.2022.138298

Tamrakar A., Chen S. W., Ramachandran R., 2018. A DEM model-based study to quantitatively compare the effect of wet and dry binder addition in high-shear wet granulation process. *Chemical Engineering Research and Design Volume 142* 18, 0263-8762. 10.1016/j.cherd.2018.12.016

Di Renzo A., and Di Maio F.P., 2005. An improved integral non-linear model for the contact of particles in distinct element simulations. *Chemical engineering science, 60(5),* pp.1303-1312. 10.1016/j.ces.2004.10.004

Hybrid Population Balance Modeling of Agglomeration Processes in Multi-Component Suspensions

Frank Rhein[1], Leonard Hibbe[1], Hermann Nirschl[1]

[1]Karlsruhe Institute of Technology (KIT), Institute of Mechanical Process Engineering and Mechanics,
Strasse am Forum 8, 76131 Karlsruhe (Germany)
Corresponding author email: frank.rhein@kit.edu

ABSTRACT

Agglomeration is a unit operation in mechanical process engineering and thus relevant for almost all processes in particle technology. Targeted or selective agglomeration in multi-component suspensions finds wide applications. A current example is the microstructure in lithium-ion batteries, which is adjusted by hetero-agglomeration and significantly influences the resulting product properties. Only limited analytical tools exist to determine relevant properties, such as the material-specific agglomerate composition. This motivates the search for predictive computational methods that provide insight into the micro-processes taking place and thus access to process information that cannot be measured.

Generally, population balance equations (PBE) are used for this purpose, which allow a calculation of macroscopic agglomeration processes. Essential is a reliable determination of the agglomeration and breakage rates, the so-called *kernels*. Especially in multi-component suspensions this is challenging and hardly described so far, since all interactions between all occurring components have to be considered and their description is further complicated by locally heterogeneous surface properties. Another challenge in modeling real systems is the availability of reliable and comprehensive material data. In the field of agglomeration, in particular pH-dependent surface potentials, Hamaker constants, but also fundamental correlations for the hydrophobic interaction are not available or are subject to errors. This totality of uncertainties complicates or prevents a purely predictive modeling. Often correction factors are used, which are optimized based on experimental data. In this contribution, an alternative approach is presented in which the mechanistic PBE model (whitebox) is extended with data-driven models from the machine learning (ML, blackbox) domain. The resulting hybrid model (HM) combines the advantages and mitigates the disadvantages of purely data-driven and physics-based approaches.

A hybrid model of agglomeration processes can be realized in various ways: A variety of different ML algorithms can be used either to estimate the *kernels* for the PBE (serial HM) or to correct the PBE output (parallel HM). Since the optimal choice of HM architecture is highly problem dependent, a general and objective framework for model selection and arrangement is presented (Rhein et al., 2023). A repeated nested cross-validation with integrated hyperparameter optimization ensures a fair and meaningful comparison between different HM. This framework is finally applied to experimental data of magnetic seeded filtration and it is shown that the prediction error of the pure PBE model can be reduced by applying hybrid approaches.

Keywords: hetero-agglomeration; population balance equations; machine learning; hybrid modeling; hyper-parameter optimization; repeated nested cross-validation

MATERIALS, METHODS AND RESULTS

Details on this paper are published open access in Rhein et al. (2023) and will not be paraphrased here. In short, a full-factorial study of various HM-architectures in combination with various ML-algorithms were tested and compared objectively with the developed framework. The resulting hybrid models are visualized in Fig. 1 and Fig. 2 shows that both the serial and pure blackbox model improved prediction accuracy, i.e. lowered the root mean square error (RMSE) of the predictions. The parallel arrangement was not able to improve the predictions which emphasizes that the underlying equations (PBE) are correct, but necessary information (kernels) are missing. Nevertheless, using a serial HM instead of purely data-driven approaches makes the overall model more transparent, as the insights into the micro-processes calculated by the PBE are still available.

The published work elaborates on this and further investigates aspects of hyperparameter optimization and interpolation ability of the investigated model structures.
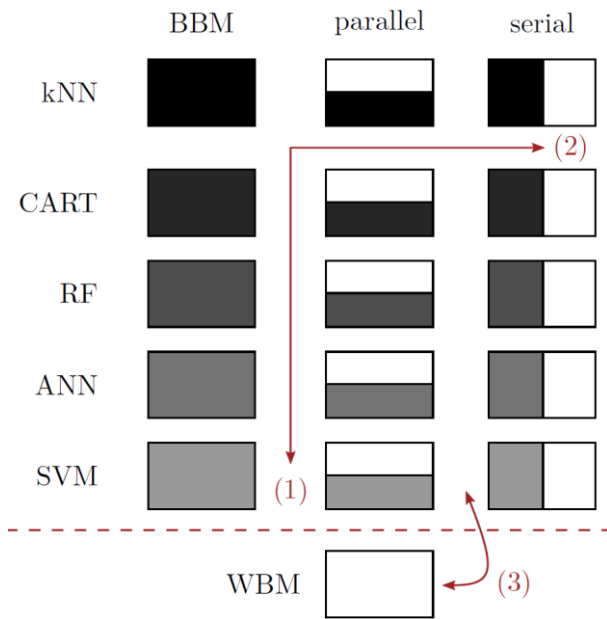

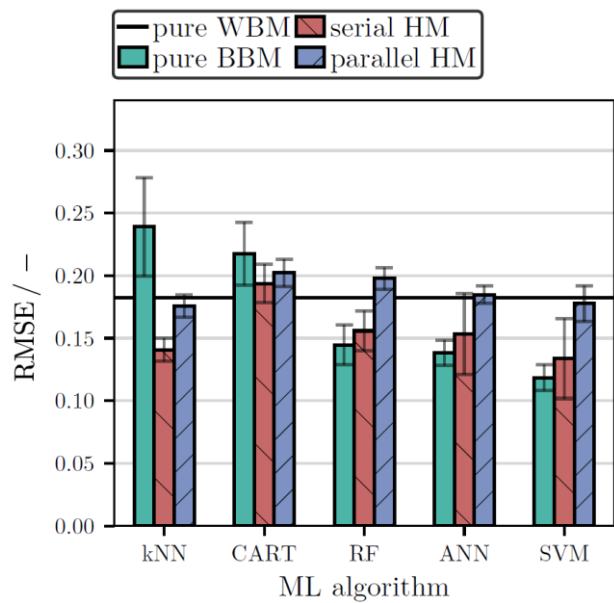**Figure 1.** *Full-factorial study structure*

Figure 2. *Comparison of prediction error – root mean squared error (RMSE) – of various model architectures*

CONCLUSIONS

Hybrid modeling is a promising technique for describing hetero-agglomeration processes as it is an elegant way of introducing experimental data into mechanistic models, while simultaneously attenuating major limitations of purely data driven approaches. The presented general framework alleviates one major difficulty in applying hybrid models, namely that the optimal model architecture and ML algorithm cannot be known beforehand, as they are highly problem-dependent. By implementing a repeated nested cross validation with integrated hyper-parameter optimization, any HM combination can be compared for any given data set in a fair and objective manner to select the best-suited architecture. Additionally, the framework allows for a statistical evaluation of the selected hyper-parameters, which paves the way for further enhancement of model accuracy. The capabilities of this approach were portrayed by a case study on magnetic seeded filtration: 16 different model architectures – including the pure WBM as well as pure BBMs, serial and parallel HMs for different ML algorithms – were compared with respect to multiple criteria. Both the serial HM and pure BBM were able to achieve a significant increase in prediction accuracy compared to the pure WBM. They also proved to enhance interpolation ability between experimental data points, especially when more elaborate ML algorithms like the ANN are used. However, as serial HMs further allow for a more accurate depiction of the ongoing micro-processes, while pure BBMs do not provide any insight, it is concluded that serial HMs are best suited for describing hetero-agglomeration during MSF.

REFERENCES

Rhein F., Hibbe L., Nirschl H., 2023. Hybrid modeling of hetero-agglomeration processes: a framework for model selection and arrangement. *Engineering with Computers.* 10.1007/s00366-023-01809-8

Experimental and numerical analysis of aerated non-coalescing stirred tanks

Francesco Maluta[1], Federico Alberini[1], Alessandro Paglianti[1] and Giuseppina Montante[1]
Department of Industrial Chemistry "Toso Montanari", University of Bologna, Italy
Corresponding author email: francesco.maluta@unibo.it

ABSTRACT
The Reynolds Averaged Two Fluid Model and Population Balance equations were solved for an aerated stirred tank to obtain the bubble size distribution with different breakup kernels in non-coalescing conditions, thus making possible a clear assessment of different breakup mechanisms. The numerical results compared with experimental bubble size distributions, the power consumption and the gas-liquid flow regime showed a closer agreement with the experiments with the Luo and Svendsen kernel.

Keywords: breakup kernels; aerated stirred tanks; digital imaging; non-coalescing systems; CFD

1. INTRODUCTION

The reliable description of fluid particle breakup due to turbulent flow is especially important in many gas-liquid and liquid-liquid industrial applications. Several breakup mechanisms have been studied and modelled to describe the generation of smaller bubbles and droplets from a parent one, in the context of a population balance modelling (PBM) approach. From a PBM point of view the breakup of particles is often expressed as the contribution of a breakage frequency and a daughter distribution function, DDF.

The choice of the most appropriate breakup mechanisms to model gas sparged turbulent stirred tanks is still debated, and some of those mechanisms involve the definition of a critical threshold on turbulent variables which lead to breakup once exceeded. The detailed description of those models can be found in recent reviews on the constitutive equations for fluid particle breakup, e.g. Solsvik et al. (2013).

Generally, the effect of different bubble breakup kernels on the predicted bubble size distribution (BSD) in stirred tanks has been studied in presence of not negligible coalescence rate. For isolating the effect of just the breakup frequency on the predicted BSD, in the present work different breakup frequency models in the case of non-coalescing stirred tanks were compared. Besides the evaluation of the breakup models, non-coalescing aerated stirred tanks are relevant in biotechnological applications, where the presence of antifoams and electrolytes may inhibit coalescence.

2. MATERIALS AND METHODS

2.1. The system

A cylindrical, flat bottomed, fully baffled stirred tank 0.232m in diameter (T) equipped with a Rushton turbine with diameter D=T/3 positioned at an off-bottom clearance of T/2 was studied. Air was injected through a ring sparger of diameter T/5 positioned below the impeller in a liquid solution of water and NaCl with concentration equal to 0.21 mol/L, which was found sufficient to inhibit bubble coalescence.

The power consumption was measured with a strain gauge torque sensor; the flow regime was assessed by visual observation and the BSD were measured with digital cameras. To measure the BSD, images were collected close to the wall of the tank in the space between two consecutive baffles on a circular window 0.05m in diameter and at an axial elevation of 0.241m from the tank bottom. Further information on the geometry and experimental techniques may be found in a previous work (Maluta et al.,2023).

2.2. Computational Model

The steady state, isothermal, incompressible Reynolds Averaged Navier Stokes (RANS) equations, extended to two phases with the so-called Two-Fluid model (TFM) were numerically solved with Ansys Fluent 2020R2 in a domain matching the experimental system. The well-known mixture formulation of the two-equation k-ε turbulence model was adopted to model the Reynolds stress tensor. The formulation of the momentum conservation equations included the interphase drag and turbulent dispersion forces.

The bubble size needed to close the set of equations was obtained from the solution of a PBE. Since coalescence is inhibited, just the birth and death due to breakup phenomena were considered as sources in the bubble number density function (NDF) transport equation. Different breakup kernels were considered,

corresponding to three different breakup mechanisms. Hereafter just the breakup frequencies are reported, the DDFs were taken from the corresponding publications and are not reported here for brevity.

The breakup frequency, $g(d)$, in the kernel developed by Laakkonen et al. (2006) reads as:

$$g(d) = C_1 \varepsilon^{\frac{1}{3}} erfc\left(\sqrt{C_2 \frac{\sigma}{\rho_L \varepsilon^{\frac{2}{3}} d^{\frac{5}{3}}} + C_3 \frac{\mu_L}{\sqrt{\rho_L \rho_G} \varepsilon^{\frac{1}{3}} d^{\frac{4}{3}}}}\right) \tag{1}$$

With C_i being empirical constants shown to be grid dependent, and the other variables follow the usual notation. This breakup mechanism assumes that binary breakup of a bubble occurs when the turbulent velocity fluctuations across the particle surface are larger than a critical value.

The breakup frequency in the kernel developed by Lehr et al. (2002) reads as:

$$g(d) = \frac{1}{2} d^{\frac{5}{3}} \varepsilon^{\frac{19}{15}} \left(\frac{\rho_L}{\sigma}\right)^{\frac{7}{5}} \times \exp\left(-\sqrt{2}\left(\frac{\rho_L}{\sigma}\right)^{-\frac{9}{5}} d^{-3} \varepsilon^{-\frac{6}{5}}\right) \tag{2}$$

Where no empirical constants are defined, and breakup is encountered when the inertial stress of the eddy bombarding the parent bubble is larger than the interfacial force of the smallest daughter particle.

The breakup frequency in the kernel developed by Luo and Svendsen (1996) reads as:

$$g(d) = \frac{1}{2} \int_0^{\frac{d}{2^{\frac{1}{3}}}} \left\{ \frac{3 d'^2}{d^3} 0.92(1-\alpha_G) \left(\frac{\varepsilon}{d^2}\right)^{\frac{1}{3}} \int_{\zeta_{min}}^1 \left[\frac{(1+\zeta)^2}{\zeta^{\frac{11}{3}}} exp\left(- \frac{12\left(\left(d'^3/d^3\right)^{\frac{2}{3}} + \left(1 - d'^3/d^3\right)^{\frac{2}{3}} - 1\right)\sigma}{2\rho_L \varepsilon^{\frac{2}{3}} \zeta^{\frac{11}{3}} d^{\frac{5}{3}}} \right) \right] d\zeta \right\} dd' \tag{3}$$

With ζ being the ratio between the eddy colliding with the parent bubble and the parent bubble size d. The breakup is assumed once the turbulent kinetic energy of the bombarding eddies exceeds a critical value.

The PBEs coupled with the different breakup mechanisms were solved with the Quadrature Method Of Moments (QMOM) and 6 moments of the NDF were transported. Although unable to obtain the full BSD, QMOM is particularly advantageous for CFD simulations, since the bubble diameter in the interphase momentum exchange terms can be readily obtained from the ratio of the third to the second NDF moment (Marchisio & Fox, 2013).

3. RESULTS AND DISCUSSION

The bubble size distributions experimentally measured and numerically calculated at a stirring speed of N = 560rpm and a gas flow rate of Qg = 4L/min are shown in Figure 1a, both in terms of abscissas and weights obtained from the moments of the NDF, bars, and as reconstructed NDFs, dashed lines.

Figure 1a shows that the kernel developed by Luo and Svendsen (1996) better reproduces the experimental distribution. In fact, for this model both the calculated abscissas and the relative weights are relatively close to the experimental ones. On the other hand, the breakup kernel by Lehr et al. (2002) fails in reproducing the measured BSD, while the one by Laakkonen et al. (2006) noticeably overpredicts the number of larger bubbles of the BSD. In order to quantify the agreement between the experimental and predicted BSDs, the deviation of the numerically predicted NDF i-th moments from the experimental ones are analyzed in Figure 1b. The deviations are calculated as:

$$\Delta Mi0 = \left| 1 - \left(\frac{M_i}{M_0}\right)^{Num} / \left(\frac{M_i}{M_0}\right)^{Exp} \right| \tag{4}$$

Figure 1b shows that the deviation of the numerical moments obtained with the kernel by Luo from the experimental ones are between 3% and 31%, while the deviations for the other two kernels generally increase with the moment order, reaching deviations larger than 100 times the experimental moments.

The different predictions of the BSD by the three breakup kernels reflect on the bubble Sauter mean diameter in the impeller zone, affecting the impeller power consumption, Figure 1c, and predictions of the flow regime, Figure 2. In particular, the power consumption obtained both as the total torque on the tank fixed walls and the mass integral of ε show that the model by Luo and Svendsen predicts the closest agreement with the experimental data. Concerning the flow regimes, the adoption of the Lehr breakup model results in a loading regime, the model by Luo and Svendsen predicts a complete recirculation regime, and the model by Laakkonen predicts a loading regime, in which few gas is entrained in the lower recirculation loops

close to the walls. The observed regime is complete recirculation, therefore the Luo and Svendsen model better replicates the experimental observations.
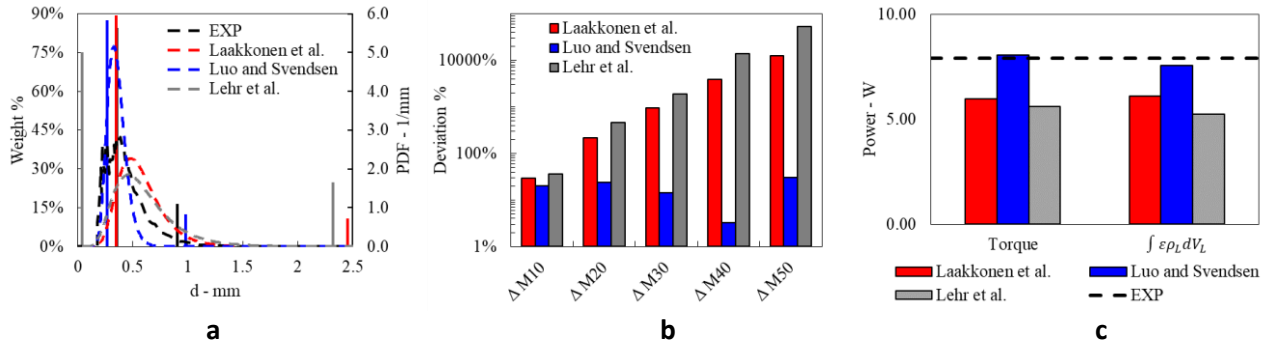

Figure 1. Numerical and Experimental BSD (a); moment deviations (b); impeller power consumption (c).
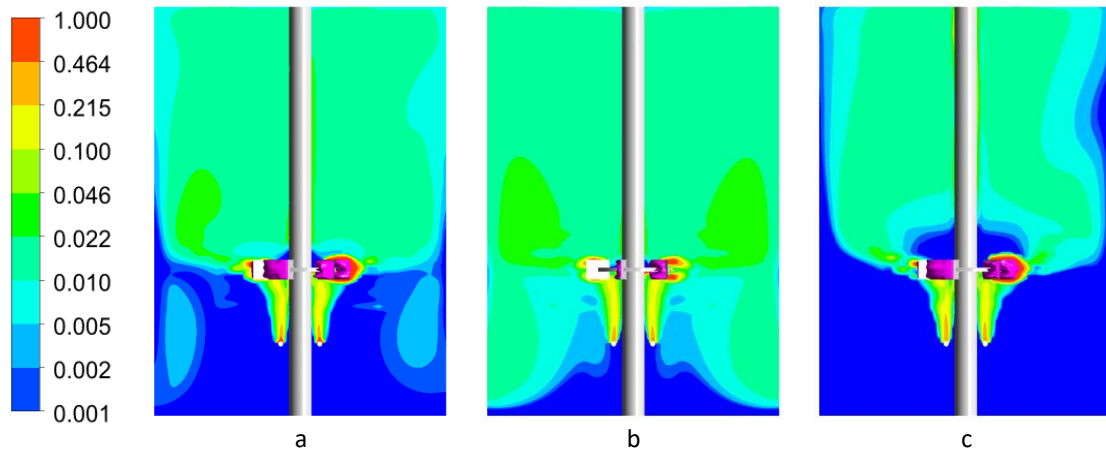

Figure 2. Gas volume fraction distributions: Laakkonen et al. (a), Luo and Svendsen (b) and Lehr et al. (c)

4. CONCLUSIONS

In the operative condition considered, the predictions of the breakup kernel by Lehr et al. cannot reproduce the flow features of the aerated tank experimentally observed. The kernel by Laakkonen et al. improves the predictions of the Lehr et al. kernel, but overpredicts the number of larger bubbles in the tank, resulting in a loading flow regime, which was not observed in the experiments. The kernel by Luo and Svendsen predict a BSD close to the measured one and correctly predicts the power consumption and the flow regime experimentally observed in the system. Additional operative conditions are under study to confirm these results.

REFERENCES

Buffo, A., & Marchisio, D. L., 2014. Modeling and simulation of turbulent polydisperse gas-liquid systems via the generalized population balance equation. Rev. Chem. Eng., 30(1), 73-126.

Laakkonen, M., Alopaeus, V. and Aittamaa, J., 2006. Validation of bubble breakage, coalescence and mass transfer models for gas–liquid dispersion in agitated vessel. Chem. Eng. Sci., 61(1), pp.218-228.

Lehr, F., Millies, M. and Mewes, D., 2002. Bubble-size distributions and flow fields in bubble columns. AIChE J, 48(11), pp.2426-2443.

Luo, H. and Svendsen, H.F., 1996. Theoretical model for drop and bubble breakup in turbulent dispersions. AIChE j., 42(5), pp.1225-1233.

Maluta, F., Alberini, F., Paglianti, A. and Montante, G., 2023. Hydrodynamics, power consumption and bubble size distribution in gas-liquid stirred tanks. Chem Eng Res Des, 194, pp.582-596.

Marchisio, D. L., & Fox, R. O., 2013. Computational models for polydisperse particulate and multiphase systems. Cambridge University Press.

Solsvik, J., Tangen, S. and Jakobsen, H.A., 2013. On the constitutive equations for fluid particle breakage. Rev. Chem. Eng, 29(5), pp.241-356.

Enhancing droplet detection in liquid-liquid systems through machine learning and synthetic imaging

Grégory Bana[1], Sophie Charton[1], Fabrice Lamadie[1], Tojonirina Randriamanantena[1], Didier Lucor[2], Nida Sheibat-Othman[3]

[1]CEA, DES, ISEC, DMRC, Université de Montpellier, Marcoule, 30200, France
[2]Laboratoire Interdisciplinaire des Sciences du Numérique, Gif-sur-Yvette, 91190, France
[3]Universite Claude Bernard Lyon 1, LAGEPP, UMR 5007, CNRS, Villeurbanne, 69100, France
Corresponding authors email bana.gregory@cea.fr, lamadie.fabrice@cea.fr

ABSTRACT

The knowledge of droplet size in liquid flows or emulsions is a fundamental parameter that strongly influences product quality, stability, and processes performance. In this communication, a new image processing algorithm for droplet detection in an emulsion based on machine learning is introduced. It is based on the combination of two neural networks and a 3D images modeling software. Validation on synthetic images as well as on experimental acquisition prove that it overpasses current image processing usually used in emulsion characterization.

Keywords: image processing, machine learning, droplet size measurement, droplet detection, convolutional neural networks

1. INTRODUCTION

Emulsions play a significant role in various industrial processes in many sectors such as food, pharmaceuticals, cosmetics and energy. Traditionally, droplet size measurement in emulsions has relied on conventional image processing algorithms like the Hough circular transform (HCT) introduced by (Davies, 1988). While these approaches are effective, they are only applicable to the characterization of dilute dispersed phase flows, and in the case of high droplet overlap in the images, they lead to frequent false detections.

In emulsion characterization, as in all image-processing problems, deep learning is replacing traditional image processing. This is especially true for convolutional neural networks (CNN), which are remarkably efficient at object recognition. To train such networks for object detection, it is crucial to create a huge database of labeled objects (droplets, bubbles...). Several approaches have been explored in the literature based on deterministic algorithms or even manual annotation (Patil et al., 2022) but significant challenges persist in creating labeled droplet databases suitable for a machine learning approach. Manual annotation is frequently an impractical option and traditional methods like HCT fall short in creating accurate databases due to the potential inclusion of incorrect labels.

This communication presents a new approach in which a deep learning algorithm is trained using synthetic images generated by a 3D graphics software and textured using a generative adversarial neural network, to tackle issues related to dataset creation. After describing the algorithm, some results on synthetics and real images are introduced and discussed.

2. PROPOSED ALGORITHM

The main flowchart of the proposed algorithm is summarized in Figure 1*Figure* . It is a three steps process:

1. Creation of a huge image dataset of well-known (size, position …) droplets using a 3D computer graphics software tool.
2. Texturing this base from real flow images using the CycleGAN neural network.
3. Training the YOLO (You Only Look Once (Redmon et al., 2016)) neural network object's detector on the textured image dataset.

The neural network used in this study is the object detector network YOLO in its V5 release. For an input image, it predicts rectangular bounding boxes frames around the detected objects. Hence, in the case of

spherical droplets, it provides information on their diameter. A detection probability is associated to each object, which allows tuning the detection performance. Usually, to train such a network, it is required to generate a training base of several thousands of labeled images containing both sharp and blurred droplets, which can be an issue. To this end, synthetic images were generated from Blender (a modeling software with 3D rendering). The use of synthetic images enables complete control of the drop size distribution (DSD), so ensuring an efficient labeling. In a second step, and in order to reinforce the learning process, a texture transfer with non-paired data from real images to synthetic images was performed using CycleGAN (Zhu et al., 2017)
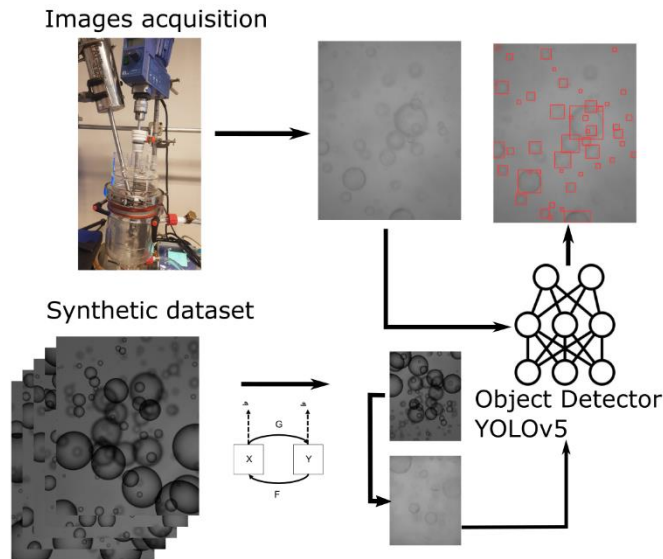

Figure 1. Main flowchart of the proposed algorithm

3. RESULTS AND DISCUSSION

3.1. Numerical Validation on a dataset of synthetic images

First, in order to evaluate the performance of the network, a test dataset of 1 000 synthetic textured images was generated. For comparison purpose, detections were made by both the neural network and the circular Hough transform, considering a confidence threshold of 0.95. Detection quality was assessed using two metrics: precision and recall. Precision is the number of right droplets detected divided by the total number of droplets detected. Recall is the number of right droplets detected divided by total number of right droplets. According to Figure 2 and Table 1, the network largely beats the circular Hough transform, both on precision and recall. The investigation also considered the influence of other parameters, such as the texture of synthetic images or the number of images in the training base.
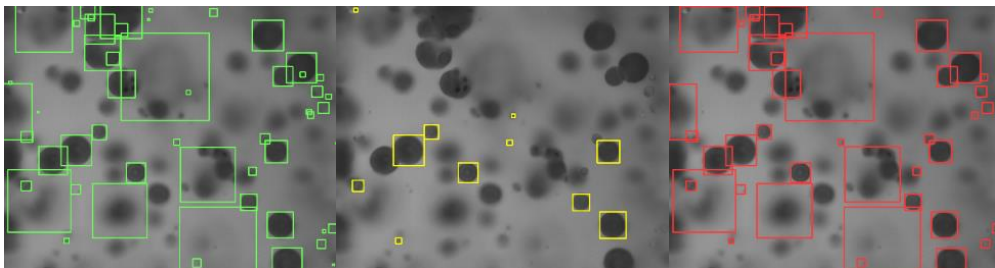

Figure 2. Left: Ground truth. Middle: Detection with CHT. Right: Detections with neural network

Table 1. Performances of CHT and neural network on 1000 test synthetic textured images

	Precision	Recall
Hough	0.536	0.240
Neural network (confidence = 95%)	1	0.758

3.2. Experimental validation on real emulsions

In a second step, by comparison with laser granulometry measurements, the performance of the algorithm was evaluated on real images. The fluid system used was 25 grams of silicone oil (viscosity of 200 mP.s−1) dispersed in 975 grams of ultrapure water (viscosity of 1 mP.s−1). The achieved hold-up in the tank was of 2.5%. Additionally, 3 grams of Polysorbate (Tween® 20, SigmaAldrich, Germany) were added to stabilize the emulsion and prevent coalescence phenomena during transport to the laser granulometer. The stirring speed was adjusted to 600 rpm and images were acquired thanks to an endoscopic probe (SOPAT GmbH) as shown on the left upper part of Figure 1. Eleven acquisitions of 200 images each were made, with each acquisition occurring every 400 seconds at a frame rate of three images per second. Analysis with the laser granulometer (Mastersizer 3000 from Malvern) were done on four samples, taken at four relevant times (400, 1200, 2000 and 4000 s) from the beginning of the agitation (t=0).

Figure 3 compares the DSD in volume measured with both technics. For the four times considered, the droplet size distributions are consistent, except for the smaller sizes where the number of small droplets obtained by the Mastersizer is higher than by image treatment. This can be due to the fact that the Mastersizer tends to overestimate the fraction of small droplets, while the machine learning approach is limited by the resolution of the images taken by the endoscopic probe, making the smallest objects undetectable.
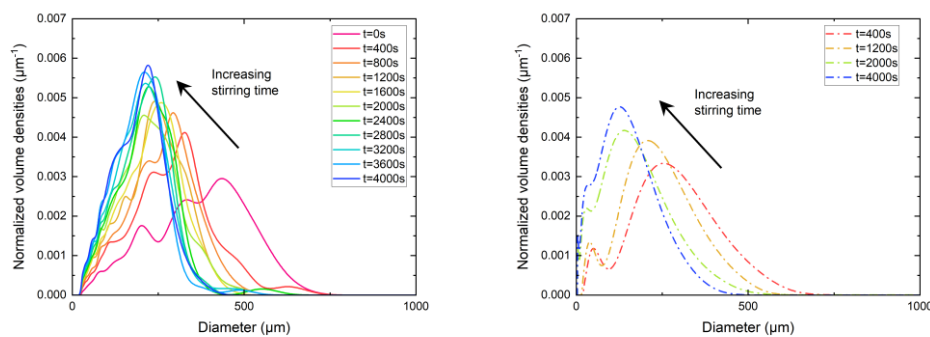

Figure 3. *Left: DSD found with image processing. Right: DSD found with laser diffraction granulometer*

4. CONCLUSION

In this communication, we have introduced a new image processing machine-learning algorithm for droplets detection in liquid-liquid systems. It is based on the combination of three numerical tools: the object detector YOLOv5, synthetic images generated by Blender and a neural network specialized in transfer texture, CycleGAN. This method overpasses the usual image processing technics, both in term of precision and recall. Moreover, it is consistent with other current DSD measurement technics like laser granulometry. The next step will be to determine the contribution of this detection method to the solution of the population balance equations using inverse methods.

REFERENCES

Davies, E.R., 1988. A modified Hough scheme for general circle location. Pattern Recognition Letters 7, 37–43. 10.1016/0167-8655(88)90042-6

Patil, A., Sægrov, B., Panjwani, B., 2022. Advanced deep learning for dynamic emulsion stability measurement. Computers & Chemical Engineering 157, 107614. 10.1016/j.compchemeng.2021.107614

Redmon, J., Divvala, S., Girshick, R., Farhadi, A., 2016. You Only Look Once: Unified, Real-Time Object Detection, in: 2016 IEEE Conference on Computer Vision and Pattern Recognition (CVPR). Presented at the 2016 IEEE Conference on Computer Vision and Pattern Recognition (CVPR), IEEE, Las Vegas, NV, USA, pp. 779–788. 10.1109/CVPR.2016.91

Zhu, J.-Y., Park, T., Isola, P., Efros, A.A., 2017. Unpaired Image-to-Image Translation Using Cycle-Consistent Adversarial Networks, in: 2017 IEEE International Conference on Computer Vision (ICCV). Presented at the 2017 IEEE International Conference on Computer Vision (ICCV), IEEE, Venice, pp. 2242–2251. 10.1109/ICCV.2017.244